

Aerodynamic Fuze Characteristics for Trajectory Control

by

Alexander Michael Budge

B.S., Aeronautical Science and Engineering
and Mechanical Engineering
University of California, Davis (1996)

Submitted to the Department of Aeronautics and Astronautics
in partial fulfillment of the requirements for the degree of
Master of Science in Aeronautics and Astronautics

at the

MASSACHUSETTS INSTITUTE OF TECHNOLOGY

June 1998

© Massachusetts Institute of Technology 1998. All rights reserved.

Author
Department of Aeronautics and Astronautics
May 20, 1998

Certified by
Eric Feron
Assistant Professor
Thesis Supervisor

Accepted by
Jaime Peraire
Chairman, Department Graduate Committee

MASSACHUSETTS INSTITUTE OF TECHNOLOGY

JUL 08 1998

Acro

LIBRARIES

Aerodynamic Fuze Characteristics for Trajectory Control

by

Alexander Michael Budge

Submitted to the Department of Aeronautics and Astronautics
on May 20, 1998, in partial fulfillment of the
requirements for the degree of
Master of Science in Aeronautics and Astronautics

Abstract

Recent development of micromechanical Inertial Management Units (IMUs) and Global Positioning Systems (GPS) capable of withstanding more than 16,000 g's has spawned renewed interest in unpowered guided munitions. Guidance schemes seek to increase the static targeting accuracy by decreasing the Circular Error Probability (CEP). In order to retain the usefulness of the vast stock piles of Army/Navy/USMC ammunition, numbering in the tens of millions of rounds, a fuze replacement is sought which incorporates all the necessary additions to transform these unguided shells into guided, or competent munitions. In particular, competent munitions require aerodynamic control actuation to effect trajectory control. Investigations focus on replacement fuzes for trajectory control by modulated roll control of a fixed magnitude lift vector.

Trajectory simulations with a modified point mass model reveal that typical ballistic trajectories exhibit an approximately invariant Mach number distribution for a range of launch angles. The trim lift coefficient is introduced as a figure of merit and simulations show the crossrange deflection of a trajectory to be very sensitive to the transonic distribution of the trim lift coefficient.

The development of grid generation processes and the implementation of Navier-Stokes CFD methods provide a means to investigate the underlying aerodynamic behavior of lift and torque generating geometric asymmetries. To engender confidence, the flow simulation is validated against wind tunnel and ballistic range data for baseline geometries.

Baseline computations identify four modes of transonic critical behavior related to the Mach dependent location of shocks on boat-tailed projectiles. Calculations with a spinning boundary condition capture the small angle of attack sign change of the Magnus moment, revealing that the sign change results from the contribution of the last 2% of the body length. Baseline computations also show that sting mounted wind tunnel models affect the pressure recovery over the boattail region at transonic Mach numbers, producing large errors in the wind tunnel modeling of transonic critical behavior.

Sliced and bent configurational asymmetries are examined as candidate lift generating geometries, but are found to be inefficient in that the asymmetries do not actuate the flow as intended with the net trim lift resulting primarily from residual aerodynamic effects and not from the high pressure surface of the asymmetry.

A leveraged boundary layer actuation concept is then pursued as a more efficient lift generating mechanism. Relatively small scale deviations in boundary layer development can drive transonic critical behavior producing large resultant trim forces, which can work synergistically with the transonic trajectory sensitivity to produce large maneuvering envelopes.

Finally, the thesis examines aerodynamic torque generation with short body-fitted and differentially canted strakes. An empirical design algebra for dual strakes can be written to simplify preliminary design, but computations show that the strakes interact such that performance does not scale directly with the number of strakes.

Thesis Supervisor: Eric Feron

Title: Assistant Professor

Thesis Supervisor: Eugene Covert

Title: Professor Emeritus

Acknowledgments

A brief acknowledgment of the usual suspects is in order. First, I would like to thank the people who have supported and encouraged me throughout my life; the people who seldom put their interests before mine; who have never been my adversaries, never sought to tear me down, but when my ratiocination became confused or when I have lost perspective on life they have restored me with kindness and humility. Primary among these are my mom and dad who made the effort to be my parents and my friends, but also the enumerable others who have given of themselves to be my friends. In a world in which it seems everyone wants to be the best, true friends are more than priceless, they give life.

I would like to thank Professor Eric Feron, my thesis supervisor and academic advisor, for the encouragement and support he has provided during my first two years of graduate education at MIT. I would also like to thank Professor Eugene Covert, my other thesis supervisor, for challenging me to think clearly and critically as well as for sharing the two directives of technical presentation: “Don’t suppress the zero!” and “Your goal is not to make it possible to understand, but to make it impossible not to understand.”

I would like to thank Bob Haines for providing the computational resources that made the project happen.

Sean George, my research cohort, deserves thanks not only for being there for external processing over an inky black cup of Tosci’s french roast, but also for being my friend.

I am also indebted to Earl P.N. Duque of the US Army Aeroflightdynamics Directorate at the NASA Ames Research Center for his help in getting setup with OVERFLOW.

Contents

1	Introduction	17
1.1	Concept of Competent Munitions	17
1.2	Projectile Dynamics	20
1.2.1	Dynamic Motion	22
1.2.2	Linearized Trim State	23
1.2.3	Ballistic Trajectory	24
1.3	Figure of Merit	26
1.4	Contributions	30
1.5	Overview	31
2	Aerodynamic Modeling	33
2.1	Requirements and Model Selection	33
2.2	Grid Generation	35
2.2.1	Surface Domain Decomposition and Grid Topology	36
2.2.2	Surface Grid Generation	37
2.2.3	Volume Grid Generation	41
2.2.4	Overlapped Connectivity	42
2.3	Numerical Convergence	43
2.3.1	Spatial Convergence	43
2.3.2	Temporal Convergence	45
2.4	Boundary Conditions	47
2.5	Validation	48
2.5.1	SOCBT Configuration	48

2.5.2	Mk41 5"/54 Configuration	50
3	Baseline Aerodynamic Behavior	53
3.1	Baseline Profiles	53
3.2	Mach Behavior	55
3.3	Transonic Critical Behavior	55
3.4	Sting Effects	60
3.5	Magnus Characteristics	63
4	Configurational Asymmetries for Lift Generation	67
4.1	Concept and Description of Geometries	67
4.2	Angle of Attack and Sideslip Angle Behavior	68
4.3	Parametric Study	70
4.4	Aerodynamic Behavior	73
4.4.1	Aerodynamics of the Bent Fuze	73
4.4.2	Aerodynamics of the Sliced Fuze	78
4.4.3	Aerodynamics of Normal Force Generation	82
4.5	Mach Behavior	85
4.6	Magnus Characteristics	89
4.7	Design Considerations	91
5	Leveraging Sensitivities for Lift Generation	95
5.1	Concept and Description of Geometry	95
5.2	Angle of Attack Behavior	97
5.3	Mach Behavior	99
5.4	Design Considerations	102
6	Canted Strakes for Torque Generation	105
6.1	Concept and Description of Geometry	106
6.2	Angle of Attack and Sideslip Angle Behavior	107
6.3	Parametric Study	108
6.4	Design Considerations	110

7	Conclusions and Future Work	113
A	Trim State Linearization	117
B	OVERFLOW Flow Solver Code Suite	121
B.1	OVERFLOW Flow Solver	121
B.2	HYPGEN Volume Grid Generator	124
B.3	PEGSUS Connectivity Solver	125
B.4	CHIMERA Grid Tools	125
C	Physical-Space Weight Function	127

List of Figures

1-1	Depiction of Spiraling Fixed-Trim Trajectory	20
1-2	Aeroballistic Coordinate System	21
1-3	Gyroscopic Behavior of Spin-Stabilized Projectile	23
1-4	Behavior of a Typical Ballistic Trajectory	25
1-5	Maneuvering Envelope Behavior	27
1-6	Range Variation with $C_{L_{trim}}$	28
1-7	Crossrange Sensitivity to Mach Local $C_{L_{trim}}$ Perturbations	28
2-1	Axisymmetric Surface Grid and Computational Coordinate System	38
2-2	Component and Resultant Grids for Sliced Geometry	39
2-3	Strake Grid Topology and Geometry	41
2-4	Half-Plane Showing Structured Volume Grid	42
2-5	Spatial Convergence in Two Orthogonal Surface Directions	44
2-6	Steady-State and Time Accurate Temporal Convergence	46
2-7	Basic SOCBT Configuration	48
2-8	Pressure Distribution Comparisons for SOCBT Configuration	49
2-9	Qualitative Flow field Comparison	50
2-10	Comparison of Mach Behavior for Mk41 Projectile	51
3-1	Baseline Profiles	54
3-2	Mach Behavior of Baseline Configurations	56
3-3	Transonic Critical Behavior Part I	57
3-4	Transonic Critical Behavior Part II	59
3-5	Mach Behavior of Sting Mounted Projectile	61

3-6	Boattail Flow Field Comparison for Free Flying and Sting Geometries	62
3-7	Linearity of Magnus Moment with Spin Rate	63
3-8	Distribution and Development of Magnus Force and Moment	64
4-1	Parametric Definitions for Configurational Asymmetries	68
4-2	Pitch and Yaw Linearity at Mach 1.1	69
4-3	Aerodynamic Behavior with Configurational Parameter Variations . .	71
4-4	Trim State Behavior with Configurational Parameter Variations . . .	72
4-5	Bent Configuration Pressure Distributions	74
4-6	Bent Configuration Boundary Layer Behavior at Mach 1.1	76
4-7	Transonic Critical Behavior of Bent Configuration	77
4-8	Bent Configuration Boundary Layer Behavior at Mach 0.90	78
4-9	Sliced Fuze Pressure Distributions at Mach 1.4	79
4-10	Sliced Configuration Pressure Distributions at Mach 1.1	80
4-11	Boundary Layer Behavior for Two Slice Angles at Mach 1.1	81
4-12	Normal Force and Pitch Moment Development at Mach 1.1	81
4-13	Comparison of Slender Body Theory and Computation	84
4-14	Force and Moment Development Comparison of Sliced and Bent Con- figurations at Mach 1.1	86
4-15	Aerodynamic Variation with Mach number for Configurational Asym- metries	87
4-16	Trim State Variation with Mach number for Configurational Asymmetries	88
4-17	Effects of Parameter Variations on Magnus for Bend at 4.25" and 50° Slice	89
4-18	Magnus Development over Configurational Asymmetries	90
4-19	Maneuvering Envelopes of Representative Configurational Asymmetries	92
5-1	BLAM Fuze Concept	96
5-2	The BLAM Fuze at Mach 0.95 and Zero Angle of Attack	97
5-3	Normal Force and Pitch Moment Behavior with Angle of Attack . . .	98
5-4	Normal Force and Pitch Moment Behavior with Mach Number	100

5-5	Trim Lift Variation with Mach Number	101
5-6	Maneuvering Envelope	102
6-1	Description of Strake Geometry	106
6-2	Roll Torque Variation with Angle of Attack and Sideslip Angle	107
6-3	Static Roll Torque Generation	109
6-4	Pressure Distribution Over Strake: Geometry 3 at 20°, Mach 2.0, and Zero Angle of Attack	111
A-1	Coordinate System for Rotational Motion Analysis	117
A-2	Rotational Motion	119
C-1	Grid Spacing Source Element	129
C-2	Typical Grid Spacing Specified by Source Weighting Elements	129

List of Tables

- 2.1 Hierarchy of Configurational Flow Modeling 34
- 6.1 Defining Parameters of Strake Geometries 108
- 6.2 Dual Strake Torque Scaling Parameters 110

Chapter 1

Introduction

The computational investigation of aerodynamic control actuator design of replacement fuzes for guided projectiles has four constitutive components: competent munitions, projectile dynamics, computational modeling, and projectile aerodynamic behavior. The components are combined to seek an effective pressure distribution for trajectory control. The competent munitions concept, as described in the next section, establishes the engineering framework for the design problem, while an understanding of projectile dynamics is important to the interpretation of design fitness. Computational modeling addresses the analysis engine utilized to investigate the problem, in particular, how CFD simulation can be applied to the design of a complicated aerodynamic system in a reliable manner. Computations elucidate characteristic projectile aerodynamic behavior. Finally, all four of the components are assembled to develop aerodynamic characteristics of replacement fuzes for guided projectiles.

1.1 Concept of Competent Munitions

Guidance of gun-launched munitions has been visited and revisited for decades, but reliable and cost-effective guided munitions have yet to be developed. Recent advances in technology and a fertile marketplace have renewed interest in unpowered guided munitions. Micro mechanical Inertial Management Units (IMUs) and Global Positioning Systems (GPS) capable of withstanding more than 16,000 g's have been

developed recently which could potentially be embedded in the fuze of a standard artillery round, allowing such a round to be converted into a highly accurate guided munition. The fuze of a projectile is the front end component which is used to arm and trigger the munition. Such conversions retain the usefulness of the vast stock piles of Army/Navy/USMC ammunition which number in the tens of millions of rounds. Guidance schemes seek to increase the static targeting accuracy by decreasing the Circular Error Probability (CEP). The goal is to reduce the CEP for 30-kilometer shot two orders of magnitude, from the current CEP of about 250 meters to only a few meters. Although the modified rounds will be more expensive than standard unguided rounds, they will be cost-effective because fewer rounds will be needed per target and the logistical burden of storing, transport and handling will be lower for the mission. The resulting increase in the rate of successful hits and reduction in the rate of unwanted hits has given this concept the name competent munitions.

Several different approaches to competent munitions are currently being explored: auto-registration, range only correction, as well as combined range and crossrange correction. In the auto-registration concept, a test round capable of communicating its impact point back to the gun is launched periodically so that appropriate corrections can be made to the gun inclination and direction. This helps to account for consistent atmospheric unknowns, such as wind and temperature. Range only correction requires single axis control authority. The simplest idea utilizes a drag increasing spoiler, which can be actuated by the controller to correct the range after intentionally overshooting the round. Range and deflection concepts require two axis control authority, such as a movable canard actuation system.

The tendency of low drag projectile shapes to be aerodynamically unstable necessitates some method of stabilization. The two most common methods are gyroscopic stabilization by spinning and aerodynamic stabilization by mounting fins behind the center of gravity. Projectiles can also be flare-stabilized by using a profile with increasing cross-sectional area behind the center of gravity, but this incurs a drag penalty and is uncommon. Most spin-stabilized projectiles use a profile with a section of decreasing cross-sectional area leading to the base, called a boattail. A boattail will

decrease drag, but increase the static instability of a projectile. Two axis controllers typically require that the fuze of a spin-stabilized projectile be “despun” to provide azimuthal or roll authority for the actuator. Despinning can be partial or complete. Complete despinning seeks to give total authority over the azimuthal orientation in inertial space, while partial despinning significantly reduces the spin rate of the fuze relative to body of the projectile, but does not give authority over the azimuthal orientation. GPS signal acquisition and IMU stabilization requirements also place constraints on the fuze spin rate.

In addition to difficulties of developing miniature avionics capable of handling the high-g operating environment, there has been difficulty in designing mechanically reliable and cost effective aerodynamic control actuation schemes. In order to minimize impact to the handling and loading procedures and equipment, all of the electronics and mechanical actuators must fit inside a standard fuze, which has an 8.5 cubic inch external volume. Previous attempts have been based on movable canards, such as in the CHAMP [17] concept, which require expensive mechanical systems containing many moving parts. To date, such systems have proven to be unreliable and have required almost the full fuze volume for the actuation mechanism.

Non-canard based actuation, the subject of this thesis, has been explored before previously for small caliber (30mm) aircraft fired projectiles. McGinley [19] found that articulating the nose of a spin-stabilized projectile provides sufficient lateral acceleration for both air-to-air and air-to-surface guidance with small deflection angles. Unfortunately, the aerodynamic coefficients were estimated by treating the nose and aft sections of the projectile as independent, a grossly incorrect assumption as will be shown in Chapter 4.

Past concepts for two axis control have required both direct azimuthal and lift magnitude control. Most frequently, variable deflection canards are mounted on completely despun fuzes, as in the CHAMP concept. Draper Laboratory has envisioned a fixed-trim terminal guidance concept which gives two axes of control authority by modulating the azimuthal orientation of a fixed normal force, as developed by Gracey, et. al. [12] for maneuvering re-entry of strategic missiles. By fixed lifting force, it

is not intended to imply a constant normal force over the trajectory, but that the controller has no authority over the magnitude of the force. Such control schemes result in a spiraling trajectory, as Figure 1-1 depicts. Trajectory simulations have shown that a fixed-trim guidance concept is a viable and promising guidance scheme for competent munitions.

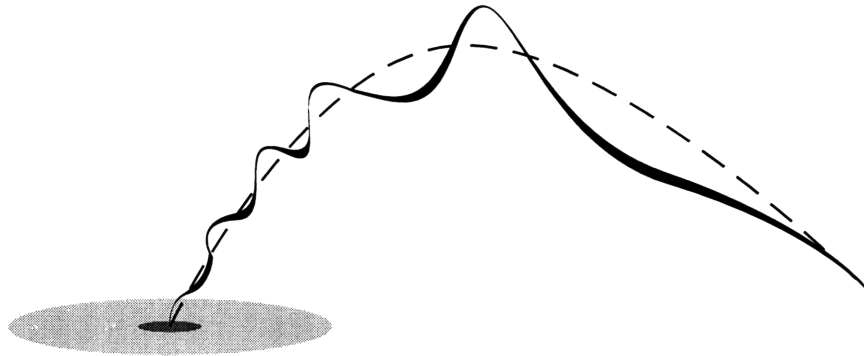


Figure 1-1: Depiction of Spiraling Fixed-Trim Trajectory

Once the requirement for generating a lifting force of controllable magnitude has been removed, it becomes possible to design asymmetries into the fuze shape which generate the necessary, but fixed, normal force. These asymmetries are the focus of this thesis. The next two sections will introduce the dynamic behavior of spin-stabilized projectiles and a figure of merit for evaluating design fitness.

1.2 Projectile Dynamics

An understanding of the rigid body dynamics of projectile motion is important to both the general goals of the aerodynamic design process and to the particular details of applying the results. Figure 1-2 establishes the aeroballistic coordinate system for describing forces and moments.

The reference geometric dimensions are defined as:

- L length of projectile
- D maximum diameter of projectile
- S area corresponding to maximum diameter
- I_{xx} rolling mass moment of inertia

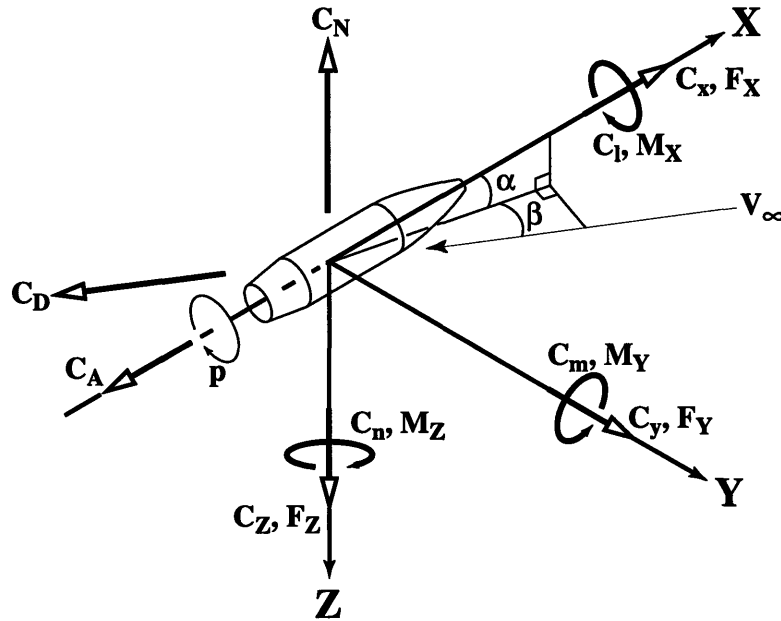


Figure 1-2: Aeroballistic Coordinate System

The flight conditions have the nomenclature:

- a_∞ freestream speed of sound
- M_∞ freestream Mach number
- T_∞ freestream Temperature (absolute)
- Re freestream Reynolds number, $a_\infty \rho_\infty L / \mu_\infty$
- Q dynamic pressure, $\frac{1}{2} \rho_\infty a_\infty^2 M_\infty^2$
- V freestream velocity
- p spin rate
- q pitch rate

The aerodynamic coefficients have the following definitions:

- C_A axial force coefficient
- C_N normal force coefficient, $\frac{N}{QS}$
- C_{N_α} normal force coefficient derivative, $\frac{\partial C_N}{\partial \alpha}$
- C_m pitch moment coefficient, $\frac{m}{QSD}$
- C_{m_α} pitch moment coefficient derivative, $\frac{\partial C_m}{\partial \alpha}$
- $C_{m_q} + C_{m_{\dot{\alpha}}}$ pitch damping moment coefficient sum, $\frac{\partial C_m}{\partial \frac{qD}{2V}} + \frac{\partial C_m}{\partial \frac{\dot{\alpha}D}{2V}}$

$$\begin{aligned}
C_n & \text{ yaw or Magnus moment coefficient, } \frac{n}{QSD} \\
C_{n_{p\alpha}} & \text{ Magnus moment coefficient derivative, } \frac{\partial C_n}{\partial \frac{pD}{2V} \partial \alpha} \\
C_l & \text{ roll moment coefficient, } \frac{l}{QSD} \\
C_{l_p} & \text{ roll damping moment coefficient, } \frac{\partial C_l}{\partial \frac{pD}{2V}} \\
C_Y & \text{ side or Magnus force, } \frac{Y}{QS} \\
C_{Y_{p\alpha}} & \text{ Magnus force coefficient derivative, } \frac{\partial C_Y}{\partial \frac{pD}{2V} \partial \alpha}
\end{aligned}$$

1.2.1 Dynamic Motion

After leaving the gun barrel, the projectile enters into a complex oscillatory motion about its center of mass. Conservation of angular momentum states that the spin (angular momentum) vector always tends to rotate toward the moment vector. An initial disturbance in pitch angle of attack will generate a pitch moment, but this pitch moment will result in rotational motion in the yaw plane due to the angular momentum of the spinning mass, as illustrated in Figure 1-3. The resulting yaw angle will cause the moment vector to dip below the yaw plane and the process repeats, producing counterclockwise rotation of the moment vector— classic gyroscopic motion. The spin vector will rotate about the original axis from which it was displaced because the gyroscopic couple was zero when the body was aligned with that axis. Thus the projectile will precess about the relative wind. In addition to this relatively low frequency precessional mode, there also exists a higher frequency nutational mode resulting from the total angular velocity not being parallel to a principle axis of inertia.

The tendency to precess about the axis of the relative wind causes the projectile to remain aligned with the trajectory, provided that the precession rate is high enough¹. This alignment tendency biases the precession such that there is a net yaw angle, called the yaw of repose. The yaw of repose is perpendicular to the plane defined by the direction of the change in flight path angle and the relative wind. Projectiles

¹This requirement establishes the upper bound on the spin rate for stabilization. The precession rate should be much higher than the rate of change of the flight path angle

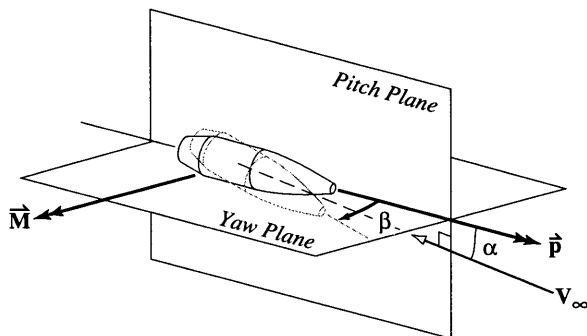


Figure 1-3: Gyroscopic Behavior of Spin-Stabilized Projectile

typically spin clockwise as viewed from the rear resulting in a negative yaw of repose, causing the trajectory to drift to the left.

1.2.2 Linearized Trim State

Properly stabilized projectiles precess at a rate which is high enough to allow the motion to be linearized about the precessional axis by time averaging the motion. Asymmetric aerodynamic forcing from the change in flight path angle and control forces bias the mean total pitch angle of the projectile. The projectile will oscillate about the instantaneous axis of zero moment, which is the trim axis for the linearized system. The yaw of repose results from the time averaged spin vector precessing in the vertical plane. The instantaneous yaw of repose can be calculated assuming steady precession:

$$\beta_{\text{repose}} = \frac{I_{xx} p \dot{\gamma}}{Q S D C_{m\alpha}} \quad (1.1)$$

where $\dot{\gamma}$ is the rate of change of the flight path angle.

The fixed trim aerodynamic actuation under consideration can be modeled as a zero-offset moment coefficient C_{m_0} and a normal force coefficient C_{N_0} . The normal force vector generated by the geometric asymmetry and the axis of revolution define the asymmetry plane. For mirror symmetric asymmetries, this is simply the lateral symmetry plane. The zero-offset moment results in a linearized trim angle of attack in the asymmetry plane, as verified in Appendix A.

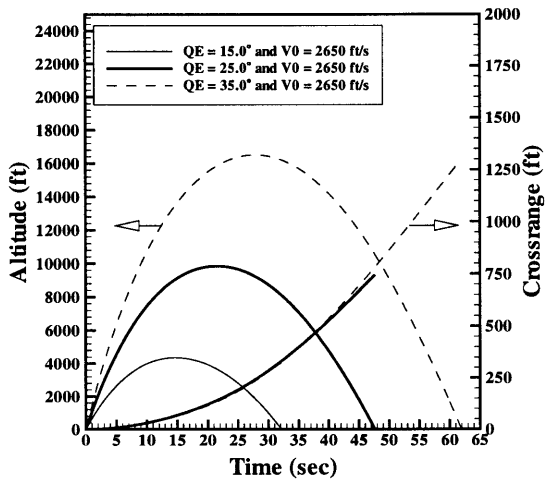
$$\alpha_{\text{trim}} = -\frac{C_{m_0}}{C_{m_\alpha}} \quad (1.2)$$

1.2.3 Ballistic Trajectory

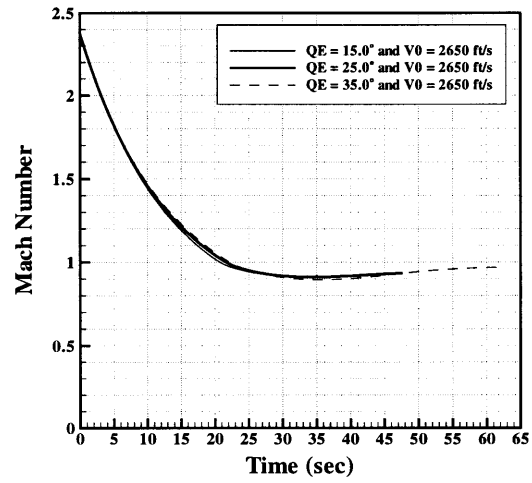
The ballistic trajectory of the projectile determines the mission profile of the vehicle. The nature of the trajectory is important for the design of aerodynamic actuation, as it determines the fundamental aerodynamic similarity parameters Mach number and Reynolds number. While aircraft are often designed for a single design point, consisting of a single Mach number and Reynolds number, projectiles must be designed for a specified time distribution of Mach numbers and Reynolds numbers.

The trajectory resulting from an initial velocity of 2650.0 ft/s, a quadrant elevation (launch inclination) of 25.0 degrees and a spin rate of 255 Hz has been used as a nominal trajectory. Figure 1-4 gives some outputs of interest calculated with a modified point mass model.

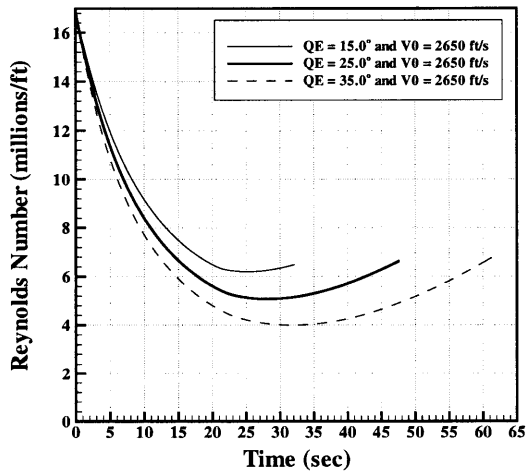
The effect of quadrant elevation on the behavior of the ballistic trajectory has an important consequences for trajectory control. The three quadrant elevations computed have widely varying altitude profiles and a four mile downrange variation, yet they produce trajectories with nearly identical Mach number and crossrange distributions. The invariant Mach distribution is a rather fortuitous circumstance because it makes the aerodynamic performance of the control actuator inherently robust to variations in the quadrant elevation due to the relative insensitivity of aerodynamic performance to Reynolds number for projectiles of this type. The dynamic pressure distribution, while varying moderately over the three quadrant elevations, maintains form, indicating that the optimal design solution for one trajectory will most likely not be too far from the optimal for other trajectories, with performance degradation being an unavoidable result of shorter flight time.



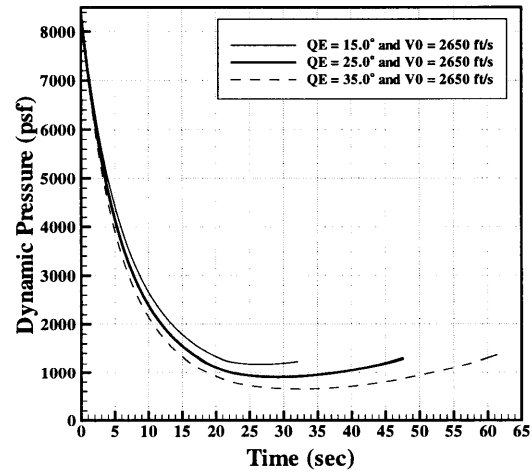
(a) Altitude and Crossrange



(b) Mach Number



(c) Reynolds Number



(d) Dynamic Pressure

Figure 1-4: Behavior of a Typical Ballistic Trajectory

1.3 Figure of Merit

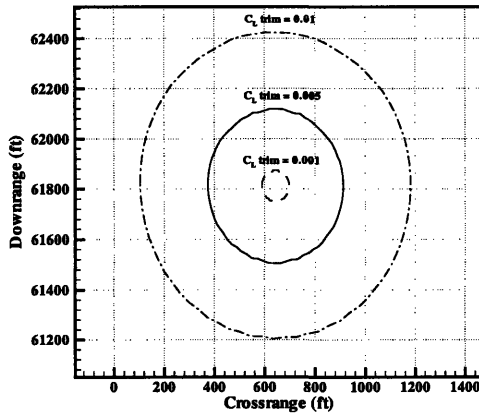
The purpose of the figure of merit is two-fold. First, it should provide a simple means of evaluating the fitness of a given configuration by bypassing the need to run numerous trajectory simulations. This purpose leads us to formulate the figure of merit in terms of aerodynamic coefficients, which allows us to move directly from aerodynamic characteristics to an indication of relative dynamic performance. Second, together with the parameterization of the configuration, the figure of merit should facilitate the collapse of data. The figure of merit encapsulates the dynamic behavior of the design and casts it in the language of aerodynamics.

The broad range of Mach numbers experienced by the projectile over its trajectory and the varying relationship between the distribution of Mach numbers and the launch conditions governing the trajectory make it difficult to define a concise and unambiguous figure of merit, as we can often do for single point designs. A compromise is made between accuracy and utility by choosing a point figure of merit which does not assume a Mach distribution, but augmenting the figure of merit with information about Mach sensitivity.

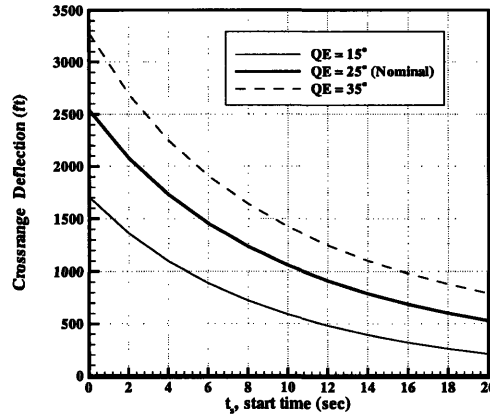
The figure of merit chosen is the trim lift coefficient, $C_{L_{\text{trim}}}$, which is derived from the linearized trim state. The yaw of repose is not included in the “trim” coefficient, it represents the linearly independent reaction to the control moment. The trim lift coefficient is chosen because it is the force perpendicular to the trajectory, to which the relative wind is tangent. The yaw angle due to control is given by Equation 1.2, with which the trim lift coefficient can be written:

$$C_{L_{\text{trim}}} = (C_{N_0} + C_{N_\alpha} \alpha_{\text{trim}}) \cos \alpha_{\text{trim}} - C_A \sin \alpha_{\text{trim}} \quad (1.3)$$

The trim lift quantifies accurately the effectiveness of a given design at a single Mach number, but it does not quantify the resultant crossrange performance. Crossrange performance prediction requires knowledge of how the design behaves over a range of Mach numbers, which is expensive to estimate with enough accuracy to legitimize a figure of merit requiring a Mach distribution.



(a) Typical Envelopes ($t_s = 10$ sec)



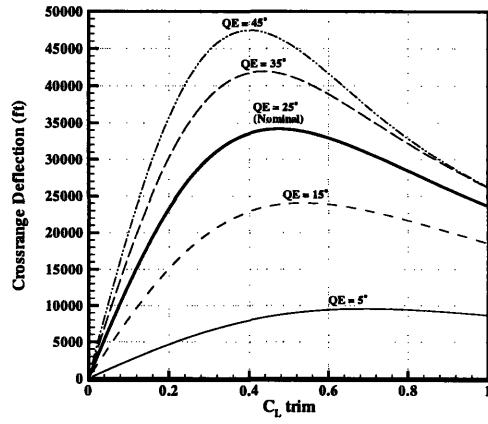
(b) Variation with Start Time

Figure 1-5: Maneuvering Envelope Behavior

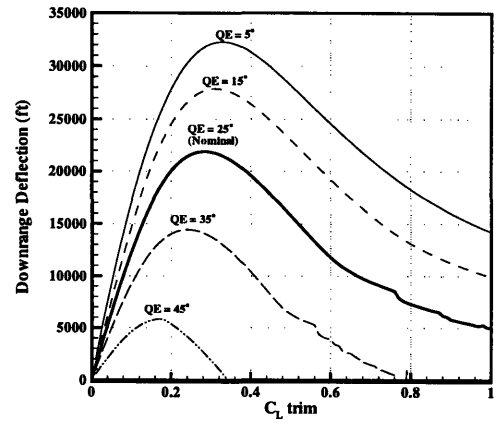
A maneuvering envelope, also referred to as a footprint, for a given actuator can be generated by simulating the trajectory for a number of azimuthal orientations of the asymmetry. Figure 1-5a shows some typical maneuvering envelopes for several values of $C_{L_{trim}}$, generated by choosing a constant $C_{L_{trim}}$. Figure 1-5b reveals the sensitivity of the maneuvering envelope to the time of control initiation, referred to as the start time, t_s . The importance of acquiring control and maneuvering at the earliest time can clearly be seen. More than half of the ideally available crossrange deflection will be lost if the navigation system requires ten seconds to stabilize.

The effect of $C_{L_{trim}}$ magnitude on maneuvering performance is shown in Figure 1-6. Range deflection is proportional to $C_{L_{trim}}$ for small values, as would be expected, but reaches a maximum and rolls off at larger values. The nonlinear behavior results from induced drag penalties due to the higher trim yaw angles. It is seen from the figure that the location and magnitude of the maximum is a dependent on the quadrant elevation.

Knowledge of the Mach sensitivity of $C_{L_{trim}}$ is important to the design of the aerodynamic asymmetry because geometric asymmetries can be devised to exploit features of compressible flow, such as transonic sensitivity. The relative influence of $C_{L_{trim}}$ at a particular Mach number can be gauged by calculating the maneuvering



(a) Crossrange Deflection



(b) Downrange Deflection

Figure 1-6: Range Variation with $C_{L\text{ trim}}$

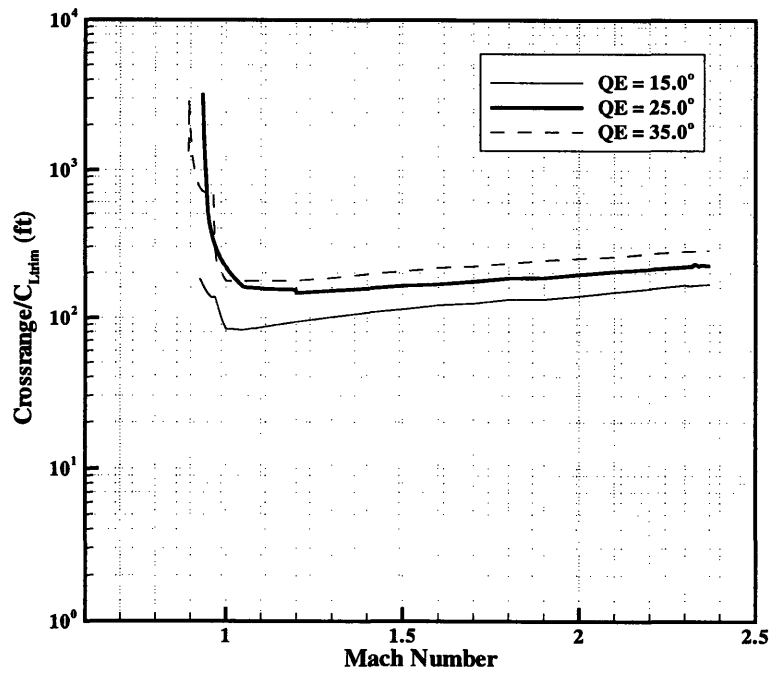


Figure 1-7: Crossrange Sensitivity to Mach Local $C_{L\text{ trim}}$ Perturbations

envelope resulting from a test $C_{L_{trim}}$ distribution which biases that Mach number. The test function is zero everywhere except for a linear spike centered at the Mach number of interest. The resulting Mach sensitivity distribution was found to be linear for small perturbations, that is, for small spike magnitudes, so the deflection is divided by the perturbation to give a quantitative sensitivity estimate.²

Figure 1-7 shows the crossrange deflection Mach sensitivity of several trajectories. Delayed control produces identical sensitivity curves except that the curves drop to zero at the Mach number corresponding to the start time, which can be determined from Figure 1-4b. The curves are characterized by a transonic peak near Mach 0.90, a low supersonic minimum near Mach 1.1, and a high supersonic peak near Mach 2.4. The transonic peak substantially dominates the high supersonic peak for the two higher quadrant elevations, but the peaks are of the same strength for the shallow trajectory.

The trim lift coefficient is held constant, regardless of the force distribution, so that the sensitivity distribution reveals the sum of three weighting factors: time, distance and dynamic pressure. The more time the projectile spends near a given Mach number, the more sensitive the range deflection will be to the trim lift coefficient at that Mach number. The majority of the flight time occurs at transonic Mach numbers, as seen in Figure 1-4, due to the terminal velocity of the drag profile, lending a strong transonic sensitivity to the trajectory. The greater the distance left to travel, the more effective a small heading displacement will be, biasing high supersonic Mach numbers which occur just after launch. Finally, the greater the dynamic pressure, the greater the actual force acting on the projectile. This again biases the high supersonic Mach numbers, especially just after launch when the atmospheric density is the greatest. Thus, the range sensitivity to Mach perturbations of the trim lift coefficient indicates that control actuation will be most effective in the transonic region.

²If dynamic response were linear, or approximately so, then the deflection resulting from an arbitrary $C_{L_{trim}}$ distribution could be estimated with the integral $\int \sigma(M)C_{L_{trim}}(M)dM$ where $\sigma(M)$ is the sensitivity distribution, which acts as an influence function.

1.4 Contributions

The developments of the thesis provide the following specific contributions to the projectile aerodynamics and the guided munitions knowledge base, as represented by the bibliography.

- The crossrange deflection of the trajectory has a very strong sensitivity to transonic trim lift perturbations.
- Transonic critical behavior can be characterized by four modes related to the Mach dependent location of shocks on boat-tailed projectiles.
- The small angle of attack sign change in Magnus force and moment results from the contribution of the last 2% of a spinning boat-tailed projectile. This contribution dominates the net force and moment at small angles of attack, but the forebody contribution dominates at higher angles of attack.
- Sting mounted wind tunnel models affect the pressure recovery over the boattail region at transonic Mach numbers, producing large errors in the wind tunnel modeling of transonic critical behavior.
- Configurational asymmetries are inefficient. Only a very small percentage of the normal force generated by a configurational asymmetry can be retained as net normal force and moment due to losses incurred by the resulting pressure recovery and induced velocity.
- Configurational asymmetries increase the Magnus force and moment for positive lift fuze orientations and decrease the Magnus force and moment for negative lift fuze orientations.
- Relatively small scale deviations in boundary layer development can drive transonic critical behavior producing large resultant trim forces, which can work in concert with the transonic trajectory sensitivity to produce synergy in trajectory control.

- Differentially canted body-fitted strakes interact such that performance does not scale directly with the number of strakes, but an empirical design algebra for dual strakes can be written to simplify preliminary design.

1.5 Overview

Chapter 2 details selection, development and validation of the aerodynamic model. Chapter 3 examines the aerodynamic behavior of the baseline axisymmetric projectiles. Several behaviors important to actuator design are introduced and explained. Chapter 4 evaluates two configurational asymmetries for generating lift. Chapter 5 investigates leveraged actuation for lift generation. In Chapter 6, a straightforward torque generating feature is explored quantitatively. The investigations are then summarized in the conclusion.

Chapter 2

Aerodynamic Modeling

The flow simulation used to predict aerodynamic performance has three constitutive sub-processes: grid generation, flow solution and post processing. Additionally, the flow simulation process must be validated by comparison to experimental or other benchmark data. A significant portion of the effort has gone towards the development and validation of simulations for various geometries in the broad range of flight conditions represented by this problem. A major component of simulation development focused on grid generation and the particular difficulties associated with the configurations investigated. Grid resolutions must also be justified by assuring grid convergence. The solver was modified to include a spinning boundary condition with which to model the Magnus effect. The most efficient time step must also be determined experimentally, and depends on Mach number, grid resolution and flow features such as unsteady wake vortex shedding.

2.1 Requirements and Model Selection

Due to the cost of flow modeling with nonlinear field methods such as the Euler and Navier-Stokes models, it is important to determine what fluid mechanic behavior is necessary to be represented by the the flow model to avoid incurring undo cost. Field methods require discretization of the flow volume surrounding the surface. Enough volume must be included to have accurate and well posed far field boundary condi-

	Incompressible	Subsonic	Transonic	Supersonic	Hypersonic	Weak Shocks	Strong Shocks	Vorticity	Entropy	Viscous	δ^* Correction	Turbulence Model
Slender Body Theory				x								
Panel Method	x	x									x	
Full-Potential	x	x	x	x		x					x	
Euler	x	x	x	x	x	x	x	x	x		x	
Parabolized Navier-Stokes				x	x	x	x	x	x	x		x
Thin-Layer Navier-Stokes	x	x	x	x	x	x	x	x	x	x		x

Table 2.1: Hierarchy of Configurational Flow Modeling

tions. Linear singularity methods, such as the panel method, require only that the surface be discretized and therefore offer a substantial reduction in computational cost. Table 2.1 maps flow behavior which is properly modeled by the various flow models. While slender body theory is an analytic linear singularity model, the panel Method is the only numerical linear singularity model represented, as lifting-line and vortex lattice methods do not model thickness, which is a necessary parameter for slender bodies.

Slender body theory decomposes the supersonic flow over a slender body into an axial component and a crossflow component resulting from angle of attack. The crossflow is incompressible for the small angle of attacks for which the theory is valid, thus the predictions are independent of Mach number. The slender body predictions are as follows:

$$C_N = 2\alpha \quad (2.1)$$

$$C_A = C_{A_0} + \alpha^2 \quad (2.2)$$

where C_{A_0} is determined from the axial problem and the reference area is taken to

be the maximum cross-sectional area.

Slender body theory is not sufficient due to the necessity of modeling both attached and separated flows throughout the Mach range with spin-induced three-dimensional boundary layers and flow fields. The discontinuous and non-conservative nature of transonic flow over realistic projectile geometries necessitate the cost incurred by complex Thin-Layer Navier-Stokes models to predict aerodynamic behavior and performance.

The OVERFLOW CFD code, a robust structured Chimera (overlapped) Navier-Stokes solver developed at NASA, was selected for flow model implementation. Appendix B contains more detailed information about the flow solver and the suite of utilities that industrious workers from across the country have developed.

2.2 Grid Generation

The grid is the cornerstone of the flow model. Not only does the grid define the geometry of interest, but it also determines the quality of the resulting solution. Poor grids lead to inaccuracy and can hinder or prevent convergence by inducing numerical instability. Numerical instability can be exhibited by either an apparent bounded unsteadiness, which is non-physical in origin, or by divergence of the solution.

The overlapping grid system consists of an aggregate of structured finite-difference grids which together define the surface of the geometry and fill the flow volume to be modeled. With each individual grid there is an associated mapping, as represented by the grid metrics, which transforms the physical domain into the computational domain. The physical domain is that which defines the geometry and flow field, while the computational domain is a cube of evenly spaced points. This is typical of finite-difference computations where the transformation into the orthogonal and evenly spaced computational domain engenders straightforward and efficient numerical solutions.

Grid generation, in the finite-difference sense, determines a mapping which transforms a set of ordered points defining both the volume and the boundaries of the

flow field, including the surface geometry, into a cube of evenly spaced points. An overlapped grid system relaxes the boundary constraints by allowing the system of grids to define the boundaries as a whole, while each individual grid will typically have only one of its computational planes defining just a portion of a boundary. The mapping implicitly defined by the grid must be one-to-one. The grid lines should be smooth, orthogonal and excessive skewness should be avoided. Grid points should also be closely spaced in the physical domain in regions of high gradients in the flow field quantities.

The grid generation problem as posed in the overlapped framework is to determine the best possible aggregate of grids which allows the simplest individual grids to be assembled into a well connected overlapping set. It is often useful to describe configurational features with an individual grid or with a grid subset in such a way as the configurational geometry can be modified or removed easily for design studies. The following sections present the grid generation methodology employed.

2.2.1 Surface Domain Decomposition and Grid Topology

The surface must first be broken down into subcomponents which allow for structured finite-difference grid generation, this process is called surface domain decomposition. In general, the best approach is to start by discretizing control curves which define discontinuities and lines of high surface curvature in the geometry such as intersections, edges and chines. Surface grids can then be generated by marching grids away from the these control curves to become what are called seam grids because they stitch the patchwork of overlapped grids together.

This process is complicated when two separate control curves lie near each other, or touch. When this occurs, the general solution is to further break apart the control curves until the subregions are amenable to structured gridding. This is not always possible, however, depending on the admissible grid topologies. Triangular intersections are particularly difficult to reduce into amenable subregions and must either be modified to become a skewed quadrilateral or the region must be further subdivided into a diamond quadrilateral and a trapezoid.

The regions between the seam grids are then filled with block grids, such that the seam grids and block grids together cover entire surface. It is necessary for connectivity that all grids sharing boundaries overlap at least three cells and have similar cell volumes in the overlap zone.

Grid topologies must then be chosen that provide for simple grids which are easy to generate. Decomposition of the surface should be done while keeping the volume grids resulting from the surface grids in mind. It is important not to fight the requirements necessitated by structured finite-difference grids by attempting to generate a grid of ill-chosen topology. Because structured grids define a one-to-one mapping from a homogeneous cubic volume to the one which represents the geometry, it is best to choose a topology which is as close as possible to being a cube and it is necessary that the topology of a volume grid have six sides. It is good practice to visualize what sorts of deformations one would need to perform in order to wrap a rubber cube around the domain to be gridded.

The particularity of a given geometry often offers both troubles and opportunities which cause deviation from the above generalized approach to grid generation. The surface discontinuities of the baseline projectiles, which are merely bodies of revolution, fall naturally on grid lines such that a baseline axisymmetric projectile surface can be defined with a single grid. Troublesome areas can also be dealt with by gridding them only approximately, if the misrepresentation of surface geometry can be justified in terms of scale and overall flow field sensitivity to that region of the boundary.

2.2.2 Surface Grid Generation

Once the surface is decomposed and topologies are chosen, then the surface grids may be generated. For the geometries considered, it is possible to choose domain decompositions and topologies which allow the surface grids to be generated in cylindrical or cartesian coordinate systems with grid lines following constant coordinate directions, thus providing for orthogonality.

Axisymmetric Configurations

The axisymmetric body of revolution, which forms the foundation of all the configurations evaluated, can be gridded quite easily by discretizing the profile shape and revolving it one complete turn or one half turn, depending on whether a full three-dimensional calculation will be performed or a calculation assuming lateral mirror symmetry. The surface discontinuities will be provided for naturally by placing a grid point on the profile at the discontinuity location. This process will result in a grid with an axis singularity at the center of the fuze tip and at the center of the base where the mapping will not be one-to-one. These grid singularities are acceptable within the OVERFLOW solver suite and are treated by first order extrapolation. Figure 2-1 shows an axisymmetric surface grid, defining the computational coordinate system.

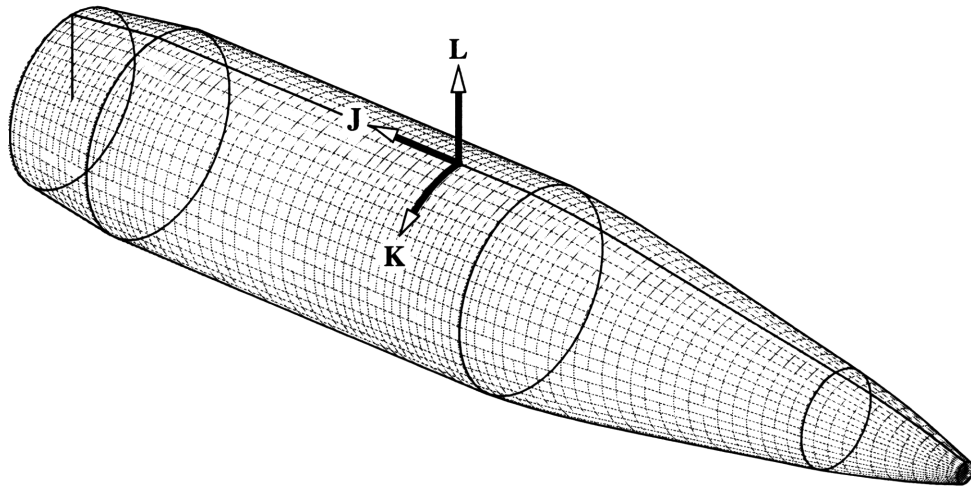


Figure 2-1: Axisymmetric Surface Grid and Computational Coordinate System

The distribution of profile points is chosen such that all surface discontinuities are exactly represented by a grid point and such that there is a greater density of grid points in regions where high flow gradients are expected, which also happen to be near surface discontinuities, where shocks tend to form. The distribution is specified by use of weighting functions and the one dimensional physical-space weighted grid generator discussed in Appendix C. Grid dimensions are written $JD \times KD \times LD$, where JD is the number of longitudinal points, KD is the number of circumferential

points and LD is the number of points in the surface normal direction.

Sliced Configurations

It is not possible to represent exactly a sliced configuration with a single grid. This difficulty arises from the discontinuity line defined by the intersection of the body of revolution with the slicing plane. The discontinuity line is itself closed, making it impossible to work into a single grid. Thus, multiple overlapped grids are required to accurately describe this region. To simplify, grid development for blunt nose geometries has been foregone.

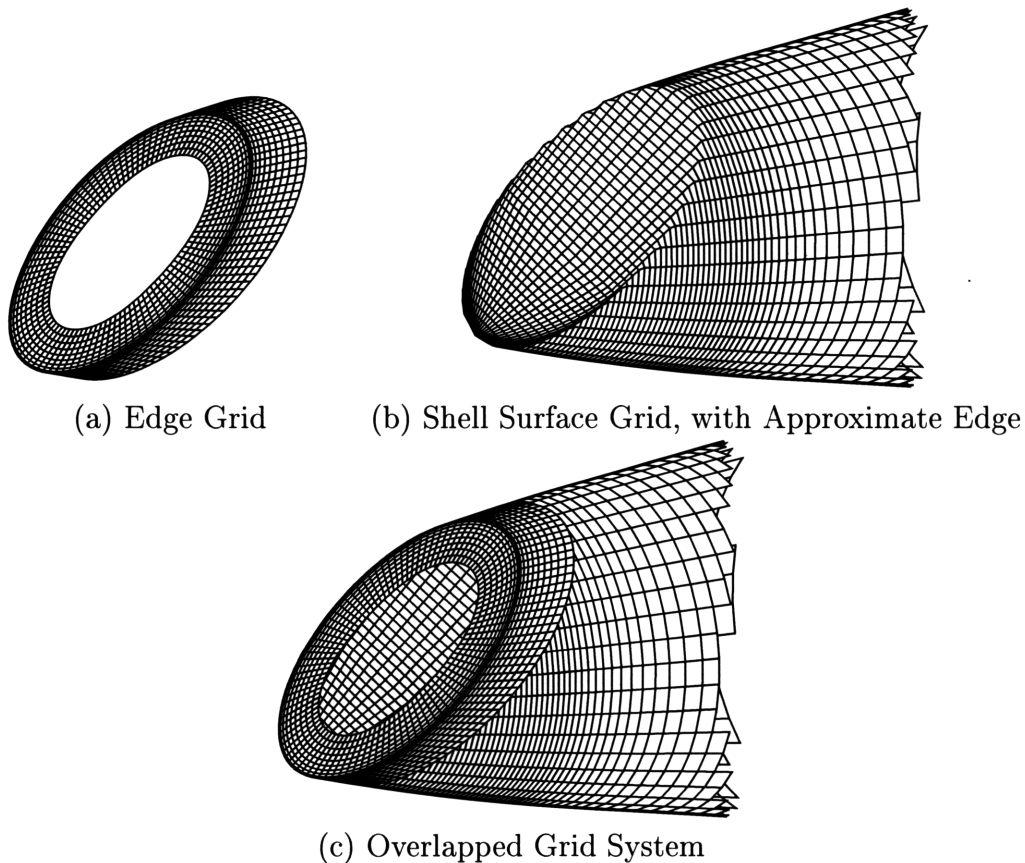


Figure 2-2: Component and Resultant Grids for Sliced Geometry

Figure 2-2 shows the individual and overlapped grids for the sliced configuration. As the figure shows, the slice is decomposed into a deformed body of revolution grid and an edge grid. The deformation was performed by projecting grid points from the

nominal body of revolution grid onto the slice plane. For the half-plane above the axis of revolution, the points are simply dropped straight down onto the slice plane. The nominal grid points lie on a circular arc which is at most a half-circle so that the projection is one-to-one, that is, the new set of points has no folds. For the half-plane below the axis of revolution, the circular arc of nominal grid points is more than a half-circle and the nominal grid points are transformed to lie on a half-circle whose diameter is equal to the width of the slice at that location before being project onto the slice plane. The edge grid defines the intersection of the slice plane and the body of revolution exactly (acting as a seam grid). The grid is marched away from the edge and projected onto the surface.

The underlying deformed body of revolution has several abnormalities which suggest that it would be unsuitable for use as a single grid. First, some quadrilaterals get wrapped around the edge, such that one side lies on the slice plane and one corner of the opposing side lies on the body of revolution. These quadrilaterals are ill-defined in that the surface normals defined by triangular decomposition are discrepant. Second, the projection process and transformation described in the previous paragraph results in high stretching close to the singular axis point. The first circumferential plane of cells away from the axis degenerate into triangles (as the axis condition necessitates), but the ellipsoidal shape of the slice intersection skews the cells more than would be desired. Both of these abnormalities are concealed by the edge grid, which results in an overlapped grid system that is well defined.

Despite the seeming inappropriateness of the underlying deformed body of revolution, the flow solver was found to be robust to the abnormalities under the whole Mach range of interest. A comparison was made with the overlapped grid predictions and was found to be in good agreement, which made it a cost effective alternative for the design investigations.

Bent Configuration

The so-called bent configuration is generated by linearly shearing an axisymmetric surface grid to produce an approximation to a deflection type bending. Actuated

mechanisms for bending would most likely pivot the fuze section, such that the arc length, shape of the cross-sections (constant x , for example) and orientation of the blunt nose would differ from the geometry evaluated here.

Strakes

A single strake geometry is explored for design purposes. The geometry was chosen to simplify grid topology, but was conceived to be aerodynamically representative of the concept. Figure 2-3 depicts the geometry of a strake, as defined by a single grid. The viscous surface lies entirely on one computational plane. Again, the strake geometry and grid topology are chosen such that grid lines naturally define surface discontinuities. The grid could be improved by relaxing the lateral spacing in the surface overlap region, causing the grid to splay out laterally, but it was found that the connectivity was reasonable.

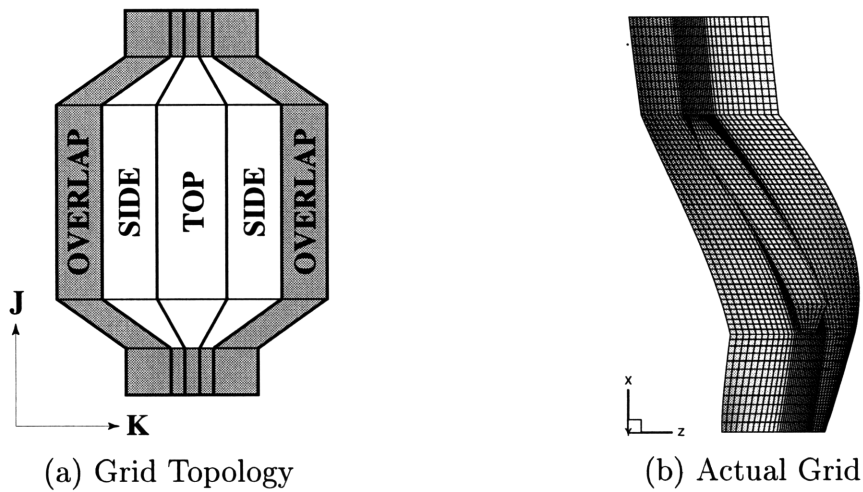


Figure 2-3: Strake Grid Topology and Geometry

2.2.3 Volume Grid Generation

Once the surface grids have been generated, the volume grids are generated by “growing” the grid from the surface with the hyperbolic grid generator HYPGEN [5], which is part of the OVERFLOW flow solver suite. Figure 2-4 shows a symmetry plane of

a typical volume grid. The volume has three regions: a surface region, a near field region and a far field region. These three regions are characterized by their grid spacing normal to the surface. The surface region has the highest density of grid points and thus contains the majority of the grid points. The wall spacing must be sufficient to capture the boundary layer velocity profile, as modeled by the turbulence model. For the Baldwin-Barth [2] turbulence model employed, the wall spacing should be about $y^+ = 1$, which was achieved in most configurations and flow conditions with a non-dimensional wall spacing of 10^{-6} . The near field region allows for greater grid resolution of the inviscid flow response to the displacement body. The relative sparseness of the far field region results from the smaller disturbances and milder flow gradients present in this region. The far field boundary was placed twenty reference lengths away from the surface to allow sufficient volume for dilation of transonic flow fields.

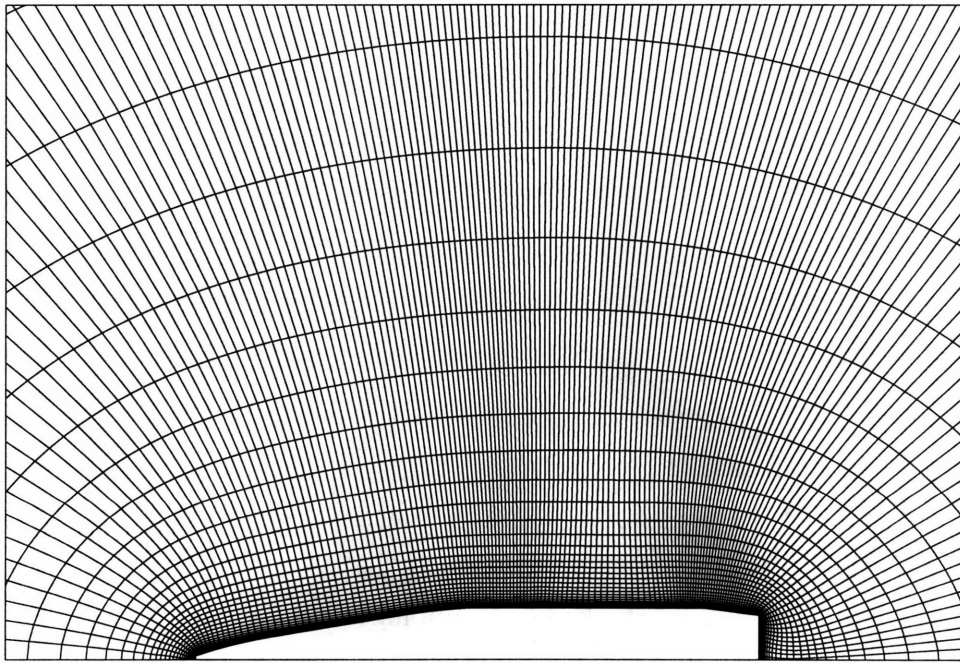


Figure 2-4: Half-Plane Showing Structured Volume Grid

2.2.4 Overlapped Connectivity

After all the volume grids have been generated, connectivity between the grids is calculated with PEGSUS [41]. Calculating overlapped grid connectivity is the process

of searching for the best interpolation stencil for each grid point in an overlapped region. An interpolation stencil consists of grid points from other grids and requisite weightings with which to perform tri-linear (linear three-dimensional) interpolation. Interpolation is the mechanism by which information is passed between the aggregate of grids.

The details of particular methods employed by PEGSUS will not be discussed, but the two requirements for good connectivity will be noted. First, there must be at least three cells overlap between adjacent grids. Second, the overlapping cell volumes must be similar. Quality of the connectivity is measured by how well balanced the interpolation stencils are in spatial configuration. In practice, reasonable connectivity can be obtain despite a region of disparate cell sizes, if they are well oriented. Furthermore, the coarser grid must be capable of adequately resolving the flow gradients.

2.3 Numerical Convergence

Numerical solutions must converge spatially as the density of grid points increases, and iteratively as the solution progresses towards steady-state, be it a constant or a limit cycle.

2.3.1 Spatial Convergence

Numerical discretization of complex flow fields usually result in approximations of second order accuracy in the discrete spacing, written $O(\Delta x^2, \Delta y^2, \Delta z^2, \Delta t^2)$, due to the truncation of the Taylor series approximation of the derivatives. Consistency requirements necessitate that truncation error tends towards zero as the spacing tends towards zero. Thus, the approximate solution should converge to the exact solution as the grid resolution increases. Grid resolution must be increased until the change in the predicted quantities becomes sufficiently small, at which point the grid is said to be converged.

The variations of the coefficients with grid spacing in the two orthogonal surface directions are given in Figure 2-5. Longitudinal calculations were performed with

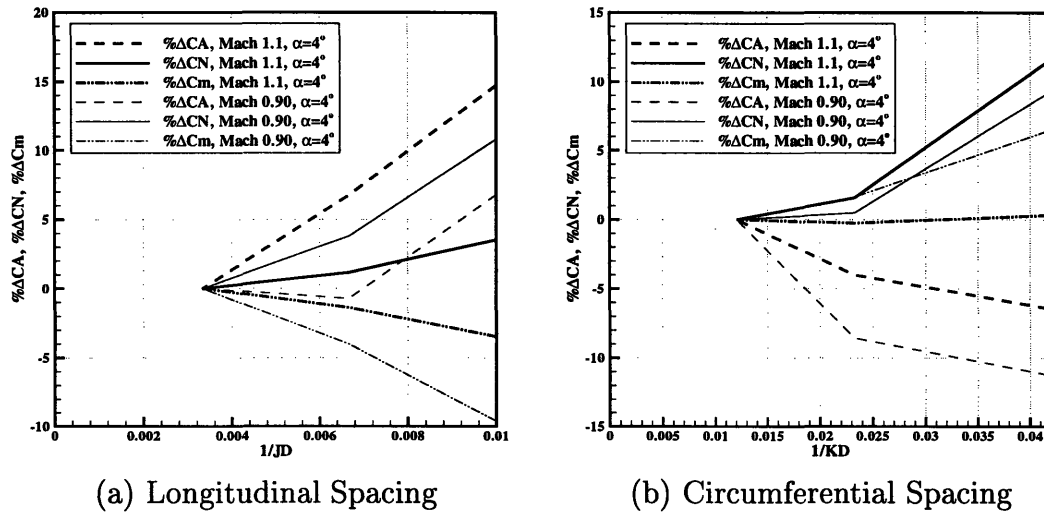


Figure 2-5: Spatial Convergence in Two Orthogonal Surface Directions

43 circumferential grid points and 100, 150 and 300 points longitudinally. Circumferential calculations were performed with 150 longitudinal points and 24, 42 and 83 points circumferentially. The force and moment coefficients generally tend to converge quadratically, as the error in numerical accuracy does, but there are some exceptions due to nonlinear changes in the flow field. Longitudinal refinement results in a decrease in the axial force, while circumferential refinement results in an increase. Similarly, longitudinal refinement results in an increase in pitching moment, while circumferential refinement results in a decrease, although pitching moment appears to be only weakly dependent on circumferential spacing for higher Mach numbers.

In practice, properly converged grids may not be used because the cost will impede the effectiveness of the computational model in the design process. Such cost saving measures must be used with good judgment and experience with the geometry at hand because the formulation of numerical approximations does not guarantee well behaved degradation of accuracy for grids far from being converged. Engineers often also utilize an intuitive but usually unrigorous principle that approximations will give fair predictions of trends, even when the predicted magnitudes are poor. With experience, poorly resolved grids can be useful during preliminary design studies for finding trends and approximate locations of maxima. The use of such lower order

approximations can be limited because shock locations and separation behavior are both strongly influenced by grid resolution and often have a strong influence on the solution.

2.3.2 Temporal Convergence

Steady-state solutions utilize local time step scaling for convergence acceleration. Typically, both a time step and a minimum required CFL are specified. Thus, as the time step is decreased a value will be reached below which the minimum CFL specified wholly determines the local time step. Increasing the CFL number in the outer field can abet solution convergence by accelerating the establishment of the outer inviscid flow which is often a strong driver of the viscous boundary layer region.

Time steps are determined by first attempting to use a time step of 1.0, then decreasing the time step an order of magnitude for subsequent attempts until the solution stabilizes. For well behaved steady-state solutions on moderate grid resolutions ($150 \times 43 \times 60$) it was found that a time step of 0.1 and a minimum CFL of 5.0 produces stable solutions for Mach 0.80 to about Mach 1.1 or so. Higher Mach numbers required a time step of 0.01 and a minimum CFL of 2.0.

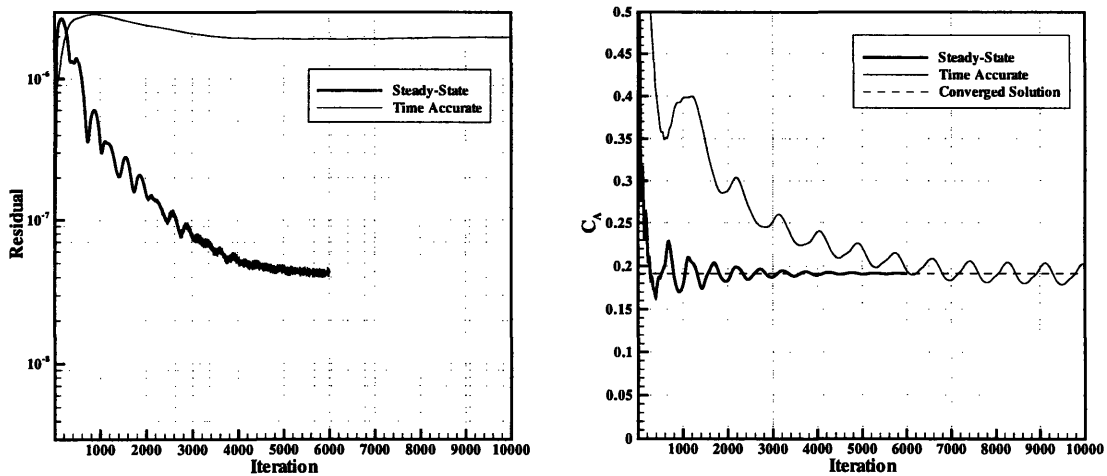
Time accurate solutions require a time step small enough to resolve the time dependent flow behavior and to maintain numerical stability. Transonic Mach numbers, near Mach 0.90, were found to converge for a time step of 0.001 for non spinning cases. Time accurate solutions with moving shocks require the use of the computationally more expensive block tridiagonal implicit factorization of the left hand side, as discussed in Appendix B, further increasing the cost. Both the ARC3D diagonalized form and the block tridiagonal were used to compute unsteady transonic solutions and were found to give identical predictions, being equally accurate in modeling the recirculating base flow which is responsible for the unsteadiness.

Maximum allowable time steps for both steady-state and time accurate calculations depend on grid quality and resolution as well as on the physical time scales of the flow problem. Grids of poor quality, containing skewed or highly stretched cells, can destabilize a solution requiring smaller time steps. Time steps must also be

reduced for fine meshes adding additional cost to solution refinement by increasing not only the per iteration cost from additional grid points, but by also increasing the number of iterations required.

Grid refinement in the boattail and wake regions tends to adversely affect solution convergence for transonic Mach numbers. Solutions often do not converge to constant values, but develop limit cycles. Coarser grids damp inherent physical unsteadiness and stabilize the solution, but may not yield accurate results. Validation studies show that the chosen grid resolutions have sufficient accuracy for preliminary design studies. Both fine grids and the spinning boundary condition discussed below were found to exacerbate unsteadiness at transonic Mach numbers and required time accurate time stepping.

Figure 2-6 compares two temporal convergence histories, both at Mach 0.91 and 4° angle of attack. The steady state solutions has been computed on a $150 \times 43 \times 60$ point grid, while the time accurate has been computed on a $300 \times 43 \times 60$ point grid. The time accurate time stepping was necessary for the higher resolution grid because steady-state time stepping did not converge to a solution. Notice that the two methods of time stepping converge close to the same average solution, adding confidence to the numerically stabilized solution obtained from coarser grids.



(a) Residual History

(b) Axial Force History

Figure 2-6: Steady-State and Time Accurate Temporal Convergence

Steady-state solutions take advantage of local time stepping which accelerate convergence by allowing a larger base time step to be used, which is then scaled with cell volume. The steady-state solution required a time step of $\Delta t = 0.1$ with a minimum CFL of 5.0, while the time accurate solution required $\Delta t = 0.001$. Converged solutions required 121 hours for the block tridiagonal time accurate computation, 38 hours for the ARC3D diagonal time accurate computation, and 12 hours for ARC3D diagonal steady-state computation¹. The steady-state solution required less time because fewer iterations were necessary to converge the solution. The time per grid point per iteration for the two algorithms is $103\mu\text{sec}/\text{pt}/\text{iter}$ and $17\mu\text{sec}/\text{pt}/\text{iter}$ for the block tridiagonal and the ARC3D diagonal algorithms. Machine dependent details are noted to illustrate the cost to compute each data point, which certainly plays a role in engineering cost analysis in terms of lead and turn-around times. The machine used is state of the art for the day.

2.4 Boundary Conditions

After the geometry and flow domain have been represented as a grid of appropriately chosen topology, the flow problem must be described physically through the selection of boundary conditions. Viscous surfaces have been modeled as adiabatic viscous walls, with pressure extrapolation. The Baldwin-Barth turbulence model has been used for the boundary layer flow. Far field boundaries are treated with a characteristic condition similar to Riemann invariants, utilizing free stream values for information flowing into the domain. Flow quantities on a singularity axis created by a revolved surface are calculated by first order extrapolation. A periodic boundary condition is used for the full three-dimensional calculations, but mirror symmetry across the x - z plane is also used in order to reduce the cost of some calculations, but only after full three-dimensional calculations verify that full three-dimensional effects can be neglected. Several calculations were performed for spinning shells by modeling the

¹CPU time on an Origin class Silicon Graphics Workstation. Run entirely in memory on a single 180 Mhz MIPS R10000 IP27 processor with a MIPS R10010 Floating Point Unit.

spinning surface with an imposed tangential velocity as described in Appendix B.

2.5 Validation

Several geometries were chosen for validation purposes based on the availability of experimental data in the literature. Pressure distributions are compared for the SOCBT configuration and integrated quantities are compared for the Mk 41 configuration.

2.5.1 SOCBT Configuration

The Secant-Ogive-Boattail (SOCBT) configuration proliferates the literature, both wind tunnel studies and numerical studies have been performed on the basic configuration and variants. Figure 2-7 depicts the basic configuration.

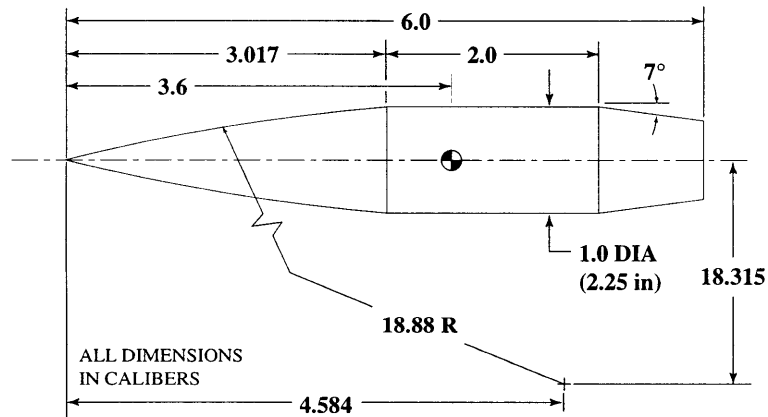
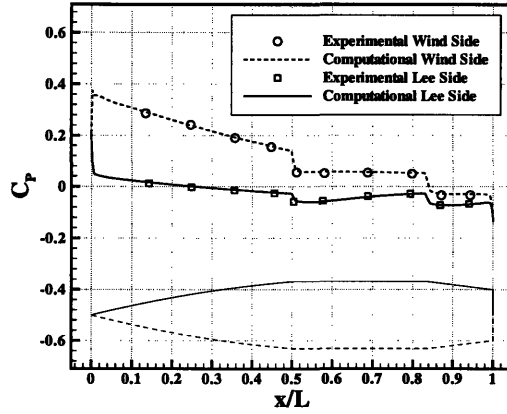


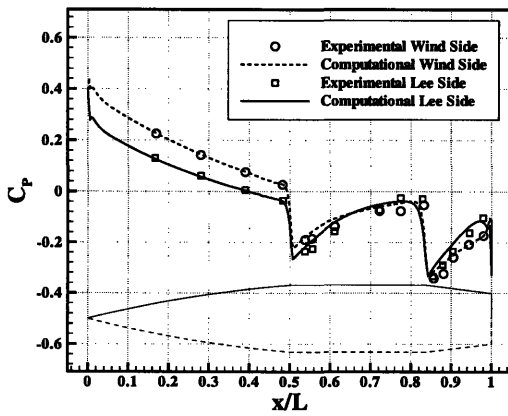
Figure 2-7: Basic SOCBT Configuration

Three non-spinning cases for which surface pressures measurements are available have been selected for comparison to the computational predictions. The comparisons are shown in Figures 2-8. The predictions compare quite well to experiment, especially at the higher Mach numbers. Prediction of flow acceleration over the ogive is excellent at all three Mach numbers and shock locations are captured to within the pressure tap spacing. The greatest discrepancies can be seen in the Mach 0.91 distribution, where the pressure increase across the ogive-cylinder junction shock is under predicted in

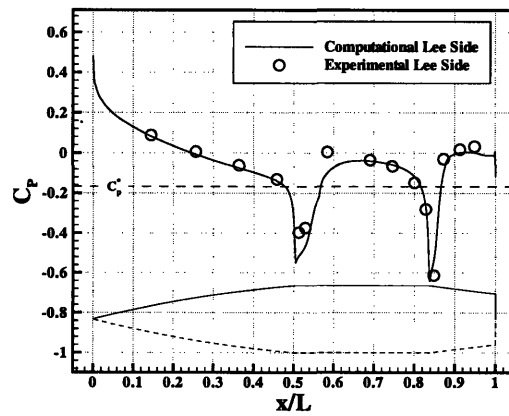
magnitude and the pressure distributions over the boattail do not quite agree, most likely due to sting effects..



(a) Mach 3.25, $\alpha = 10.4^\circ$ [26]



(b) Mach 1.1, $\alpha = 4^\circ$ [32]



(c) Mach 0.91, $\alpha = 2^\circ$ [25]

Figure 2-8: Pressure Distribution Comparisons for SOCBT Configuration

2.5.2 Mk41 5"/54 Configuration

The Mk 41 is a typical round, with a geometry which is very similar to the Mk 64 round on which the design investigations are based. Experimental data for the Mk 41 round was obtained from the Chadwick [4] paper and the Donovan [8] report. Figure 2-9 gives a qualitative comparison between experimental shadowgraphs and computational predictions of the density field. Shadowgraphs are visualizations of the second spatial derivative of density. Shock waves always appear as a dark line followed by a light line. The Mach 1.75 computational solution exhibits a slightly more rapid contraction of the wake density field, but it captures the wake shock in nearly the same location. The computational model does not incorporate smaller scale surface features such as firing rings and mechanical junction details. It can be seen that these details produce only faint disturbances in the Mach 0.95 shadowgraph, but more noticeable disturbances in the Mach 1.75 shadowgraph.

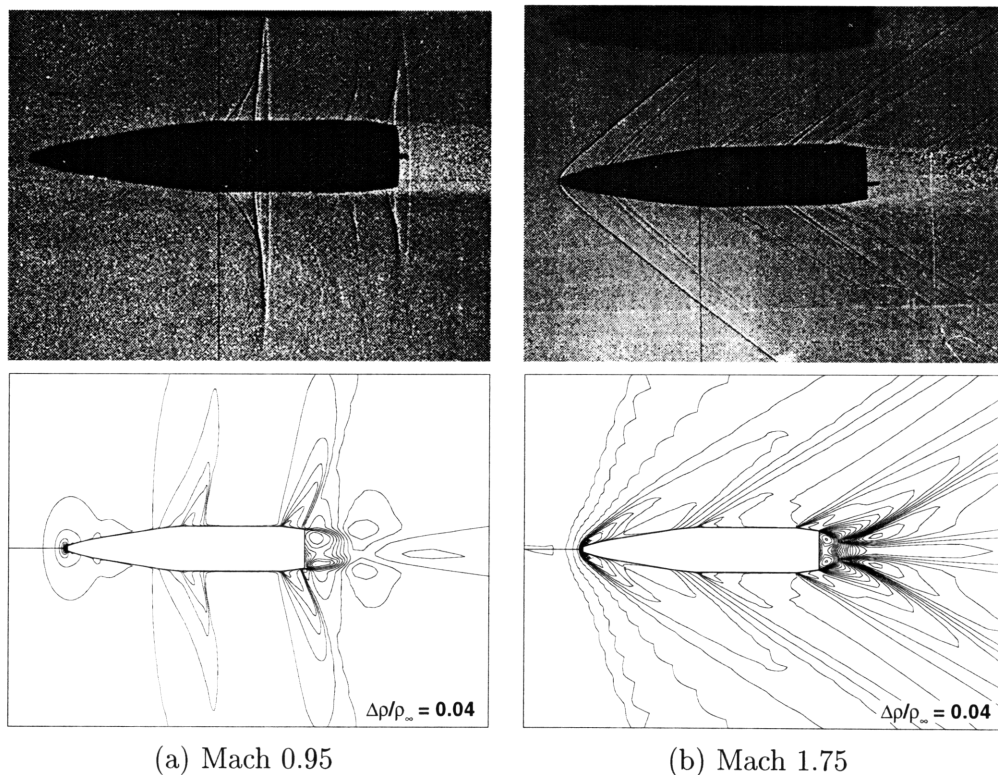


Figure 2-9: Qualitative Flow field Comparison. Top: Experimental Shadowgraphs [8], Bottom: Computational Density Contours.

Comparisons between integrated quantities of interest are shown in Figure 2-10. For the most part, the computations agree well with the experimental data, especially considering the imprecision of the available geometry data and flight conditions, which gives confidence to the modeling process.

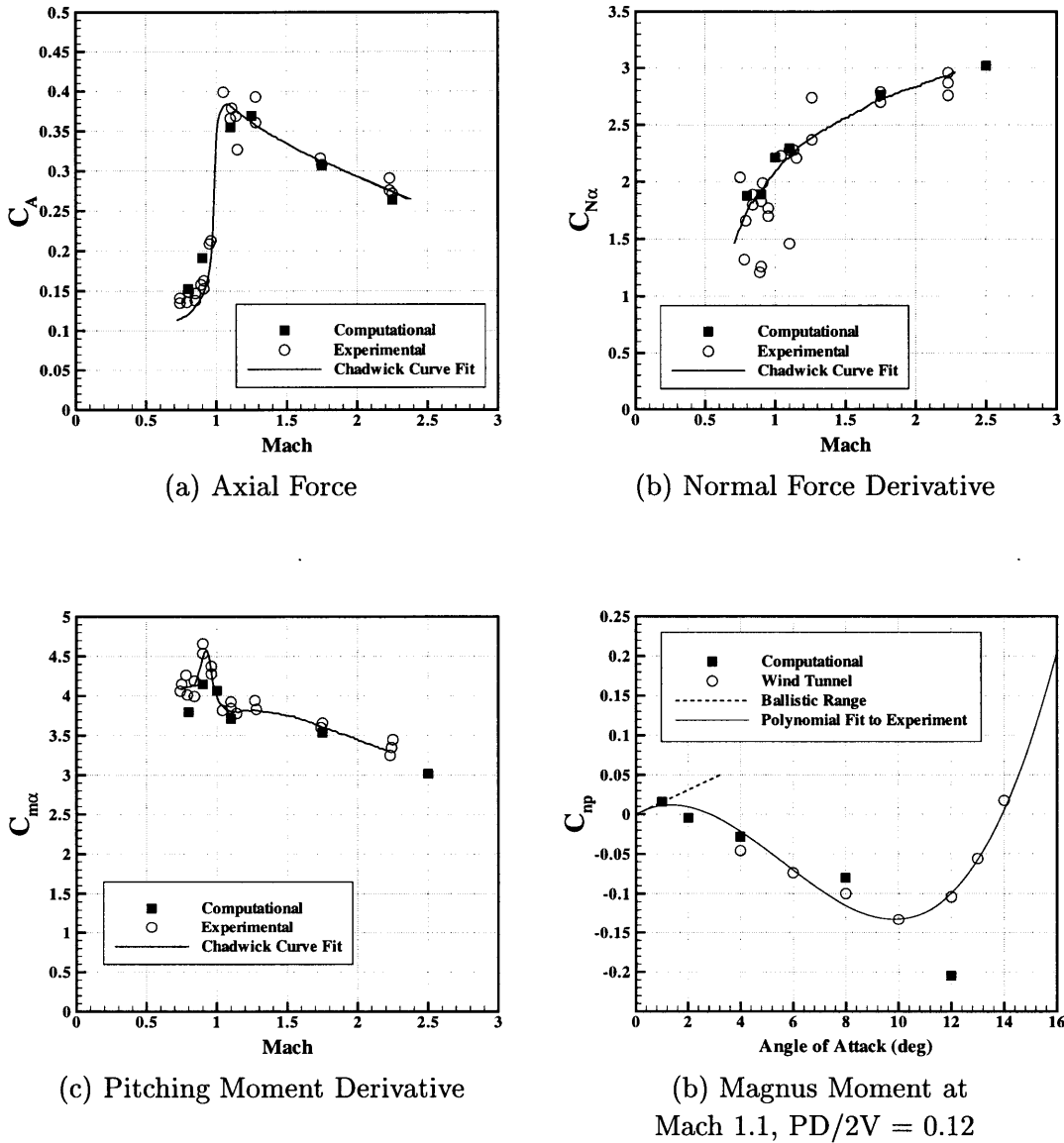


Figure 2-10: Comparison of Mach Behavior for Mk41 Projectile

Magnus moment predictions have long been a pacing item for modeling flow fields around spinning projectiles. The Magnus force results from spin induced thickening of the boundary layer on the side of the projectile for which the spin velocity opposes

the crossflow wind velocity. The laterally asymmetric boundary layer generates a side force and moment.

Although the Magnus force is only a tenth of the magnitude of the normal force, the concomitant Magnus moment is a critical parameter in dynamic stability of projectiles, particularly in low temperature, high density environments. Magnus effects are difficult to model accurately due to the complex three dimensional turbulent boundary layer flows from which the force finds root.

The introduction of the spinning boundary condition tended to destabilize the solution. The unsteadiness exhibited by the computational solution could very well be physical in root, as it is local to the boattail and wake region where previous experimental investigations have observed several different modes of unsteadiness. The computations compare fairly well at this Mach number, capturing the first sign change and predicting reasonably similar magnitudes.

The reduction of Magnus moment magnitude at high angle of attack and subsequent sign change is not even hinted at by the computations. At higher angles of attack the crossflow becomes stronger, containing larger gradients in the flow variables, and crossflow separation becomes an issue. Qualitatively, the grids used for the computations appear somewhat too coarse for accurately capturing these changes. The turbulence model also becomes an important factor in the prediction of separation and re-attachment for the complex three-dimensional boundary layers dominating these flows. Turbulence models evolved out of empirical descriptions of particular flows, which limits modeling accuracy for flows that were not in mind while the models were formulated.

The flow predictions have a primary goal of filtering and evaluating preliminary design concepts, a task the developed flow model appears more than capable of accomplishing with useful precision, as validated by experimental comparisons. Chapter 3 mentions additional blind comparisons with unreleasable data which have been performed and show even stronger comparisons, particularly given the greater precision of available details about the wind tunnel model and flow conditions.

Chapter 3

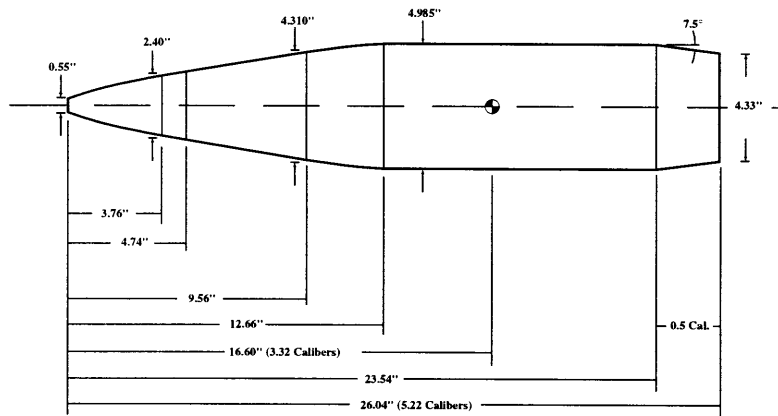
Baseline Aerodynamic Behavior

The aerodynamic behavior of the axisymmetric profile establishes a baseline for asymmetry design and reveals characteristic behavior of projectile aerodynamics which is also exhibited in the aerodynamic characteristics of configurational asymmetries. In fact, the next chapter will show that the pitch moment slopes and normal force slopes are essentially unaltered by the configurational asymmetries under consideration. An understanding of the baseline behavior is also important to the analysis of the aerodynamic mechanisms which the asymmetries actuate and can give insight into identifying and targeting such mechanisms.

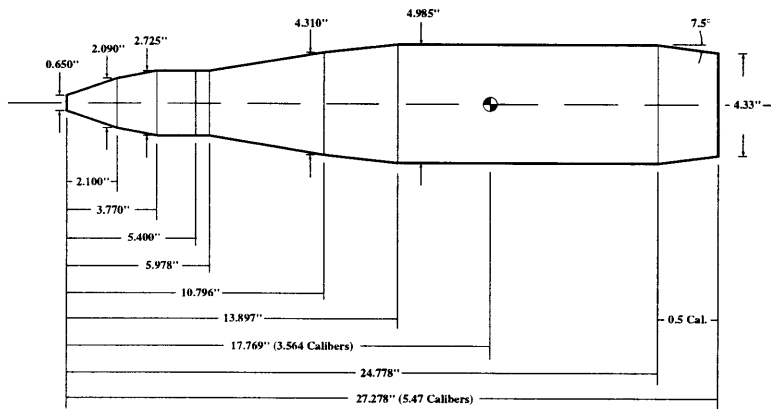
3.1 Baseline Profiles

Two baseline configurations are used in the investigations, the standard Mk 64 profile and a modified profile referred to as the CMATD profile. The profiles differ only in fuze design. The fuze of the standard profile is typical of 5" projectiles, while the CMATD fuze is longer and angular, having been modified to increase internal volume and provide a mounting point for canards.

The standard configuration has been the primary profile for investigation of asymmetries, while the CMATD profile is introduced to investigate the effects of sting mounting wind tunnel models as well as to illustrate the effects of fuze shape on aerodynamic behavior.



(a) The Standard Mk64 Configuration



(b) The CMATD Configuration

Figure 3-1: Baseline Profiles

3.2 Mach Behavior

The effects of compressibility on projectile aerodynamics produce variations as large as 100% in the baseline aerodynamic coefficients and are the driving factor in asymmetry design and performance as well as an important stability parameter. The variations of the definitive baseline aerodynamic parameters with Mach number are given in Figure 3-2.

The aerodynamic coefficients of the two baseline profiles behave similarly with Mach number, as might be expected for geometries that deviate only in fuze profile, differing consistently by about 5%. Examination of the normal force and pitch moment development reveals that the CMATD configuration generates additional lift in the fuze section which contributes to the pitch moment before the additional lift is lost while recovering to freestream over the afterbody. The longer fuze of the CMATD, which makes the overall length of the shell 5% greater, also contributes to the higher pitch moment with the lower normal force.

The two profiles have drag curves of identical shape, with the CMATD dissipating more energy supersonically due to additional losses from shocks induced by discontinuities in the fuze profile and thus producing more drag.

3.3 Transonic Critical Behavior

The computations captured the transonic critical behavior exhibited by boat-tailed projectiles, as observed in wind tunnel and ballistic range measurements as well as previous computational investigations [32]. Measurements indicate that as the Mach number increases from subsonic values, the pitch moment rises rapidly to a critical point before dropping sharply to a second critical point from which the pitch moment rises once again. Similarly, the normal force will drop rapidly to a first critical point before rising sharply to a second critical point from which it drops again.

The second critical point, consisting of the second rise in the pitch moment and the corresponding second drop in the normal force, are usually less severe or en-

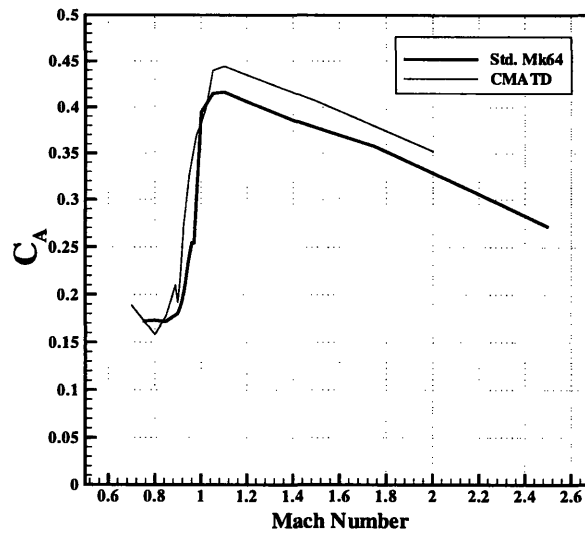
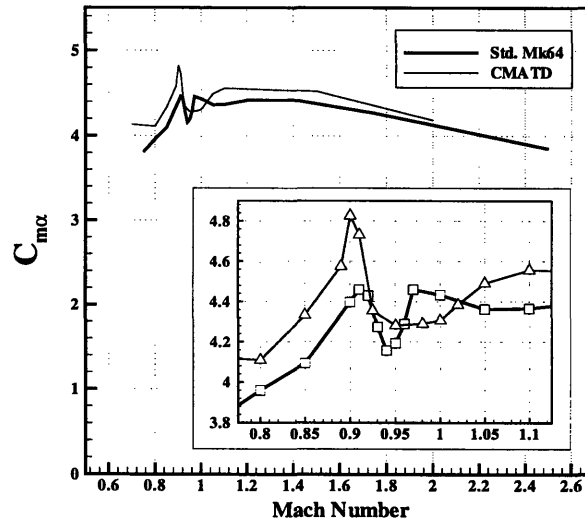
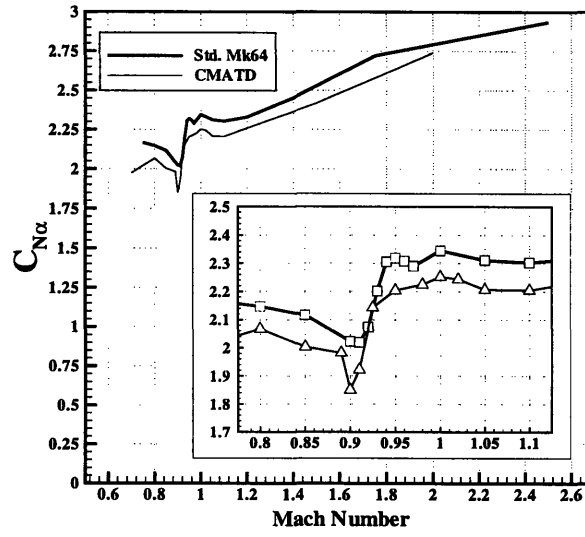
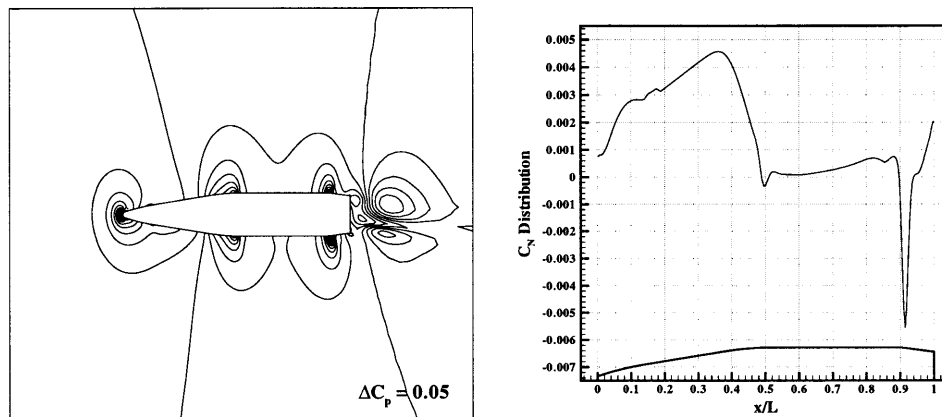


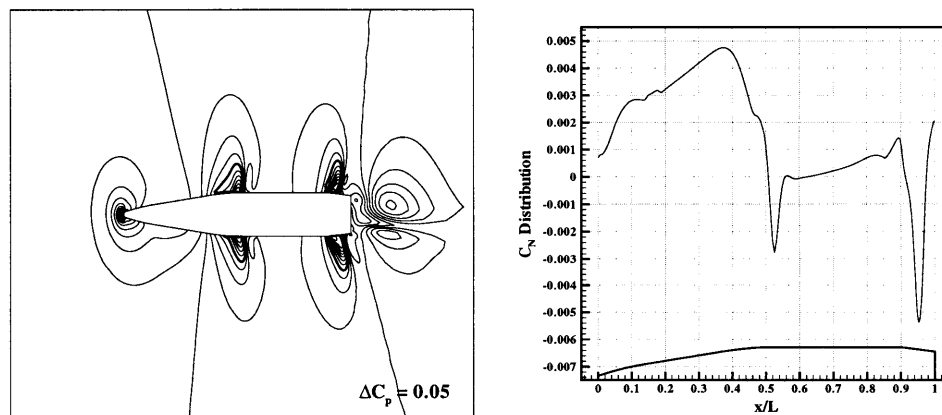
Figure 3-2: Mach Behavior of Baseline Configurations

tirely washed out in comparison to the first critical points. The standard Mk 64 and CMATD modification both exhibit this behavior, although with individual nuances, as can be seen in Figure 3-2.

The flow fields and normal force distributions for a subsonic Mach number and for the first critical point are given in Figure 3-3. The computations were performed on the standard Mk 64 profile. Thicker contours highlight sonic lines.



(a) Mach 0.85, $\alpha = 4^\circ$



(b) Mach 0.91, $\alpha = 4^\circ$

Figure 3-3: Transonic Critical Behavior Part I

Figure 3-3a illustrates the behavior at a high subsonic Mach number. The ogive-cylinder junction and cylinder-boattail junction can be seen to seed shock formation, but the flow field is almost everywhere subsonic, containing no substantial supersonic

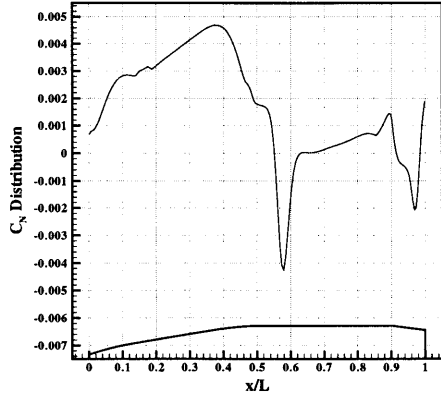
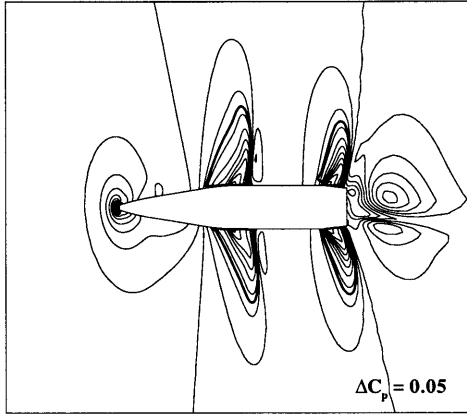
pockets.

Figure 3-3b illustrates the first critical point with a fully transonic flow field containing pockets of supersonic flow and well developed shocks. The two dimensional pitch plane flow field cross-sections shown render the three dimensional shock disks as seemingly separate entities on the upper and lower surfaces which, although obviously not separate, clearly indicate how the inclination of the shock disk effects the pressure distribution over the projectile. The first critical point is characterized by the shock disk in the cylindrical section sitting very close to the ogive-cylinder junction while the boattail shock disk has been released from the cylinder-boattail junction and sits at an angle so that the shock disk is located slightly further aft on the lower surface.

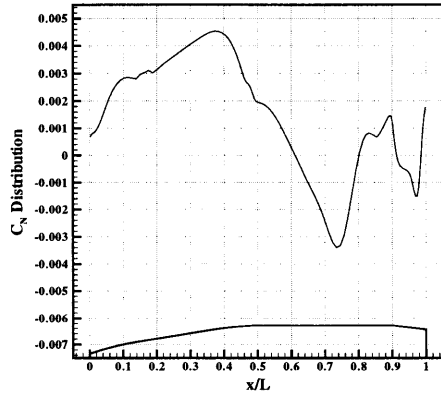
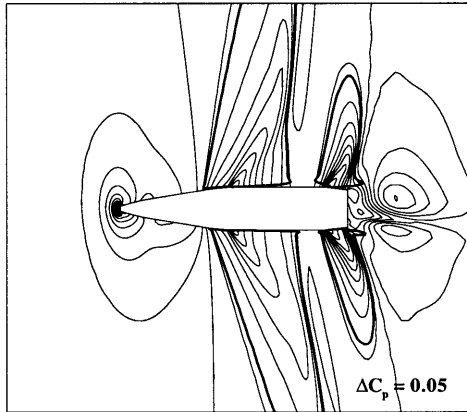
Although more lift is generated over the ogive at Mach 0.91, this additional lift is mostly lost through a stronger shock at the cylinder-fuze junction. Again, more lift is generated over the cylinder-boattail transition at Mach 0.91, but is more than lost through the exaggerated cant of the boattail shock disk. Thus, the formation and location of shocks causes a net decrease in the normal force generated at the first critical point, producing the characteristic drop. The deficit in normal force due to local production of a down force in the boattail results in an increased pitch moment, producing the characteristic rise.

Figure 3-4 illustrates the second critical point and egression from the critical regime. The flow field of the second critical point shown in Figure 3-4a shows that the ogive-cylinder shock disk has started to move away from the junction into the cylinder section, while the boattail shock has moved downstream, becoming attached to the base. The attachment of the boattail shock onto the base attenuates the local down force generation, accounting for the rise in normal force, and reduces the couple resulting from the down force, accounting for the drop in pitch moment.

Figure 3-4b shows how the flow field egresses from the transonic critical regime. As the Mach number increases, the supersonic pockets become larger causing shocks to weaken and move downstream. At Mach 0.97 the supersonic pocket originally formed over the ogive-cylinder junction has expanded over most of the cylinder section, and the whole subregion has significantly weakened. The shock has moved past the center



(a) Mach 0.94, $\alpha = 4^\circ$



(b) Mach 0.97, $\alpha = 4^\circ$

Figure 3-4: Transonic Critical Behavior Part II

of gravity of the shell, redistributing local normal force generation causing an increase in pitch moment. The loss in normal force after the second critical point results from the shorter recovery length available between the cylinder shock and the boattail shock.

Looking again at the pitch moment variation with Mach number in Figure 3-2, it can be seen that the CMATD has a larger first critical point occurring at a slightly lower Mach number with a softer, smaller second critical point. Examination reveals that although additional force and moment are being generated over the first section of the CMATD fuze (up to 3.77"), the additions are more than lost over the cylindrical fuze section, where a strong shock forms. A larger down force is produced over the boattail of the CMATD, resulting in a greater pitch-up moment.

3.4 Sting Effects

Modeling flow fields with sting mounted wind tunnel experiments can yield predictions with errors large enough to be important to control system design. The sting relaxes the flow transitioning from the boattail into the wake region. The base of a free flying projectile without base bleed contains a large recirculation region producing the very high drags which are characteristic of gun launched projectiles. The contraction of streamtubes over the boattail can produce unsteady aerodynamic body forces. Unsteadiness of this sort has been observed computationally in transonic calculations with highly resolved grids, as mentioned previously. More importantly, the wake structure supports the flow over the body. Representative wake modeling, in particular the modeling of vortex shedding from the body, is necessary for accurate prediction of body forces. As Figure 3-5 shows, transonic projectile flow fields are poorly modeled by wind tunnel models mounted with stings of typical diameters (3/10 of the reference diameter). The sting modelled computationally has a diameter of 1.5 inches.

The sting calculations showed excellent agreement with wind tunnel measurements over the entire range of Mach numbers, with an average disagreement of less than

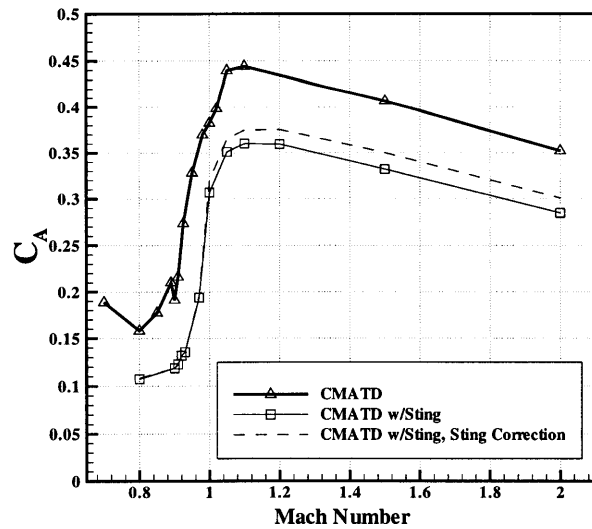
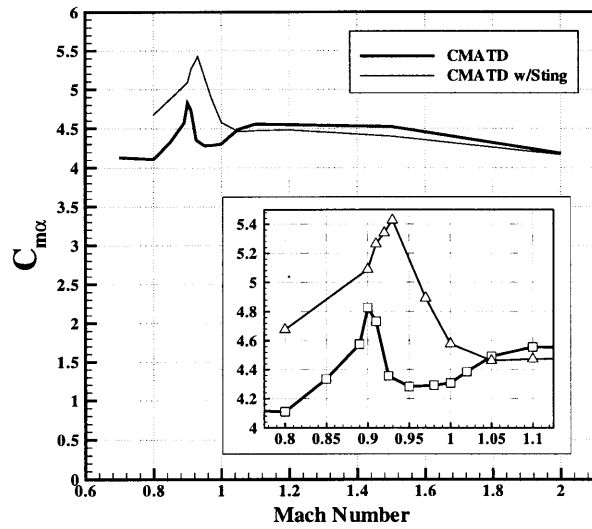
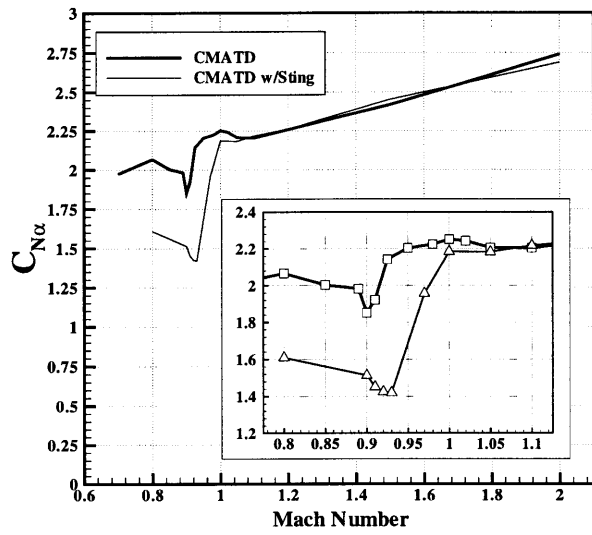


Figure 3-5: Mach Behavior of Sting Mounted Projectile

3.5%. The agreement not only serves as a validation for the computational model, but strengthens the argument that the sting introduces significant error into the wind tunnel predictions.

The sting correction plotted in Figure 3-5 has been calculated by averaging the circumferential pressure distribution at the sting-base intersection and multiplying by the cross-sectional area of the sting. For subsonic and transonic flow, the pressure in the sting-base corner is not very different from free stream, producing negligible correction. Supersonically, the correction is still only a small fraction of the difference between the free flying and sting drag predictions.

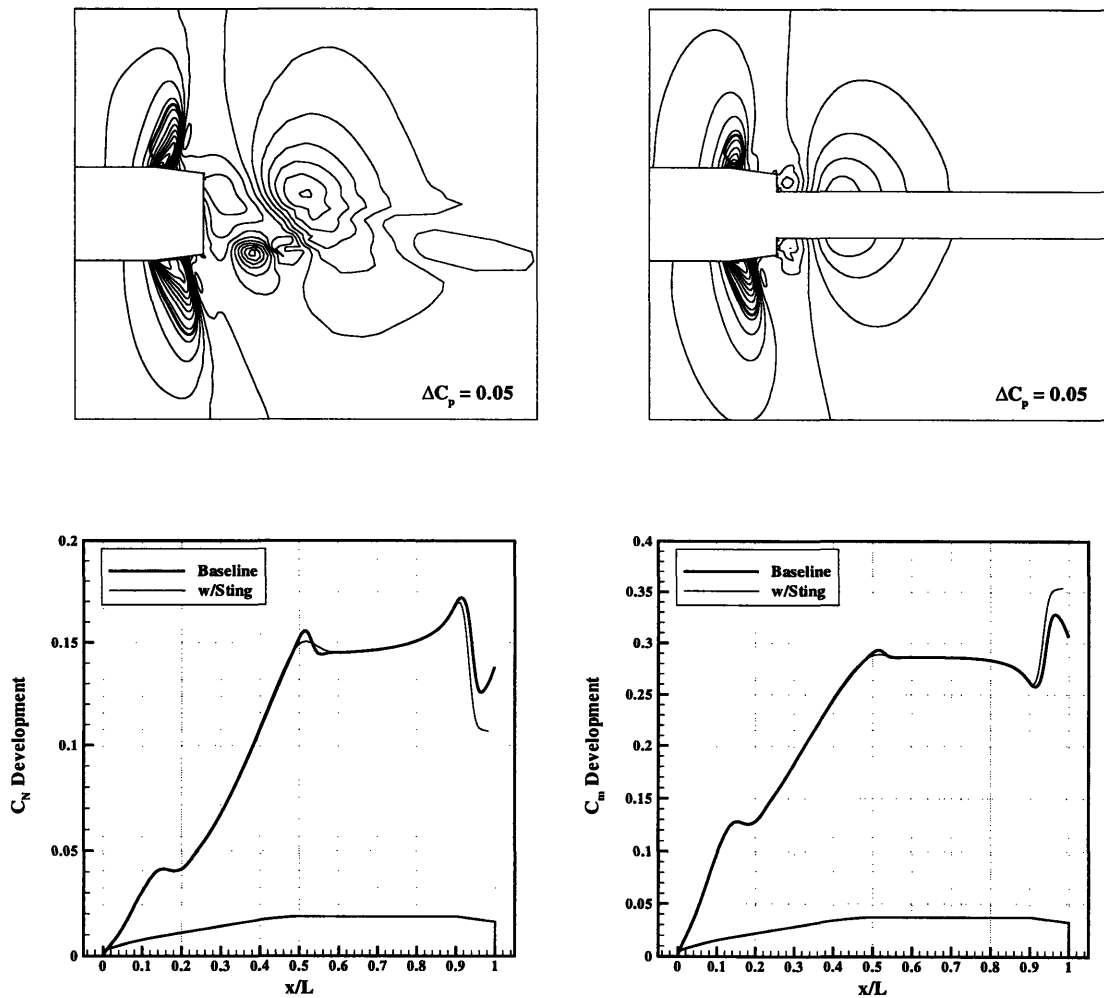


Figure 3-6: Boattail Flow Field Comparison for Free Flying and Sting Geometries at Mach 0.90 and 4° Angle of Attack

The disparity between free flying and sting geometries develops primarily over the boattail, where the sting relaxes the contraction of the stream tubes, causing the shock disk to cant farther forward, as shown in Figure 3-6. The increase in the local down force reduces the net normal force and increases the pitch moment.

3.5 Magnus Characteristics

Several Magnus calculations have been performed at Mach 1.1 and a dimensionless spin rate of $PD/2V = 0.12$. Figure 3-7 confirms that the Magnus moment is linear with spin rate at this Mach number and 4° angle of attack, as assumed in traditional projectile stability analysis.

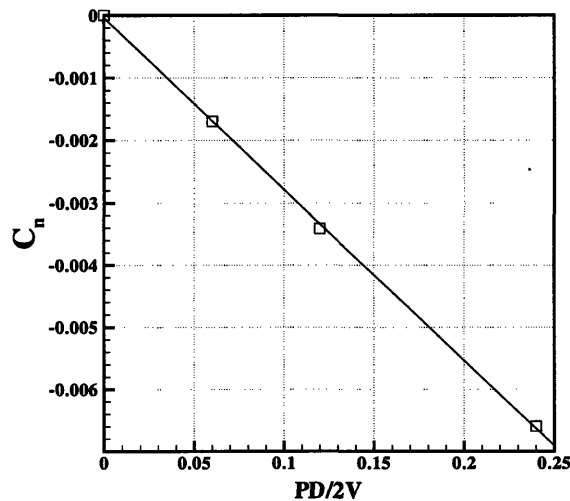
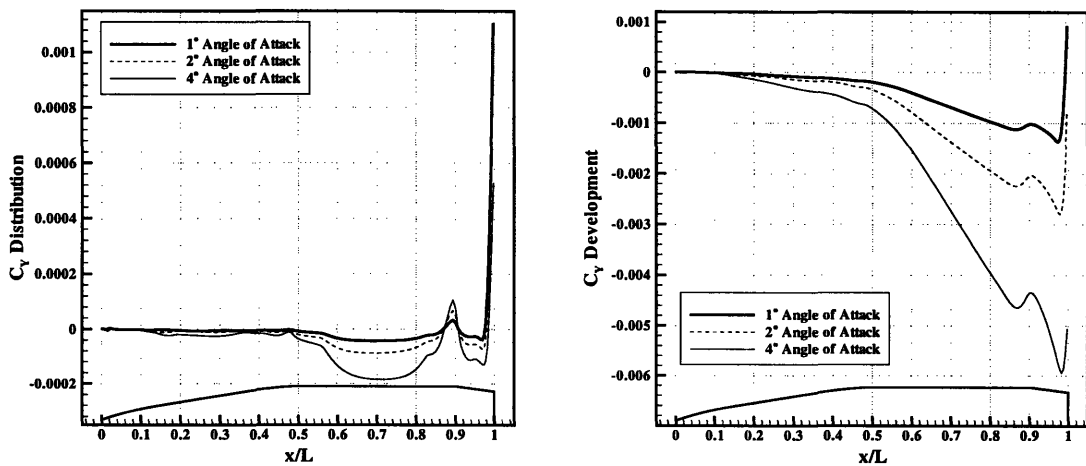


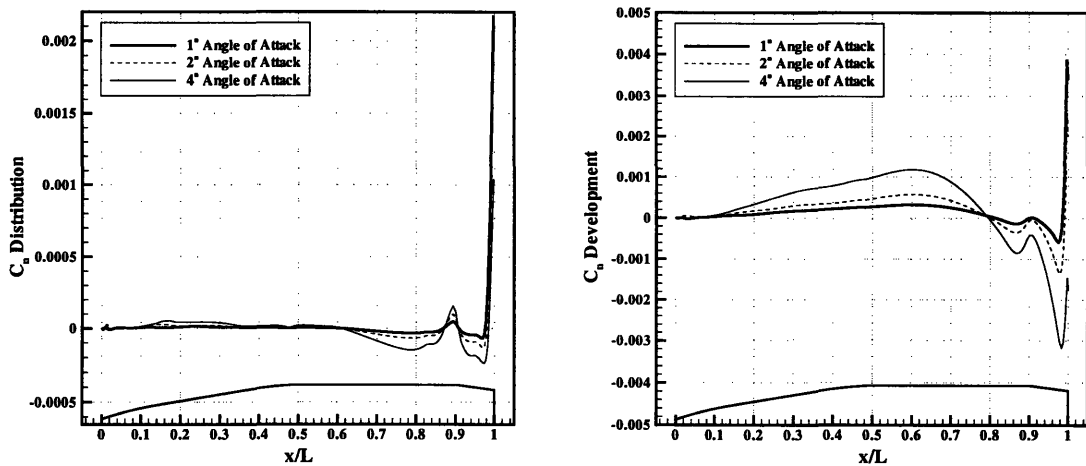
Figure 3-7: Linearity of Magnus Moment with Spin Rate at Mach 1.1 and 4° Angle of Attack

Figure 3-8 details the development of Magnus force and moment over the projectile. The clockwise from the rear (following the right hand rule) spin direction of the projectile makes the right side (from the rear) of the projectile the advancing side and the left side the retreating side. The advancing side spin velocity opposes the crossflow wind velocity, creating a higher pressure on the right side and subsequently positive side force, which can be seen clearly over the first three-quarters of the side force distribution given in Figure 3-8a.

The figure also shows that the acceleration of the flow over the cylinder-boattail junction into the boattail region and the transitioning of the flow from the boattail into the wake strongly affect the Magnus force and moment. The counteracting force is relatively strong, but still very small in magnitude with respect to the normal force. The counteracting force produced has root in the details of the boundary layer development through the adverse pressure gradient and the absorption of the boundary layer into the wake, which occurs over the last 2% of the body length.



a) Magnus Force



b) Magnus Moment

Figure 3-8: Distribution and Development of Magnus Force and Moment at Mach 1.1 for 1°, 2°, and 4° Angle of Attack and $PD/2V = 0.12$

As the angle of attack increases, the counteracting boattail force decreases, al-

though it remains influential. Despite the sign change, the curves behave similarly at the three angles of attack. The force and moment development curves show that the sign change occurs when the contribution of the majority of the body becomes greater than the counteracting force.

127

Chapter 4

Configurational Asymmetries for Lift Generation

Two configurational asymmetries are investigated for the purposes of lift generation. The two configurations have been chosen for their mechanical appeal and are represented by mechanically descriptive parameters with which constraints are easily formulated. The geometry families are referred to as the “sliced” and “bent” configurations, alluding to the generating geometric operation. As mentioned previously, the bent configuration is approximated by a shearing transformation but the term “bent” is retained for its descriptiveness. Unless stated otherwise, the standard Mk 64 geometry is used for the baseline geometry and the computations are for a static non-spinning projectiles.

4.1 Concept and Description of Geometries

Although the two configurations chosen have aerodynamic commonality, the corresponding mechanical mechanisms are quite different. The sliced configuration was conceived to allow the asymmetry to be created after launch by releasing a portion of the fuze, while the bent configuration was devised to allow active control by articulating the fuze-afterbody joint as an additional possibility to one-time asymmetry generation. The bent geometry has an advantage in that the aerodynamic asymmetry

does not reduce the internal volume. Both configurations are defined by two parameters, an incidence angle and a pivot point location. Figure 4-1 illustrates the two geometries and their defining parameters.

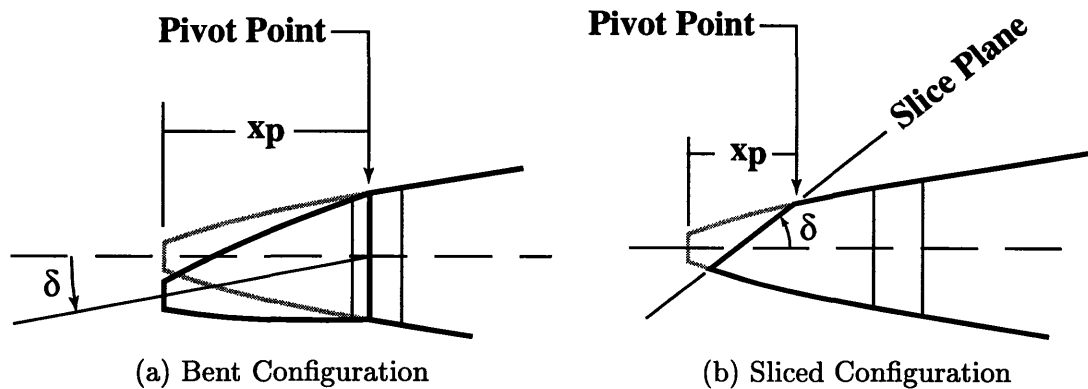
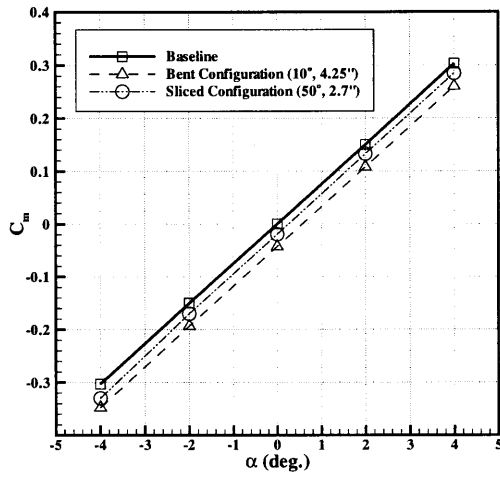


Figure 4-1: Parametric Definitions for Configurational Asymmetries

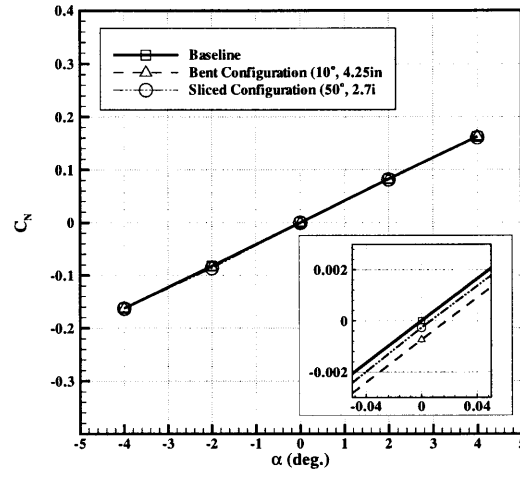
4.2 Angle of Attack and Sideslip Angle Behavior

The effect of angle of attack and sideslip angle on the pressure distribution of projectiles with configurational asymmetries determines how the aerodynamic forces and moments are described for use in dynamic models. Knowledge of nonlinear behavior severe enough to significantly modify the rigid body dynamics is necessary for control system design. Figure 4-2 gives the results of computations performed at Mach 1.1 for both configurational asymmetries as well as the baseline standard Mk 64 projectile.

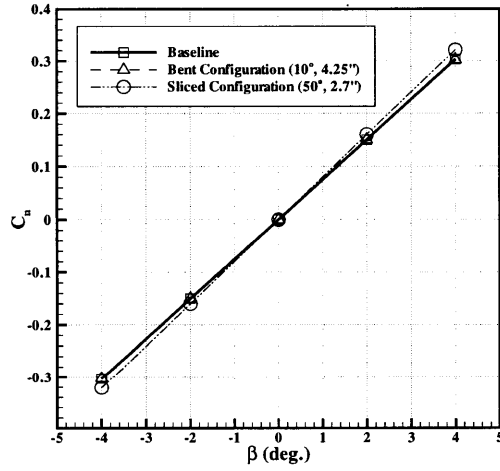
The figure shows that all configurations behave linearly with both angle of attack and sideslip angle. Figures 4-2a and 4-2b further show that the pitch moment and normal force of the asymmetric projectiles are simply offset, retaining the baseline slope with angle of attack. A zero-offset pitching moment term, C_{m_0} , and normal force term, C_{N_0} , are introduced into the linear aerodynamic stability and trajectory analysis to describe the integrated effects of the asymmetries on the pressure distributions. Furthermore, in order to reduce computational cost it is assumed that all asymmetries



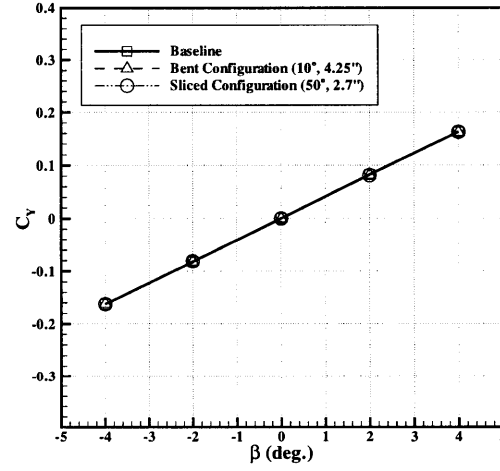
(a) C_m vs. α



(b) C_N vs. α



(c) C_n vs. β



(d) C_Y vs. β

Figure 4-2: Pitch and Yaw Linearity at Mach 1.1

retain the baseline force and moment slopes for calculation of the trim lift and for dynamic simulation.

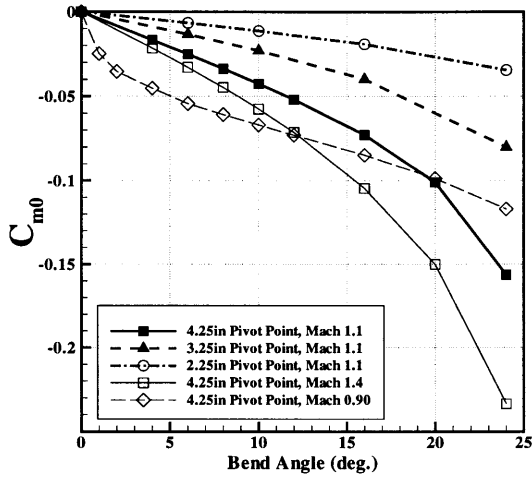
The asymmetries are symmetric about the pitch plane resulting in symmetric sideslip behavior, as can be seen in Figures 4-2c and 4-2d. The sliced configuration has a slightly modified yaw moment slope (6% greater, for the 50° slice angle at the 2.7" pivot point), a consequence of the sliced fuze redistributing the cross-sectional area and hence the normal force distribution and resulting moment.

4.3 Parametric Study

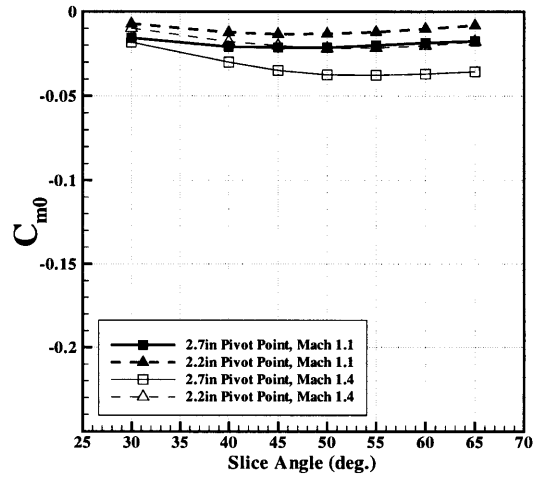
The design subspace specified by the parameterization has been searched by sweeping the feasible range of parameters until either a maximum was found or the constraints were reached. Computations were performed at zero angle of attack to obtain the zero-offset coefficients C_{N_0} and C_{m_0} , which are combined with the baseline derivatives C_{N_α} and C_{m_α} to obtain performance predictions. The variations in aerodynamic characteristics, as represented by the zero-offset coefficients are given in Figure 4-3 for the two configurations.

Inspection of the bent configuration behavior, given in Figure 4-3a and 4-3c, reveals that for supersonic Mach numbers, the force and moment coefficients increase linearly in magnitude with small bend angles, and quadratically for larger angles. The coefficients also increase in magnitude as the pivot point moves aft and as the Mach number increases. Note that the normal force coefficient produced by bending is an order of magnitude smaller than the pitch moment coefficient.

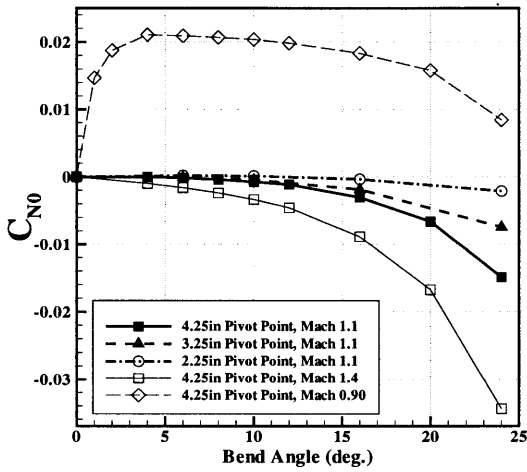
The parameter sweep at Mach 0.90 exhibits behavior completely different from the supersonic parameter sweeps. Large forces and moments are produced with very small perturbations, the smallest data point being 1° of bend. Recall from Chapter 3 that Mach 0.90 is the first critical point, the Mach number at which the shock orientation in the boattail region is very sensitive. The opposite signs of the normal force and pitch moment suggest that the normal force is being generated behind the center of gravity. Examination of pressure distributions confirms that the normal force and



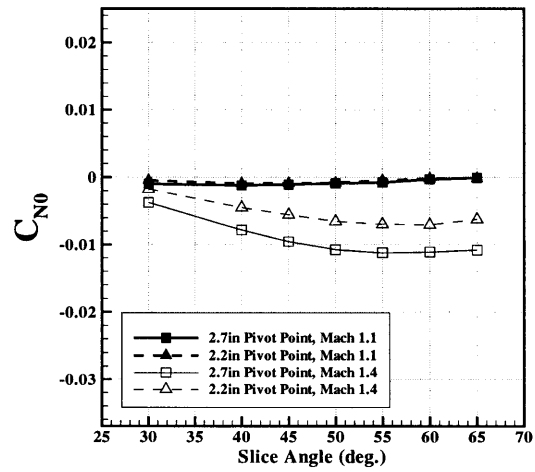
(a) C_{m0} vs. Bend Angle



(b) C_{m0} vs. Slice Angle



(c) C_{N0} vs. Bend Angle



(d) C_{N0} vs. Slice Angle

Figure 4-3: Aerodynamic Behavior with Configurational Parameter Variations

moment are being generated in the boattail.

The sliced configuration behaves differently, as can be seen in Figure 4-3b and 4-3d. The force and moment coefficients exhibit a maximum near 55° . Clearly, the amount of asymmetry generated by slicing also passes through a maximum at some point between 0° , where the slice plane does not intersect the fuze, and 90° , where the slice plane merely truncates the fuze and produces an axisymmetric body again. In fact, the volumetric asymmetry can be quantified with the second volume cross moment of inertia, I_{xz} , which is maximum at 50° . The coefficients also increase in magnitude for aft moving pivot point and increasing Mach number.

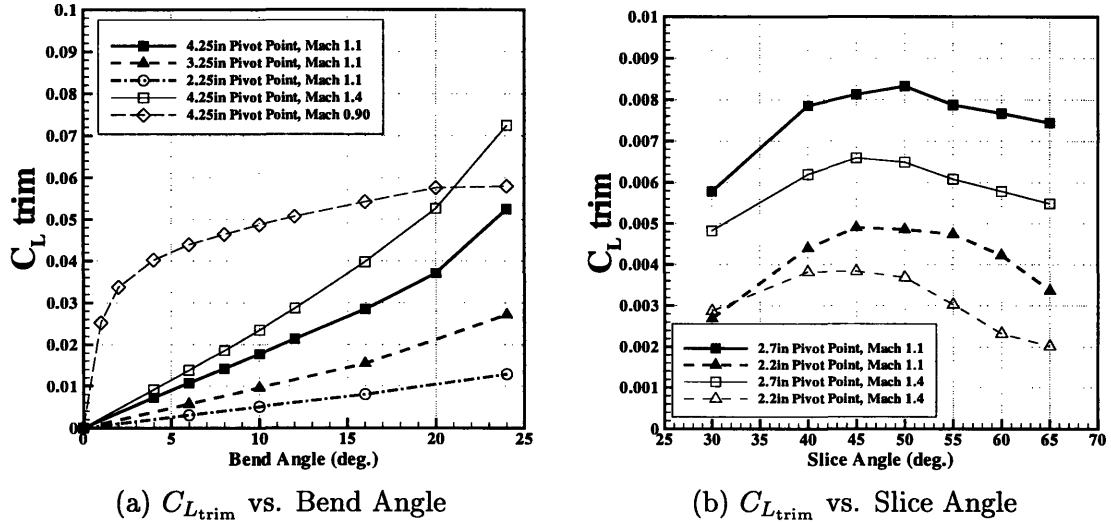


Figure 4-4: Trim State Behavior with Configurational Parameter Variations

Figure 4-4 presents the effectiveness of the configurations, as quantified by the figure of merit $C_{L_{trim}}$. The trim lift depends on the ratio of the zero-offset coefficients, not on their magnitude, which is easily seen by inserting the trim angle of attack into the trim normal force expression:

$$C_{N_{trim}} = C_{N_0} - \frac{C_{N_\alpha}}{C_{m_\alpha}} C_{m_0} \quad (4.1)$$

In particular, it is notable that zero net normal force will be generated when

$$\frac{C_{N\alpha}}{C_{m\alpha}} = \frac{C_{N0}}{C_{m0}} \quad (4.2)$$

Although the trim angle of attack will result in some trim lift due to axial force. The trim lift and normal force expressions indicate that the zero-offset normal force and moment will fight each other when they have the same sign and it is possible that large individual values will produce zero net lift.

From Figure 4-3 it can be seen that the supersonic zero-offset coefficients are all of the same sign, so that the difference between force and moment coefficients drives the performance. Thus, the bent configuration performs better than the slice, not because the zero-offset coefficients are large, but because the force and moment coefficients have an order of magnitude difference. The bent configuration benefits from nonlinear aerodynamics at Mach 0.90, producing zero-offset force and moment coefficients with large magnitudes of opposite sign, resulting in relatively large $C_{L_{trim}}$ values.

4.4 Aerodynamic Behavior

An understanding of the underlying aerodynamic behavior of the two configurations is important for evaluating the functionality of the asymmetries and for determining how best to actuate the flow field. It is of interest to determine the characteristics of the pressure field induced by the two configurations and how variations in the configurational parameters modify the pressure field.

4.4.1 Aerodynamics of the Bent Fuze

Pressure distributions over the mirror symmetry plane of the bent configuration for bend angles of 4, 10 and 16 degrees are given in Figure 4-5. The 10 degree pressure distribution is highlighted with the dark line, with the 4 degree distribution contained within it and the 15 degree distribution rising above and below it. The solid lines indicate upper surface values and the dashed lines indicate lower surface values.

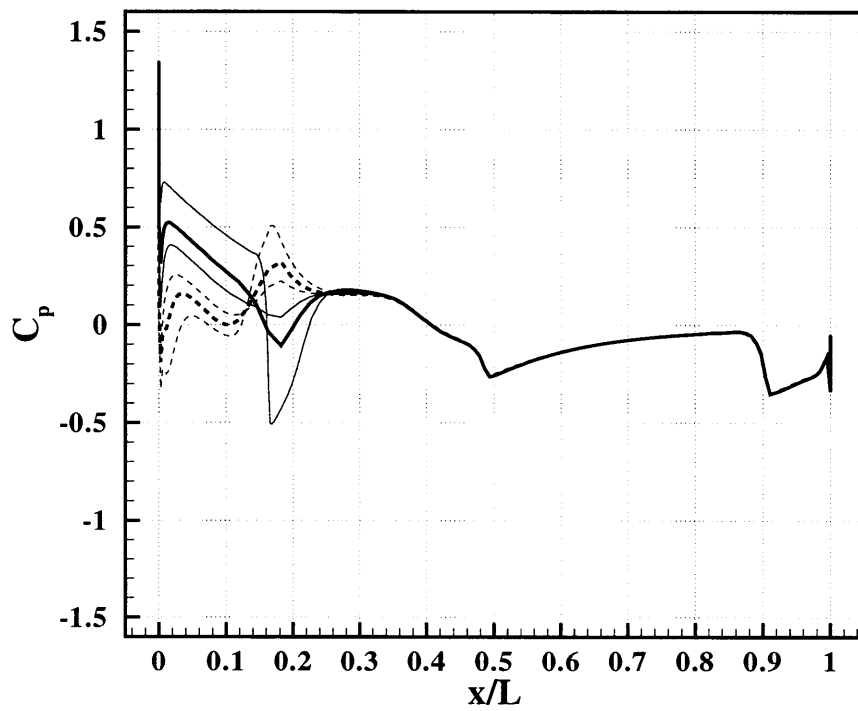


Figure 4-5: Bent Configuration C_p Distributions at Mach 1.1 for Bend Angles of 4, 10 and 16 degrees: Upper and Lower Surfaces Indicated by Solid and Broken Lines, Respectively

All of the pressure distributions produce a downward (negative normal force) over the fuze, as dictated by the larger upper surface pressure, before crossing over and producing an upward force. The two smaller bend angles crossover at the pivot point, while the largest bend angle crosses over farther aft. All three pressure distributions reunite and become non-force generating by 30% of the body length. The crossover results from the flow accelerating rapidly around the greater curvature of the upper surface asymmetry transition, producing a decrease in pressure. The flow decelerates along the lesser curvature of the lower surface, producing an increase in pressure.

Nonlinearity with Bend Angle

The pressure distributions give a clue as to the root of the nonlinear behavior of the zero-offset coefficients. The two smaller bend angles exhibit linear behavior, maintaining the same shape but having different scales. The largest bend angle displays a somewhat different shape, but only in that the upper surface pressure drop occurs slightly farther aft, bringing the crossover point with it. The aft shifted crossover point increases the down force generated over the bent portion and decreases the up force generated after the pivot point, producing a net increase in the down force generated, which accounts for the additional force generated.

The root of the nonlinearity can be found by examining the growth of the boundary layer, as visualized by its displacement thickness. Figure 4-6 shows displacement thickness profiles for the 10 and 16 degree bend angles. The boundary layer develops nearly identically on the lower surfaces of the two bend angles, while the upper surface of the 16 degree bend develops a thicker boundary layer with a more exaggerated peak over the pivot point at $x/L = 0.16$. The thicker boundary layer and exaggerated peak reduce the curvature of the outer flow and shift the point of maximum curvature and the concomitant pressure drop farther aft. Although the computations were not performed with a fine enough longitudinal mesh resolution to resolve separation around this sharp convex corner, it is very likely that a small separation bubble will form.

The nonlinearity in bend angle, therefore, results from boundary layer thickening

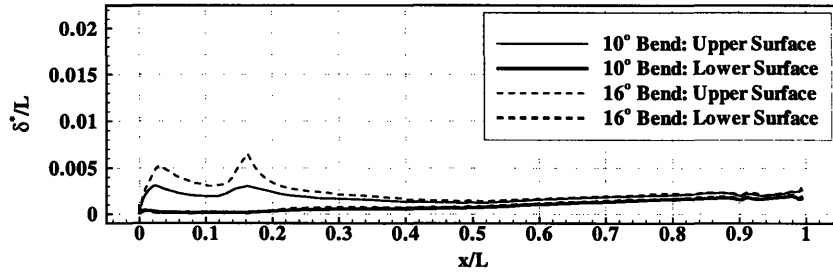


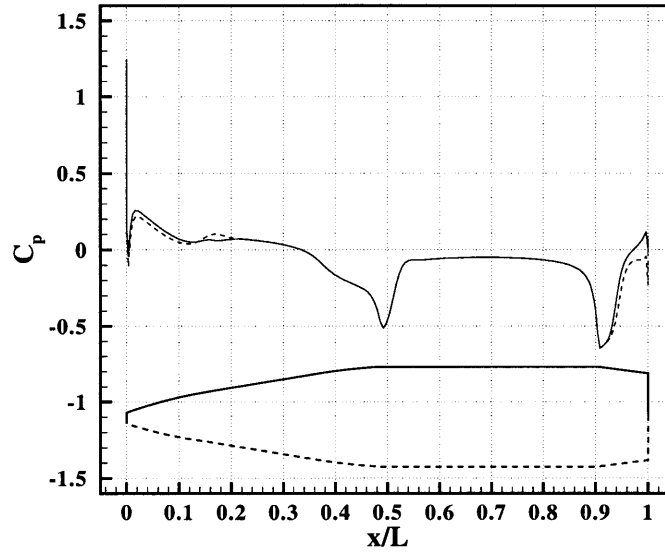
Figure 4-6: Bent Configuration Boundary Layer Behavior at Mach 1.1 for Bend Angles of 10 and 16 degrees

over the convex corner at the pivot point of the upper surface, which reduces the curvature and shifts the upper surface pressure drop aft, increasing the net normal force beyond that which would be produced by the additional local angle of attack due to the bend angle alone.

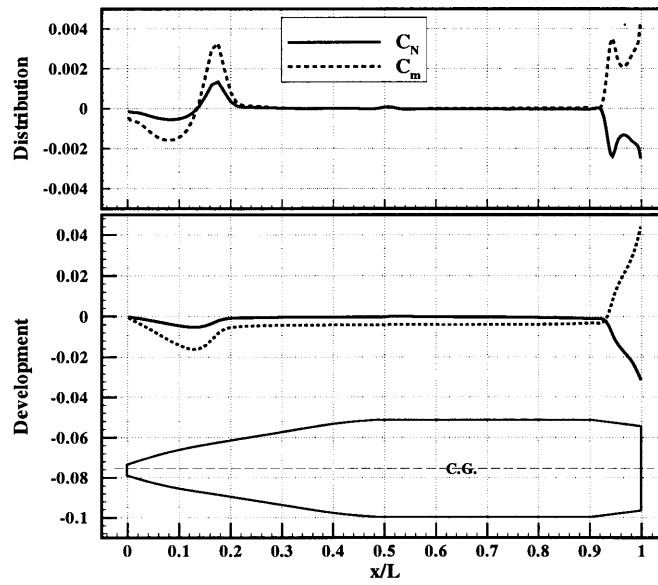
Transonic Critical Behavior

The strikingly sensitive behavior of the bend at Mach 0.90 is a consequence of the transonic critical behavior produced by the boattail, as verified by the pressure difference visible over the boattail in Figure 4-7a. The pressure distribution seems odd in that the small bend angle produces equally small pressure differences over the fuze section which do not propagate downstream into the cylindrical midsection, as for the supersonic pressure distributions of Figure 4-5, except that a large pressure difference develops seemingly without cause over the boattail. The distribution and subsequent development of the normal force and pitch moment concur that the net production occurs entirely over the boattail, as shown in Figure 4-7b.

The essentially axisymmetric pressure distribution over the mid-section indicates that the slight bend in the fuze does not significantly modify the inviscid outer flow, suggesting that the inviscid outer flow does not communicate the small perturbation of the fuze to the boattail. Examination of the boundary layer displacement thickness distribution in Figure 4-8 reveals that a slightly thicker boundary layer on the lower boattail surface relaxes the pressure recovery over that surface, locating the lower shock farther aft. The consequential differential shock locations between upper and



(a) Pressure Distribution



(b) Normal Force and Pitch Moment Development

Figure 4-7: Transonic Critical Behavior of a 1° Bend Angle at Mach 0.90 and Zero Angle of Attack

lower surfaces produces a locally negative normal force and positive pitch moment due to the force being located aft of the center of gravity.

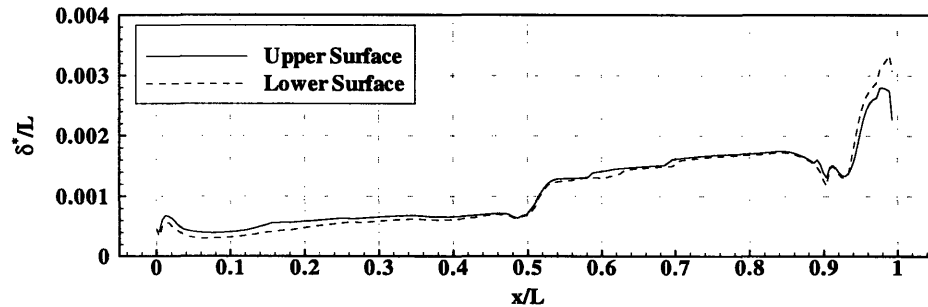


Figure 4-8: Boundary Layer Growth over 1° Bend Angle at Mach 0.90 and Zero Angle of Attack

The thicker lower surface boundary layer results from momentum loss over the lower surface of the fuze section, which does not effect the displacement thickness significantly until exacerbated by the adverse pressure gradient over the boattail. The adverse pressure gradient over the boattail can amplify small perturbations in the boundary layer into large net forces, giving viscous flow and the transonic critical behavior of boattail projectiles an important influence on aerodynamic fuze design.

4.4.2 Aerodynamics of the Sliced Fuze

Figure 4-9 shows how the fuze pressure pressure distributions vary with slice angle at Mach 1.4, with the dashed line denoting the lower surface pressure. The aft portions of the pressure distributions are identical and non-lifting and have been omitted. The flow over the upper surface expands very rapidly over the edge of the slice plane, but a shock compresses the flow, quickly reuniting it with axisymmetric flow.

As the slice angle increases to the critical angle of 55°, the angle generating the maximum normal force, the pressure on the slice plane increases as the upper surface pressure just aft of the slice plane and the lower surface pressure below the slice plane decrease. The net effect is an increase in normal force as the slice angle increases to the critical angle. The shape of the pressure distribution becomes fully developed and generates the maximum normal force at the critical angle. As the slice angle

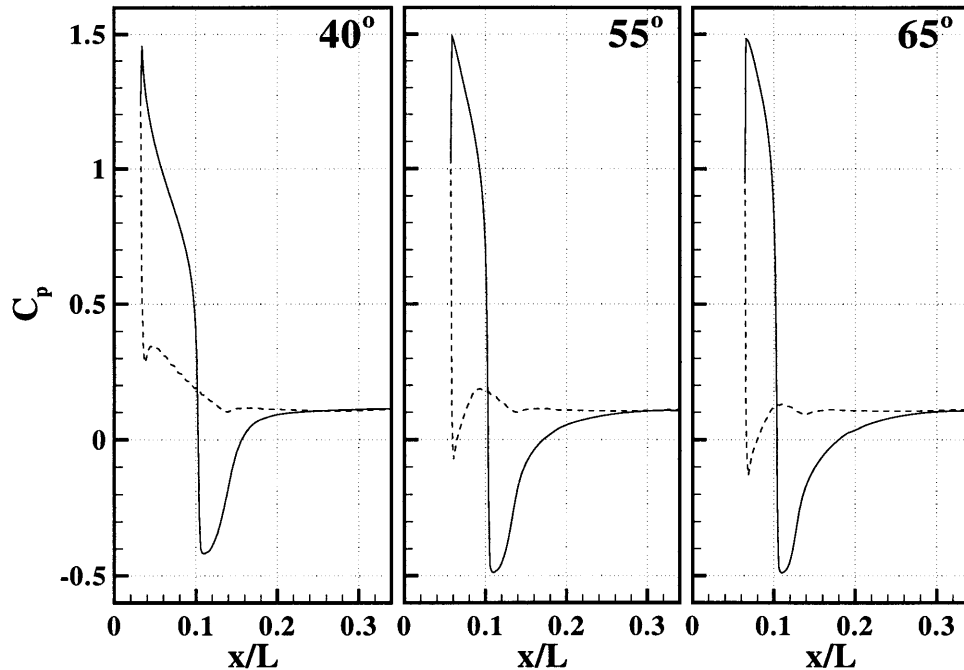
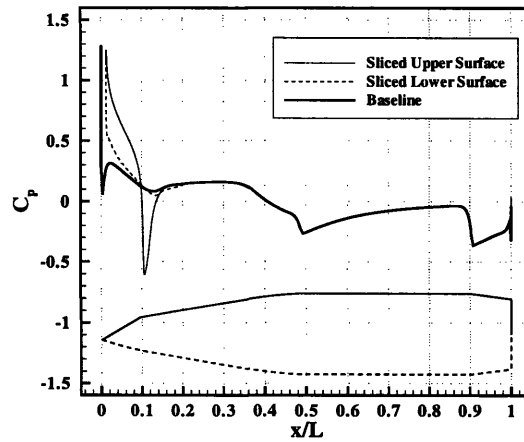


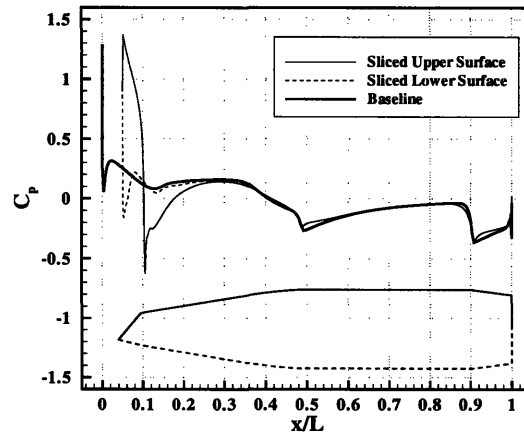
Figure 4-9: Sliced Fuze Pressure Distributions at Mach 1.4: Upper and Lower Surfaces Indicated by Solid and Broken Lines, Respectively

exceeds the critical angle, the pressure distribution maintains form while becoming compressed by the reduction of the planform area of the slice plane, and thus the normal force decreases, accounting for the maximum. The introduction of the slice plane sought to create a high pressure area for normal force production, but note that acceleration of the flow from the stagnation point, around the tip to the lower surface also plays an influential role in the production of net normal force.

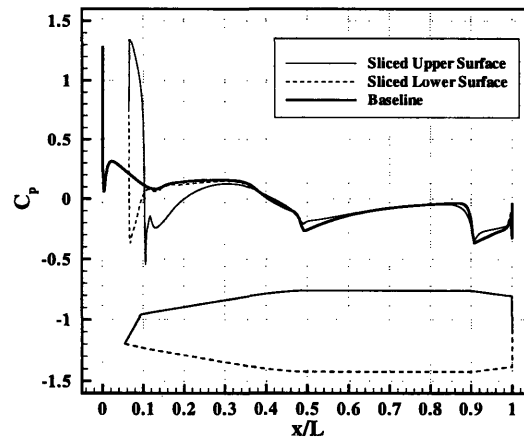
At Mach 1.1, the pressure distributions have somewhat different features due to separation, as shown in Figure 4-10. The upper surface pressure distribution of the 30° slice angle at Mach 1.1 has the same form and similar magnitude as exhibited by all slice angles at Mach 1.4, while the upper surface pressure distributions of the larger Mach 1.1 slice angles have a different form of recovery from the expansion around the edge of the slice plane. Examination of the flow field reveals that the flow separates across the slice edge, which produces the initially rapid compression but delayed recovery as seen in Figures 4-10b and 4-10c. Figure 4-11 gives the displacement thickness of the boundary layer for two slice angles at Mach 1.1, showing the massive



(a) 30° Slice at 2.7"



(b) 50° Slice at 2.7"



(c) 65° Slice at 2.7"

Figure 4-10: Sliced Configuration Pressure Distributions at Mach 1.1

boundary layer growth induced by the slice.

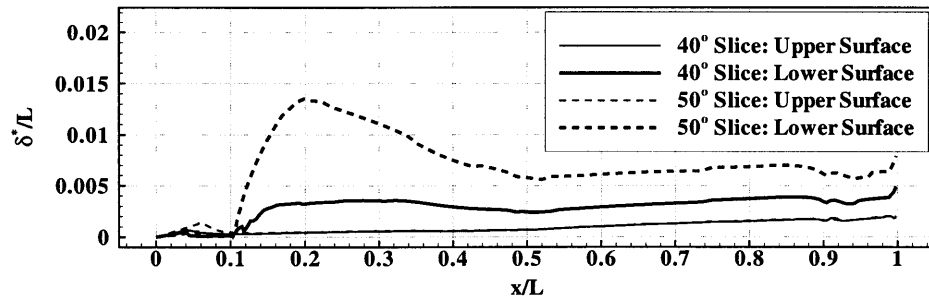


Figure 4-11: Boundary Layer Behavior for Two Slice Angles at Mach 1.1

The large separated region not only delays the recovery, producing a larger positive normal force, but the effects of the separation on the boundary layer persist downstream with an upper surface pressure distribution which does not return to the axisymmetric distribution, as can be seen in Figure 4-12. The development of the normal force and pitch moment curves divulge that much of the net force and moment production occurs in the boattail region, where the thicker upper boundary layer influences the shape of the pressure recovery.

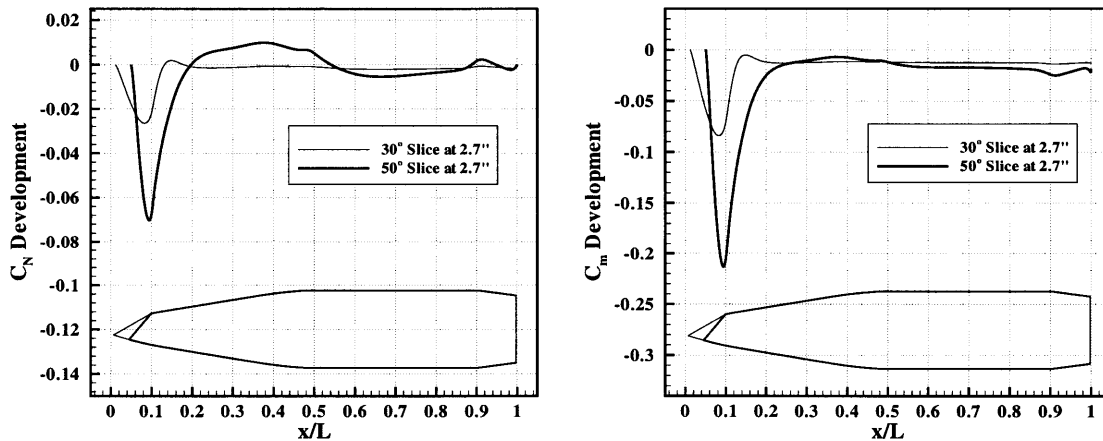


Figure 4-12: Normal Force and Pitch Moment Development at Mach 1.1

As stated previously, the parameters chosen for the sliced configuration do not relate to the resulting volumetric asymmetry linearly, as do the parameters chosen for the bent configuration, but in fact, the maximum volumetric asymmetry occurs for

a slice angle of 50° . Investigation of how the slice modifies the pressure distribution found that four factors influence the performance of the slice configuration. First, the planform area of the slice plane governs how much force the engendered pressure difference produces. Second, the cross-sectional projected area of the slice plane relates to the pressure magnitude. Third, the geometry of the leading edge, that is, the corner between the slice plane and the lower surface, drives the low pressure zone on the lower surface. Fourth, the transition from the high pressure on the slice plane to the axisymmetric afterbody pressure distribution governs the recovery loss, which was found to be invariant with slice angle at higher Mach numbers.

The competition between the first two factors can be quantified as the product of the cross-sectional projected area and the planform area of the slice plane, $\sin(\delta) \cos(\delta)$, which correctly predicts the slice angle for maximum $C_{L_{\text{trim}}}$, but not the component coefficients. The slice angle can be included in the above product to account for the leading edge corner angle, quantifying first three factors with the product $\delta \sin(\delta) \cos(\delta)$ nearly linearizes the slice angle variation of the Mach 1.4 normal force data, but does not quite predict the angle of the maximum moment, possibly due to the lack of information on the change in moment arm.

4.4.3 Aerodynamics of Normal Force Generation

In potential theory, the change in cross-sectional area of an *arbitrary* slender body at angle of attack produces the change in momentum responsible for normal force generation in both subsonic and supersonic flows. Slender body theory assumes a pointed, zero cross-sectional area tip, thus ideal slender body analysis relates the crossflow in the base plane directly to the normal force[1].

Computations show that the net normal force is no longer commensurate with the angle of attack and change in cross-sectional area in the presence of viscous and other non-potential phenomena. In particular, the impingement of shocks on the surface and regions of separation significantly modified this behavior. This should not be a surprise, however, because shock waves and separation modify the vorticity of the flow field, affecting the net circulation. Additionally, the circulation introduced by a

lifting system modifies the flow field with an induced velocity component, like the down wash produced by a wing.

The bent configuration affords a particularly good example of the effects of induced velocity. Examination of the normal force distribution at high Mach numbers, where linear supersonic behavior should dominate, reveals that the free stream aligned axisymmetric afterbody is responsible for the loss of normal force generated by the bent fuze. The generation of a counteracting normal force over the afterbody must result from local flow inclination, in fact, the lifting bent fuze must produce a local induced angle of attack. In the framework of potential theory, a camber line can be defined as the locus of the cross-sectional centroids. As in thin airfoil theory, the camber line is required to be a streamline of the outer flow, away from the surface, which makes the induced velocity a function of the slope of the camber line.

In the spirit of thin airfoil theory, the chord of the projectile is defined as the line connecting the centroid of the tip to the centroid of the base. For the bent configuration and approximately for the sliced configuration, the camber line becomes two linear segments joined at the centroid of the cross-section corresponding to the pivot point. The fuze angle is defined as the angle between the chord and the linear camber line component of the fuze. Similarly, the base angle is defined as the angle between the chord and the baseline axis of revolution. A zeroth order correction is then made by correcting the free stream angle of attack by the camber line inclination, which is the base angle. This reduces the local angle of attack of the bent fuze and creates a local angle of attack for the afterbody. Normal force development can be predicted by application of slender body theory with the corrected local flow inclinations.

Figure 4-13 compares this Mach independent prediction with computations at two Mach numbers. The development of normal force at Mach 2.5 seems to confirm the induced velocity hypothesis with strong quantitative agreement in the fuze section, and qualitative agreement in the afterbody. Indeed, the maximum is well predicted in both location and magnitude. Notice that the normal force development over the afterbody is inversely proportional to the distance, as expected for induced velocity

phenomena.

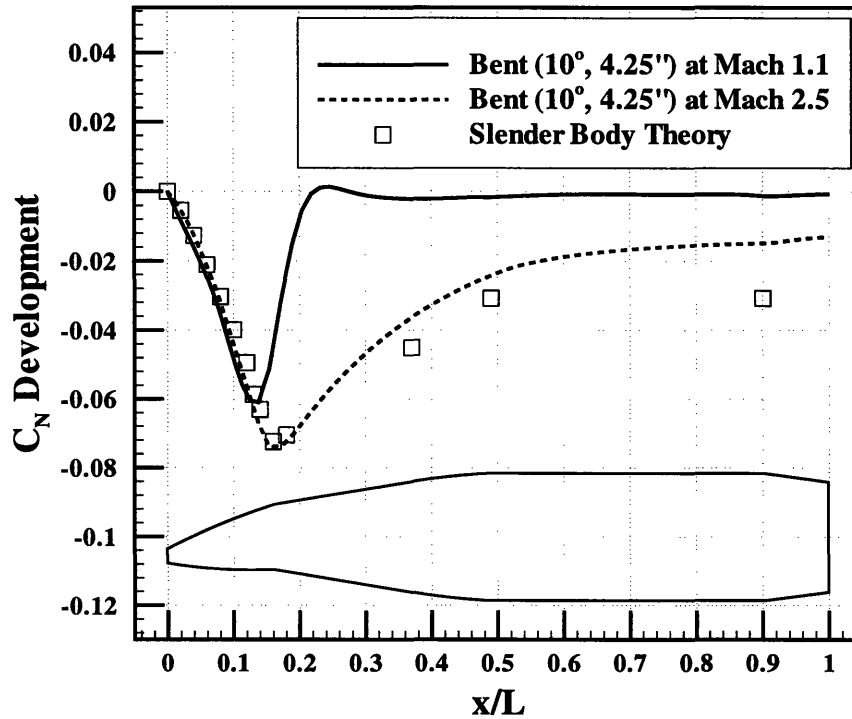


Figure 4-13: Comparison of Slender Body Theory and Computation at Mach 1.1 and Mach 2.5

The normal force development at Mach 1.1 does not seem to behave in the same manner. Although the build-up of normal force over the fuze section shows agreement with the analysis, the computation never realizes the predicted maximum and yields entirely different behavior over the afterbody. Lower supersonic flows support more rapid recovery from the acceleration of the flow around the upper surface of the bend, through the formation of a shock. Pressure distributions indicate that the pressure distribution over the lower surface changes very little, while the upper surface pressure recovery lengthens with increasing Mach number.

Both configurations share the perturbing characteristic that the fuze generates a very large normal force only for it to be lost over the pivot point and the afterbody, as can be seen in Figure 4-14. Unfortunately, the loss of lift is a consequence of the lift generation itself; due to the concomitant induced angle of attack and low pressure produced while transitioning from the high pressure region to the axisymmetric afterbody. The net normal force produced by both configurations results more from

indirect small scale residual disturbances, than from the direct action intended by the asymmetries. This is evident in the greater net normal force generated by the bent configuration, despite the fact that the sliced fuze develops a larger normal force than the bent fuze.

The larger normal force developed over the 50° sliced fuze is in part due to the greater change in cross-sectional area of the sliced fuze, but also suggests that the local angle of attack is similar to that of the 10° bend shown. The larger normal force and pitch moment generated by the bent configuration result not from the effectiveness of the fuze itself, but because the sliced configuration, in comparison, is relatively poor at maintaining force and moment developed by the fuze.

4.5 Mach Behavior

The 50° sliced configuration and the 10° bent configuration, both at their aft pivot point constraint, have been chosen as the representative candidates for the two configurations. The 50° slice has been chosen because it produces close to the maximum $C_{L_{trim}}$, while the 10° bend has been chosen because it has a reasonable mass asymmetry and it performed satisfactorily. Figure 4-15 gives the behavior of the zero-offset coefficients over a range of Mach numbers.

For both configurations, C_{m_0} and C_{N_0} exhibit fluctuating behavior in the transonic region, transitioning to monotonic increasing magnitude supersonic behavior. As discussed previously, transonic critical phenomena driven by boattail sensitivity produce the peaks and dips. In particular, the sliced configuration thickens the upper surface boundary layer, while the bent configuration thickens the lower surface boundary layer, thus the boattail shock disk cants opposite directions, increasing the magnitude of the bent configuration pitch moment and decreasing the magnitude of the sliced configuration pitch moment. Similarly, the normal force generated by the bent configuration increases in magnitude, while it decreases in magnitude for the sliced configuration.

The normal force of both configurations passes through zero near Mach 1.0, as

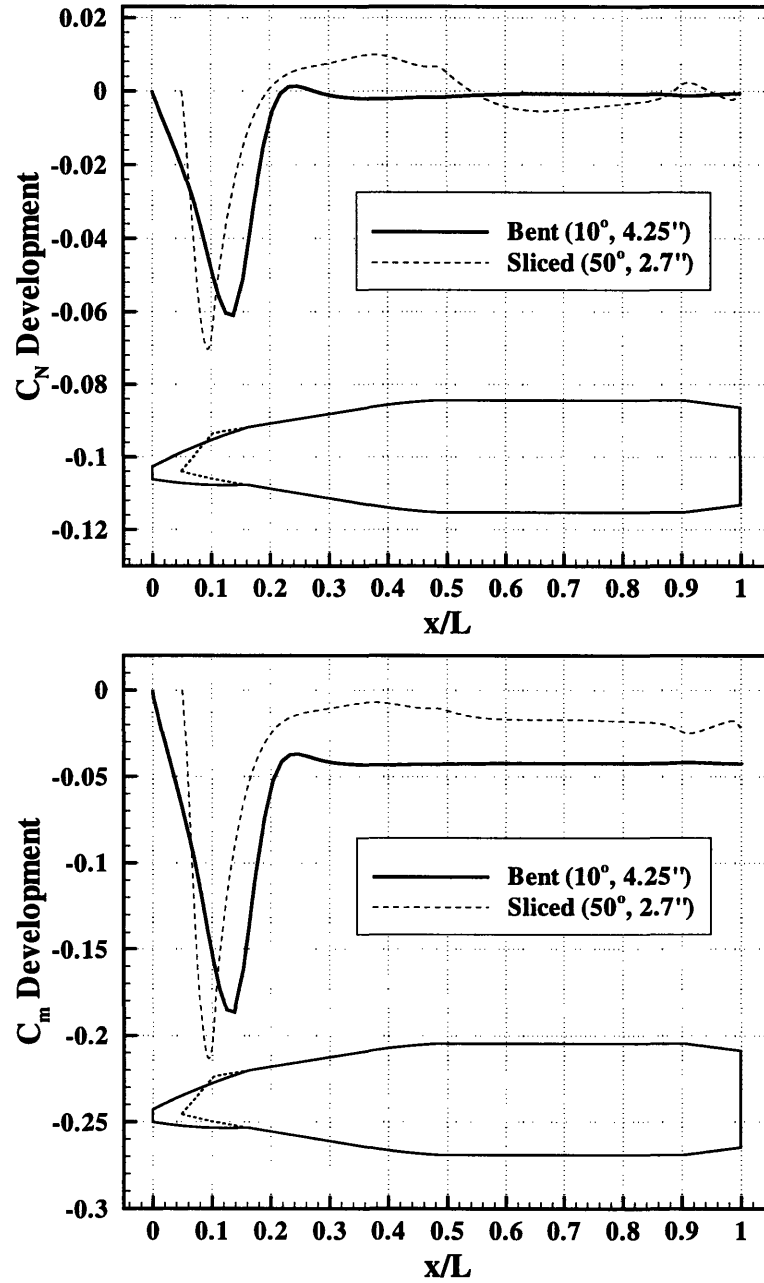
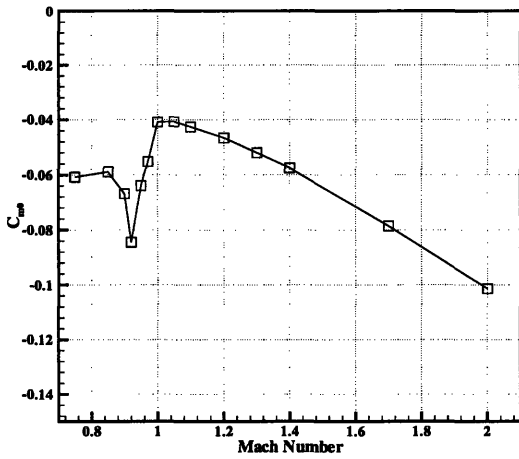
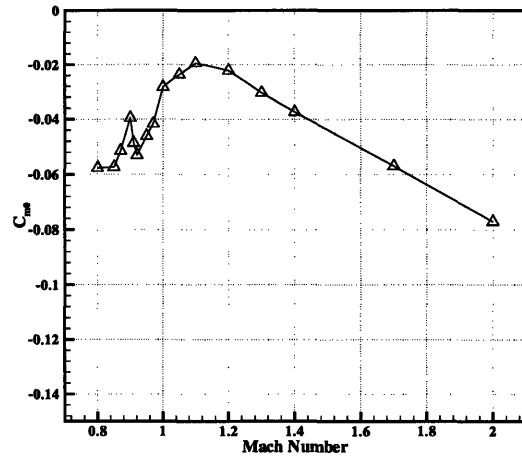


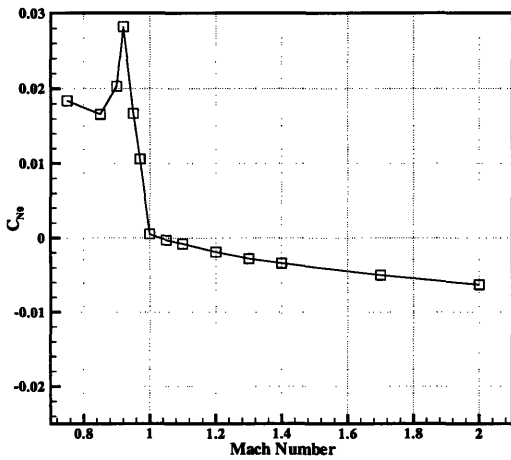
Figure 4-14: Force and Moment Development Comparison of Sliced and Bent Configurations at Mach 1.1



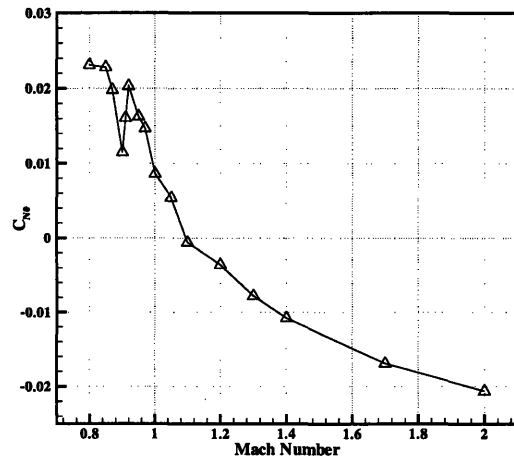
(a) C_{m0} vs. Mach for Bent Fuze



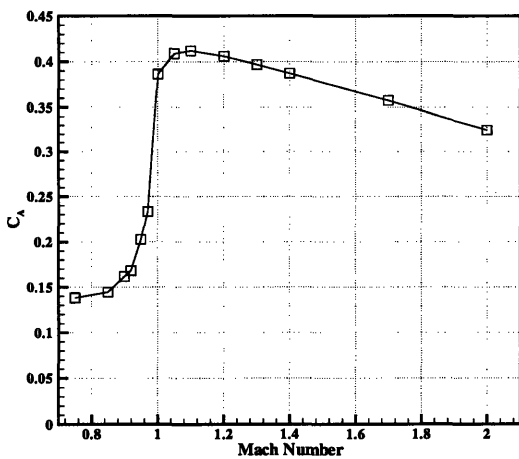
(b) C_{m0} vs. Mach for Sliced Fuze



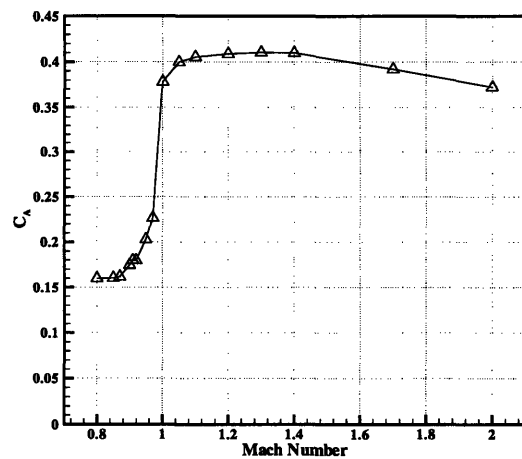
(c) C_{N0} vs. Mach for Bent Fuze



(d) C_{N0} vs. Mach for Sliced Fuze



(e) C_A vs. Mach for Bent Fuze



(f) C_A vs. Mach for Sliced Fuze

Figure 4-15: Aerodynamic Variation with Mach number for 10° Bend at 4.25" and 50° Slice at 2.7"

the net force generation transitions from being boattail driven to being driven more directly by the asymmetric fuze. The pressure recovery from the acceleration of the flow from the high pressure upper surface to the lower pressure axisymmetric afterbody drives the behavior in the supersonic region. Increasing Mach number tends to increase the pressure coefficient on the ogive, decreasing the acceleration required of the flow which not only reduces the magnitude of the counteracting force generated over the transition, but lengthens the recovery. The longer recovery ameliorates the generation of moment by shortening the moment arm of the counteracting normal force.

The bent configuration has classical projectile axial force characteristics, while the sharp transition of the sliced configuration separates the flow and produces a strong shock at or just aft of the geometric discontinuity, even at the higher Mach numbers where the bent fuze no longer exhibits strong shocks.

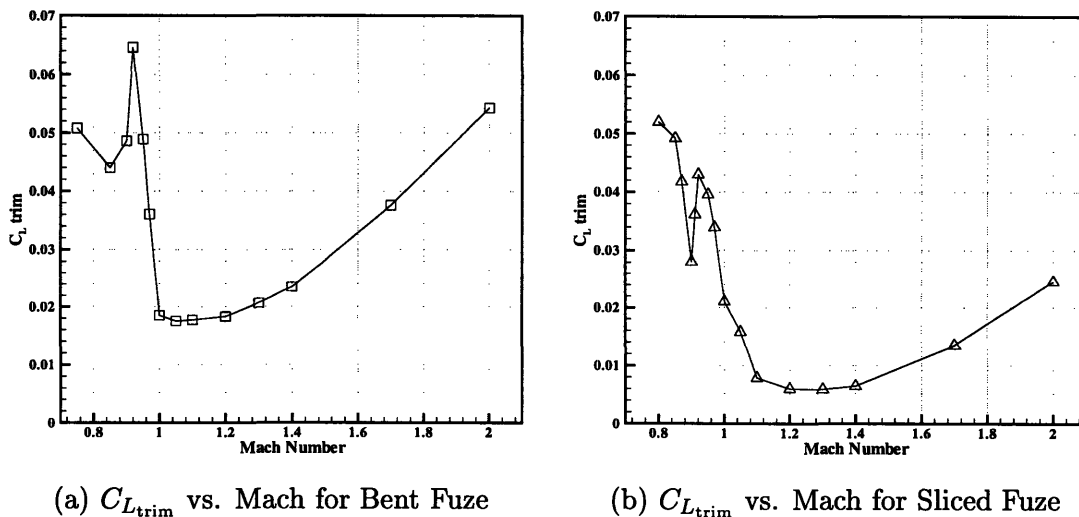


Figure 4-16: Trim State Variation with Mach number for 10° Bend at 4.25” and 50° Slice at 2.7”

Figure 4-16 shows the variation of the trim lift of the two configurations over the Mach range. The trim lift curves carry the form of the zero-offset normal force curves. Both configurations have a minimum trim lift near Mach 1.0, where the lifting mechanism transitions from boattail to fuze driven.

4.6 Magnus Characteristics

Although a thorough validation of the Magnus modeling and predictions has not been carried out, several computations have been performed for a despun fuze and a dimensionless afterbody spin rate of $PD/2V = 0.12$ at Mach 1.1 to investigate the possible effects of aerodynamic actuation on Magnus. The Magnus force and moment increase in magnitude (but negative in sign) for increasing bend angle and sliced plane pivot point location, as shown in Figure 4-17.

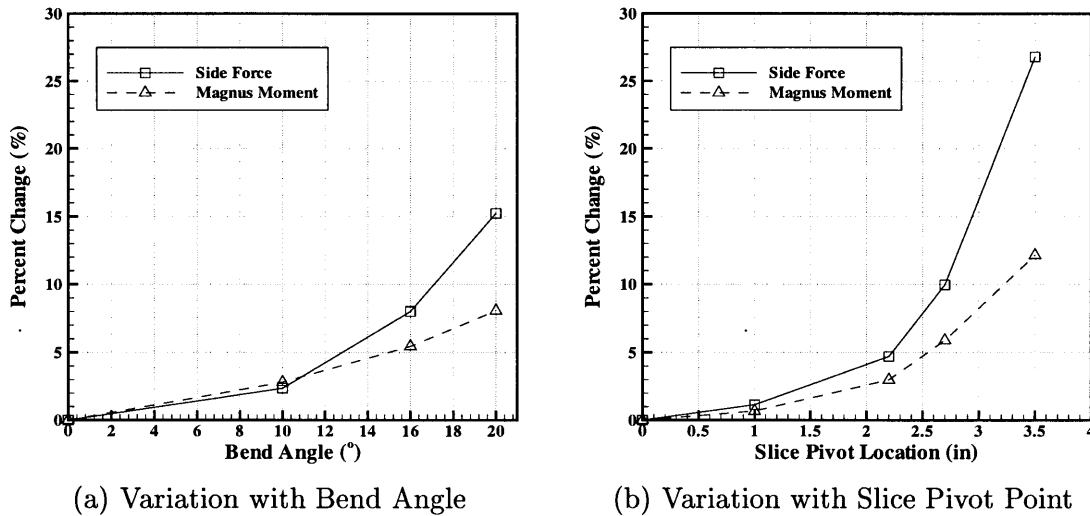
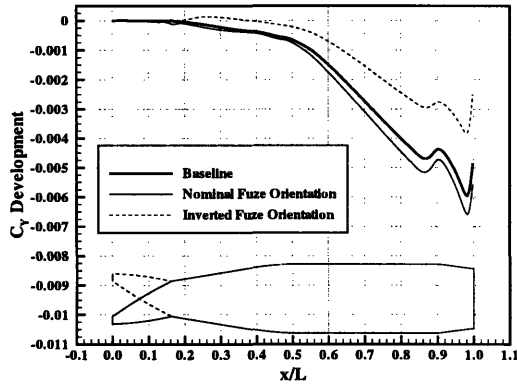


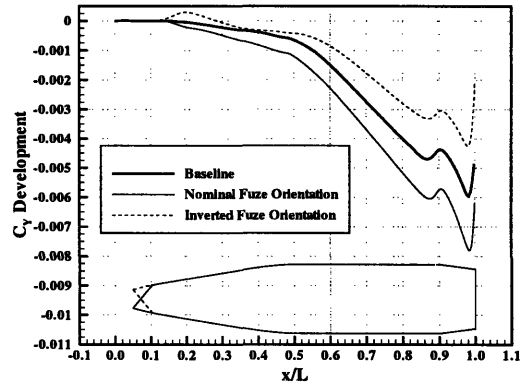
Figure 4-17: Effects of Parameter Variations on Magnus for Bend at 4.25'' and 50° Slice

Figure 4-18 gives the development of Magnus force and moment over representative configurational asymmetries as well as for the baseline Mk 64. The computations were performed for a dimensionless spin rate of 0.12 at Mach 1.1 and opposing fuze orientations. The configurational asymmetries will introduce a fuze roll angle dependency on the Magnus force and moment, as implied by the rather large difference between fuze orientations. The precessional dynamics will be modified by a Magnus moment which depends not only on the spin rate and angle of attack (to second order), but also on the roll angle of the fuze.

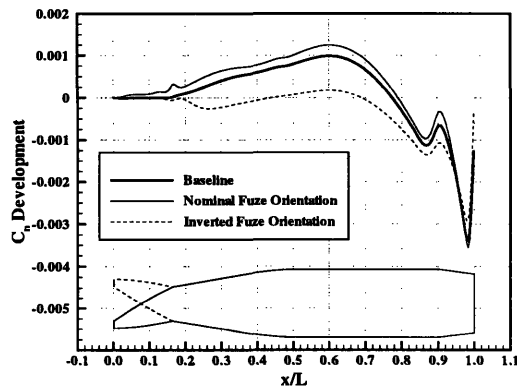
The nominal fuze orientation produces greater Magnus effects because both nom-



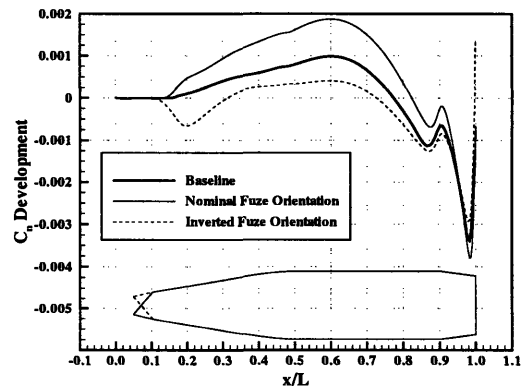
(a) Bent C_Y Development



(b) Sliced C_Y Development



(c) Bent C_n Development



(d) Sliced C_n Development

Figure 4-18: Development of Magnus Force and Moment over Configurational Asymmetries at Mach 1.1 and $PD/2V = 0.12$: 20° , 4.25" Bent Configuration and 50° , 2.7" Sliced Configuration

inal orientations develop thicker upper surface boundary layers for non-spinning projectiles than the corresponding inverted orientations. For spinning projectiles, the influence of the fuze on the upper surface boundary layer propagates circumferentially in the direction of the spin to affect the boundary layer behavior on the advancing side. The interaction thickens the boundary layer on the advancing side, increasing the magnitude of the Magnus force and moment.

The inverted orientation behaves similarly, only the thicker lower surface boundary layer interacts with the retreating side, the side for which spin usually decreases the boundary layer thickness. The change in Magnus effect produced by the inverted orientation of the fuze exceeds that produced by the nominal orientation, indicating that inverted orientation more significantly modifies the lateral difference in boundary layer thickness.

As for the baseline projectile, the boattail of the configurational asymmetries contributes significantly to the net Magnus force and moment, but the asymmetric fuzes do not change the nature of Magnus development, nor do the asymmetries trigger Magnus sensitivities to boundary layer development, as evinced by the consistent shape of the curves. The inverted orientation of the sliced fuze does exhibit a sign change in Magnus moment which, while a possibly devastating stability and control issue, results merely from the reduction in forebody contribution allowing the boattail to dominate.

4.7 Design Considerations

Parameter sweeps indicate that the bent fuze has much more potential for trim lift generation. Although the performance of the 50° , 2.7" sliced fuze, as represented by the trim lift behavior of Figure 4-16b, does not seem horribly poor in comparison to the 10° bent fuze, the loss of performance in the transonic region coupled with the transonic sensitivity of the trajectory results in very poor performance, as shown in Figure 4-19.

The basis of comparison is one of reasonableness. That is, the sliced configuration

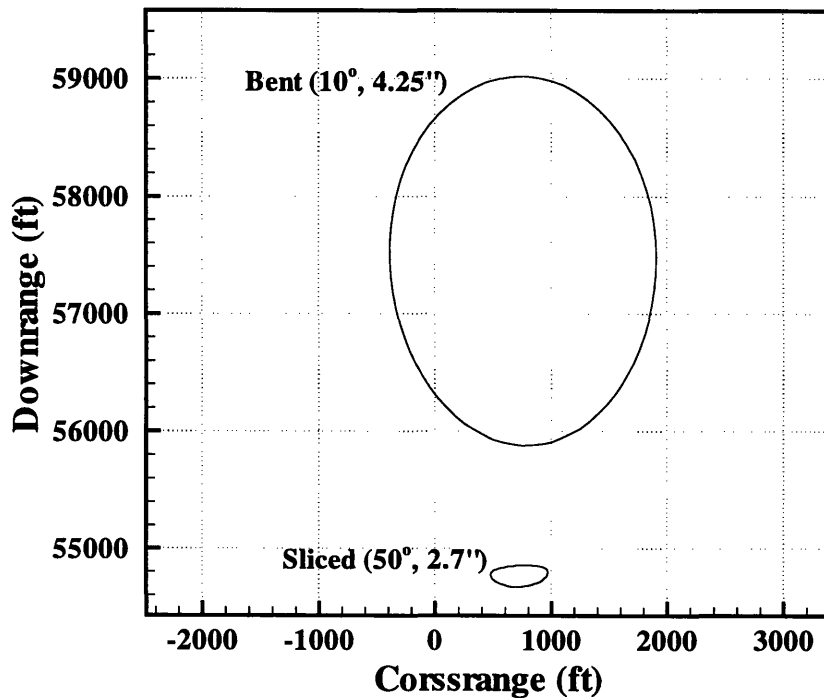


Figure 4-19: Maneuvering Envelopes of Representative Configurational Asymmetries for a 10 second Delay in Control Initiation

chosen generates the maximum trim lift at Mach 1.1 for the sliced parameters and constraints, and the bent configuration was chosen because the bend seemed reasonable and was within the constraints. Of course, one would wish to minimize the bend angle to meet trajectory control force requirements in application. Clearly, the bent fuze has the advantage that it can be pivoted farther aft, at the fuze-ogive junction, without violating the design constraints. The bent fuze gains this advantage because the bending transformation does not interfere with the fuze volume.

The bent configuration has three very positive design attributes which the sliced fuze does not share. First, the bending transformation does not incur a loss of internal volume. Second, the bent fuze provides sufficient trajectory control with predicted crossrange envelope of 1,150 feet. Third, the bent fuze produces smaller changes in the Magnus force and moment and does not produce a sign change in either for even a substantial 20° bend.

The bent fuze does, however, create a larger mass asymmetry, perhaps requiring more attention to dynamic stability than might be required for the sliced fuze. One

issue regarding the fixed-trim strategy revolves around what to do with the trim lift before navigation begins, requiring on the order of 10 seconds. The sliced fuze can be launched symmetrically with a fill-in piece that is later released when navigation begins. The bent fuze most likely requires an internal mechanism or joint to allow for a symmetric configuration, although there is the possibility that a releasable shroud could be attached to the upper surface such that there is no asymmetry across the horizontal plane.

The design of a control system for either of the configurational asymmetries requires more information than the present computations provide. In addition to the static pitch moment and normal force coefficients, Magnus moment and force as well as roll and pitch moment damping coefficients are required throughout the Mach range.

1000

1000

Chapter 5

Leveraging Sensitivities for Lift Generation

The previous chapter considered several design concepts which attempted to modify the local pressure distribution, but it was found that the local gains were lost downstream during the aerodynamic recovery from the local actuation. Investigation also revealed that the sensitive boattail flow was primarily responsible for net force and moment generation in the transonic regime. The present chapter investigates a novel concept which attempts to leverage the transonic critical sensitivity for actuation purposes. Clearly, targeting transonic sensitivity limits the range of Mach numbers for effective control, but the initial trajectory sensitivity studies presented in Chapter 1 suggested that the maneuvering envelope also has transonic sensitivity which could provide synergy.

5.1 Concept and Description of Geometry

Previous investigation showed how the boundary layer served as a communications channel between the fuze and the boattail, with very little effect in between. While the present realization of the leveraged actuation concept lacks the subtle control possibility inferred by this finding, it does demonstrate viability of the Boundary Layer Augmented Maneuvering (BLAM) concept.

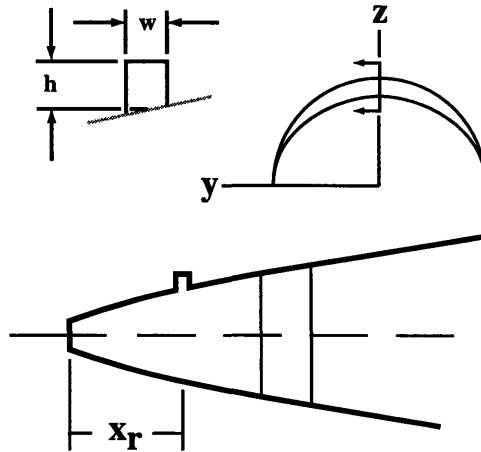


Figure 5-1: BLAM Fuze Concept

Figure 5-1 illustrates the configurational geometry of the BLAM fuze investigated, consisting of a square cross-sectioned ring with the height tapered circumferentially so that the ring has maximum height on the upper surface and tapers to zero height at right angles circumferentially each side. The purpose of the ring is to dissipate energy from the upper surface boundary layer, decreasing the momentum so that the upper surface boundary layer thickens to a larger extent than the lower surface boundary layer through the adverse pressure gradient over the boattail. The geometry investigated has an equal height and width of 1/8 inch.

As in the mechanics of linked members, such as the design of static trusses or dynamic machinery where unconstrained modes of movement are referred to as mechanisms, sensitive flow features which can be actuated by small scale displacements also function as mechanisms. The goal of design aerodynamic actuation, then, is to find the flow mechanisms which result in the desired change in integrated forces. The current concept involves two mechanisms present in the transonic flow field of boat-tailed projectiles. First, the boundary layer thickness in the adverse pressure gradient region of the boattail is sensitive to upstream influences. Second, the boat-tail shock orientation is sensitive to the boattail angle. Thus, actuation at the fuze targets the downstream boundary layer thickness over the boattail which effectively reduces the boattail angle through shock-boundary layer interaction, the resulting boattail shock orientation amplifies the previously small perturbations of the flow

field by significantly affecting the pressure distribution, as shown in Figure 5-2.

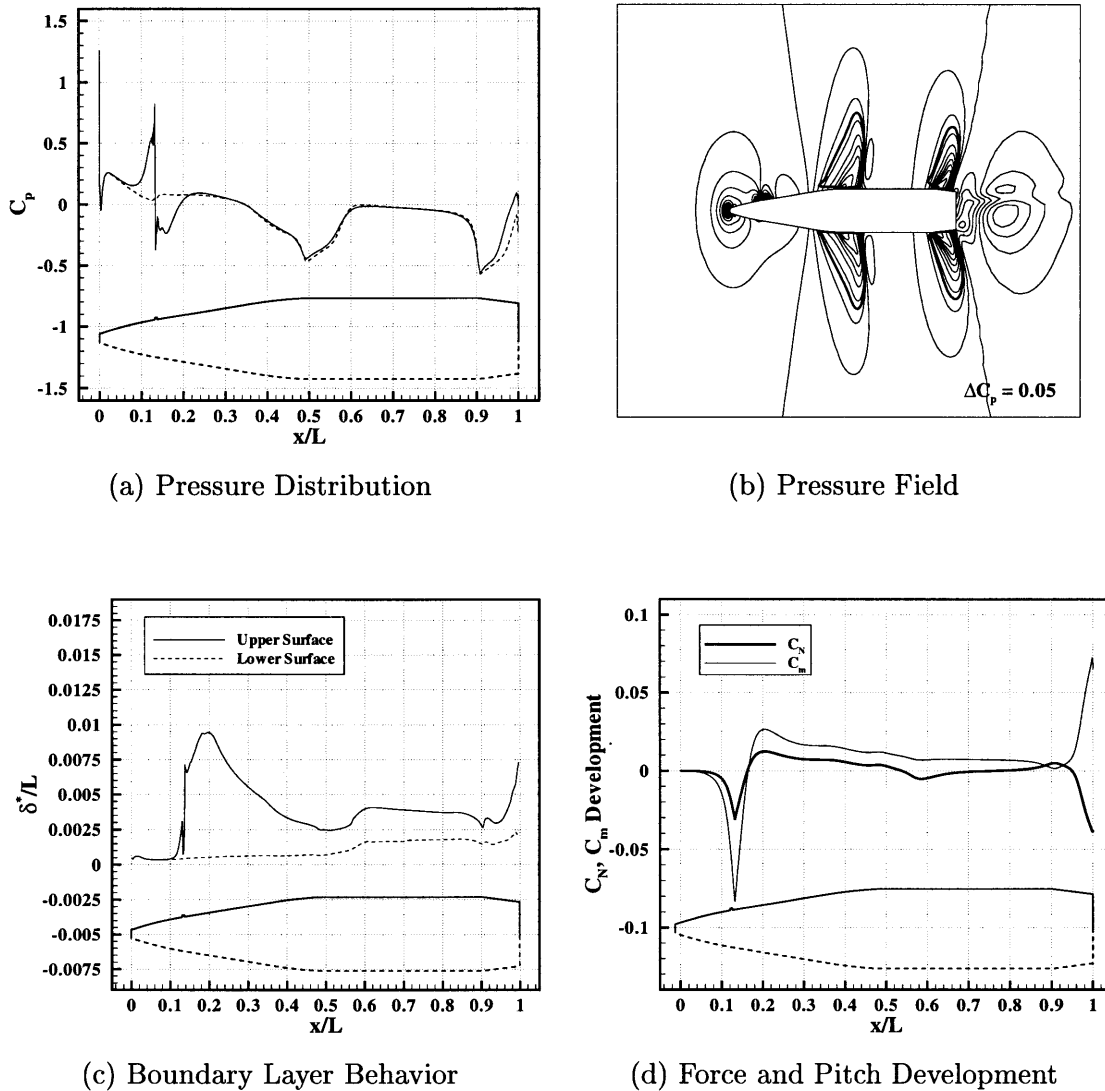


Figure 5-2: The BLAM Fuze at Mach 0.95 and Zero Angle of Attack

5.2 Angle of Attack Behavior

One of the difficulties introduced by attempting to actuate the flow with small scale surface features results from disparate energy scales of the flow. The effectiveness of micro-scale flow actuation depends on the proper targeting of sensitive flow equilibria. Unfortunately, changes in flow conditions can upset the necessarily delicate relation-

ship between the sensitivity and the method of targeting it. Changing flow conditions, such as angle of attack, can add energy into previously isolated modes of the flow field, swamping the balance between targeting mechanism and flow sensitivity.

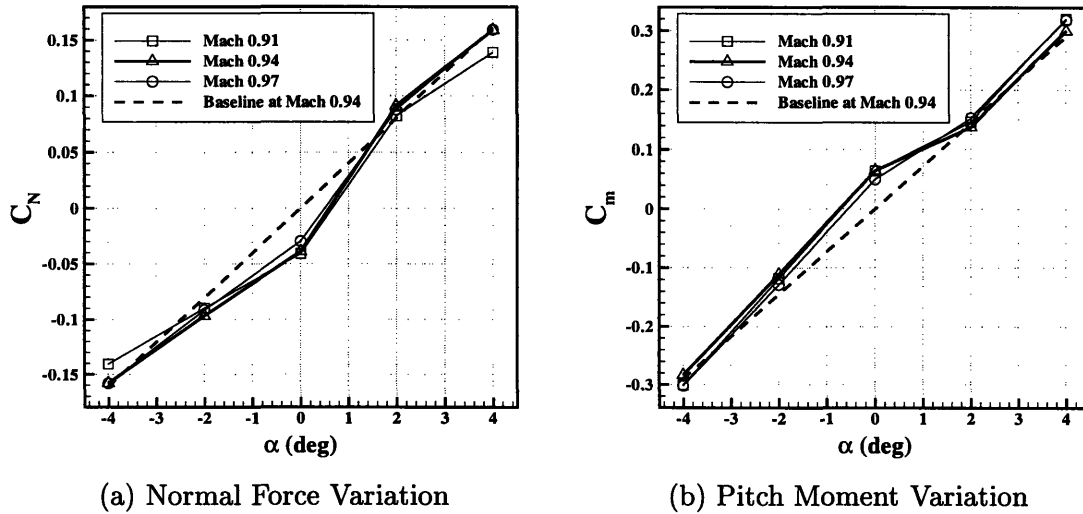


Figure 5-3: Normal Force and Pitch Moment Behavior with Angle of Attack

Figure 5-3 shows the limited effectiveness range of the current realization of the BLAM concept. The ring produces a non symmetric deviation of the force and moment behavior about zero angle of attack. For the current design, the behavior returns to that of an axisymmetric shell for angles of attack greater than 4° . Fortunately, the trim angle of attack remains in the effective range, although robustness has definitely become an issue which needs to be addressed in future refinements.

The non symmetric angle of attack behavior results from the asymmetry of the ring. Positive increasing angle of attack generally decreases the pressure on the upper surface and increases the pressure on the lower surface, which produces an overall thickening of the upper surface boundary layer and thinning of the lower surface boundary layer. The magnitude of the local down force generated by the ring decreases moderately, but as with the bent and sliced configurations, the local effect is lost as the flow returns to nearly axisymmetric. Increasing positive angle of attack decreases the pressure to which the upper boattail surface recovers and increases the pressure to which the lower surface recovers to the extent that the pressures crossover,

nullifying normal force and moment generation in the boattail region.

Increasingly negative angle of attack generally increases the pressure on the upper surface and decreases the pressure on the lower surface, which produces an overall thinning of the upper surface boundary layer and thickening of the lower surface boundary layer. The magnitude of the local down force generated by the ring increases moderately, but is lost as before. As for positive increasing angle of attack, the pressure to which the upper boattail surface recovers decreases as the angle of attack increases negatively, but the upper and lower surface pressure recoveries crossover at a greater negative angle of attack. The influence of angle of attack on the upper and lower boattail surface boundary layer thickness has a stronger influence on crossover for negatively increasing angle of attack.

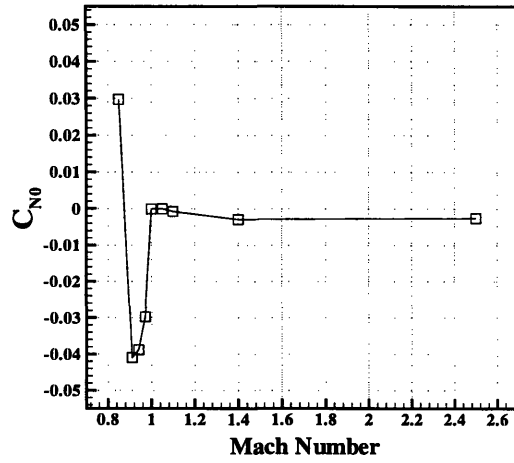
5.3 Mach Behavior

The current realization of the BLAM concept performs consistently in the transonic critical region for which it has been designed, from Mach 0.91 to Mach 0.97. Above Mach 0.97, the effectiveness decreases very rapidly as the Mach number exceeds the transonic critical region. One high subsonic Mach number has been computed, revealing a sign change in both zero offset coefficients, as can be seen in Figure 5-4. The zero-offset pitch moment changes sign near Mach 2.

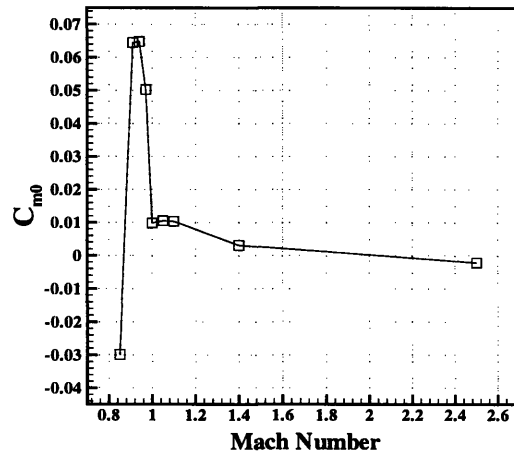
At Mach 0.85 the flow contains only very small regions of supersonic flow and the boattail shock disk is attached to the cylinder-boattail junction. The thicker upper surface boundary layer does not function to displace the upper location of the boattail shock, but reduces the pressure to which the upper surface recovers and thereby generates a local up force which becomes the primary contributor to a net positive normal force and negative pitch moment.

Above Mach 1.4 normal force and pitch moment lost through the pressure recovery from the disturbance of the ring decreases and the residual local normal force and pitch moment generation become more dominant.

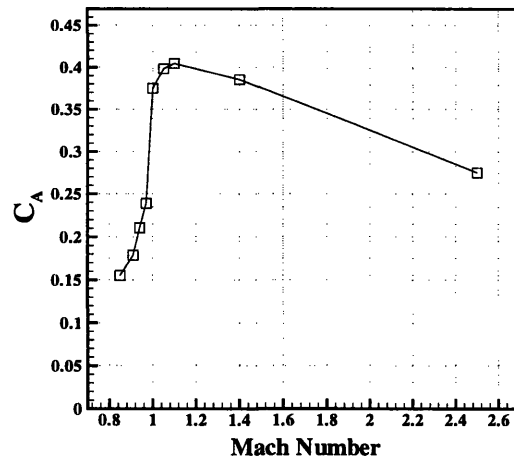
The BLAM configuration has a typical axial force curve, with only a very moderate



(a) Normal Force Variation



(b) Pitch Moment Variation



(b) Axial Force Variation

Figure 5-4: Normal Force and Pitch Moment Behavior with Mach Number

penalty incurred by the ring.

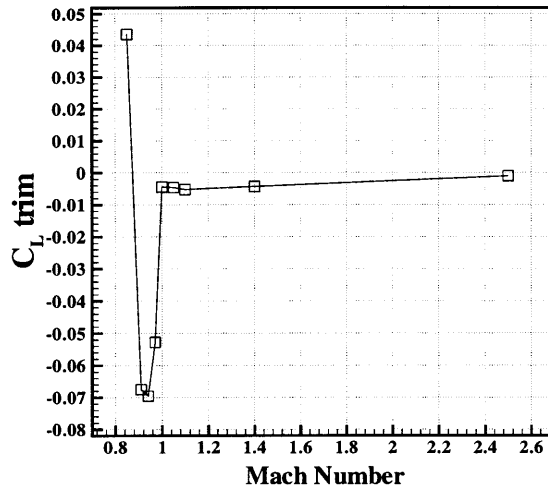


Figure 5-5: Trim Lift Variation with Mach Number

Figure 5-5 gives the variation of the trim lift with Mach number. Like the zero-offset coefficient curves, the trim lift curve has a large transonic peak which rapidly decreases to a small magnitude at Mach 1. Again, the single subsonic data point is of opposite sign, but there are no sign changes at higher Mach numbers as for the zero-offset pitch moment, although the trim lift does decrease with increasing supersonic Mach number.

The trajectories were found in Chapter 1 to have approximately identical Mach number distributions for quadrant elevations between 15 and 35 degrees. The change in sign will be a factor for trajectories resulting from lower launch velocities due to the lower speed near apogee and during descent. The rapid sign change will be problematic for the range of lower launch velocity trajectories reaching terminal velocity near the sign change. Launch velocities below this range could place the terminal velocity well within the subsonic region, which provides the potential for control if the transition through the sign change occurs rapidly enough not to destabilize the controller.

The localized high lift can be best utilized by maintaining the Mach number close to the peak Mach number for as much of the flight time as possible. This can be accomplished to first order by choosing the best launch velocity, but the inclusion of

such constraints in the control logic could prove quite fruitful.

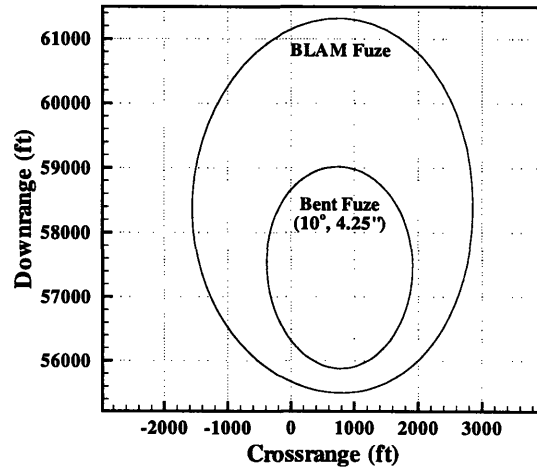


Figure 5-6: Maneuvering Envelope

The BLAM Fuze demonstrates a very impressive maneuvering envelope for the nominal trajectory and a 10 second delay in starting control, as shown in Figure 5-6. The nominal trajectory, as discussed in Chapter 1, has a Mach number always greater than 0.91 and thus avoids the sign change.

5.4 Design Considerations

The current study did not investigate many important issues necessary to make a proper design choice, leaving many questions which the novel concept must answer. No parameter variations have been performed for the height, width, cross-sectional profile or location of the ring. The baseline projectile profile does not include small surface details such as firing rings, which proved to be negligible for baseline forces and moments (justified by comparison to experiment), but the small scale of the BLAM ring makes it difficult to neglect such details. The computations performed were for static nonspinning conditions, so that the effect of spin on the boundary layer behavior needs to be probed. Spin effects are important for both the strong influence of the Magnus moment on stability and the influence of the spin on actuating the boundary layer as intended.

With these caveats aside for the moment, the concept promises many beneficial characteristics. A passive implementation would not reduce the fuze volume, leaving the maximum space available for electronics and internal torquing mechanism. The small forces acting on the ring could allow active actuation without a bulky mechanism. Although proportional actuation will most likely not be possible, the ring can be segmented providing some variation in trim lift magnitude, and the addition of simple on/off control could also be advantageous. High bandwidth on/off control of a segmented full circumferential ring could allow modulation of the ring with the spin of the fuze, thereby providing azimuthal control without despinning the fuze, or provide azimuthal control with a partially despun fuze. Given the availability of high bandwidth mechanical actuation, the accuracy of the IMU and GPS become the next constraint.

The trim lift generated by the BLAM concept varies appropriately with Mach number. Despite the advantage of the corresponding high dynamic pressures at high Mach numbers, the high Mach number range becomes unusable due to the time required to acquire the GPS signal and stabilize the IMU. The relative ineffectiveness of the design at high Mach numbers becomes a bit of an advantage because the small additional moments and forces will most likely not have much effect on stability or navigation.

In many ways, the BLAM concept actuates the flow field in a more direct way than the configurational asymmetries of the previous chapter. The configurational asymmetries generated a large magnitude normal force over the asymmetry but always lost most of what was generated, if not all of it or even more than what was generated as the flow recovered to axisymmetric. While the current realization of the BLAM fuze also exhibits quite a bit of local activity which does not contribute to the net force and moment, it successfully targets a flow mechanism which the configurational asymmetries only happenstancially actuated but from which much the net force and moment often resulted.

Actuators other than the ring investigated here can be used to disrupt the boundary layer, such as blowing and hinged flap actuators. Active control can be accom-

plished not only by actively creating the disturbance, like raising a ring, but by actively smoothing out a disturbance. An example would be a fuze with a discontinuity such as a chine that can be actively smoothed out with panels, possibly piezo-electric, that smooth the discontinuity enough to thin out the boundary layer when actuated..

Chapter 6

Canted Strakes for Torque Generation

Current competent munitions concepts require control authority over the roll orientation of the fuze. High g-loading at launch will greatly increase the friction in the bearing which attaches the fuze to the afterbody, imparting a high rate of spin to the fuze as it leaves the barrel. The rotational inertia of the fuze must then be dissipated to establish roll authority, a process called despinning. Roll authority of the fuze allows azimuthal control of the trajectory modifying normal force as well as providing a more stable and therefore more accurate platform for the IMU and GPS.

The torque required to initially despin the fuze, counteract bearing friction and establish roll authority can be obtained from an internal mechanism or by aerodynamic actuation. Aerodynamic actuation can either be active, allowing for control of the magnitude and direction of the torque, or passive. Active actuation could be produced by short canard-like vanes which can be deflected as needed, while passive actuation could be generated with a similar but non-deflecting geometry. Establishing roll control authority with passive aero-torque generation requires an internal torquing mechanism capable of overpowering the aero-torque at flight conditions where roll control is desired.

6.1 Concept and Description of Geometry

Passive aero-torque generation can be accomplished with very short surface fitting vanes, referred to as strakes. Figure 6-1 illustrates a typical dual strake geometry, as well as defining its parameters. The sides of the strake are perpendicular to the surface and the top of the strake is parallel to the surface. The strake begins and ends with a tapered section, the geometry of which has been chosen to simplify grid topology, as discussed in Chapter 2. The baseline projectile profile is the standard Mk 64.

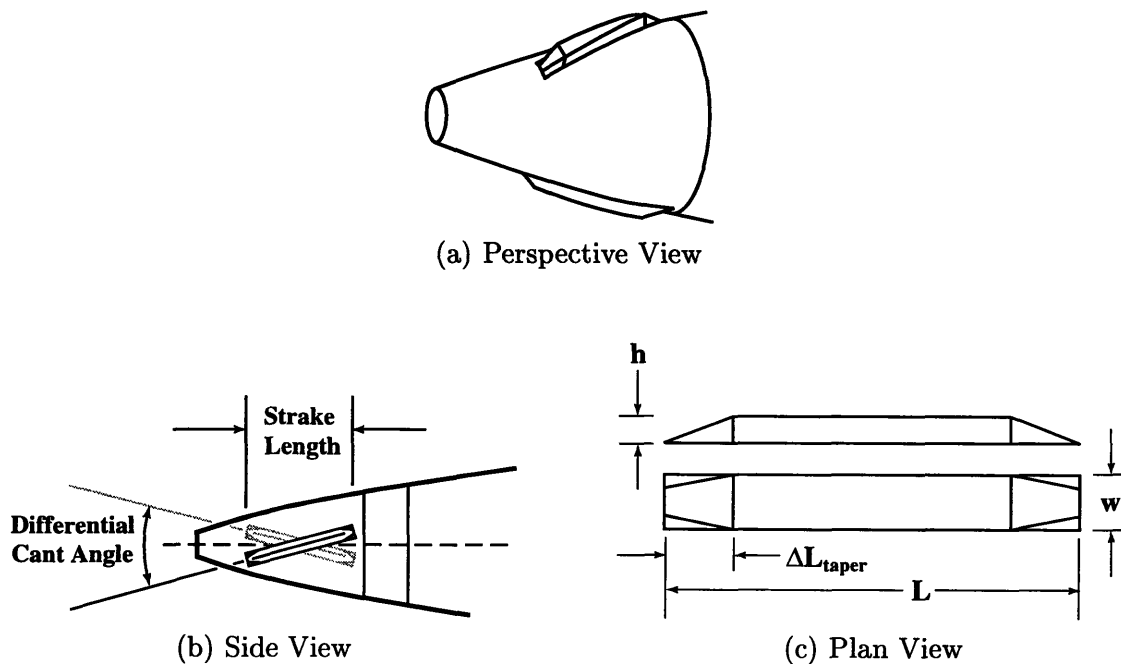


Figure 6-1: Description of Strake Geometry

The computations performed are static and do not account for torque degradation due to the spin rate modifying the local flow inclination impinging on the strake, thus, the computations predict the maximum torque situation which occurs when the fuze has been despun.

6.2 Angle of Attack and Sideslip Angle Behavior

Angle of attack and sideslip sweeps have been performed at Mach 1.1 with a dual strake geometry to investigate the effects of the strakes on the baseline behavior and to investigate the effects of flow inclination on torque generation. Normal force slope and pitch moment slope were not altered by the the presence of the strakes, but the roll torque did vary with both angle of attack and sideslip angle, as shown in Figure 6-2.

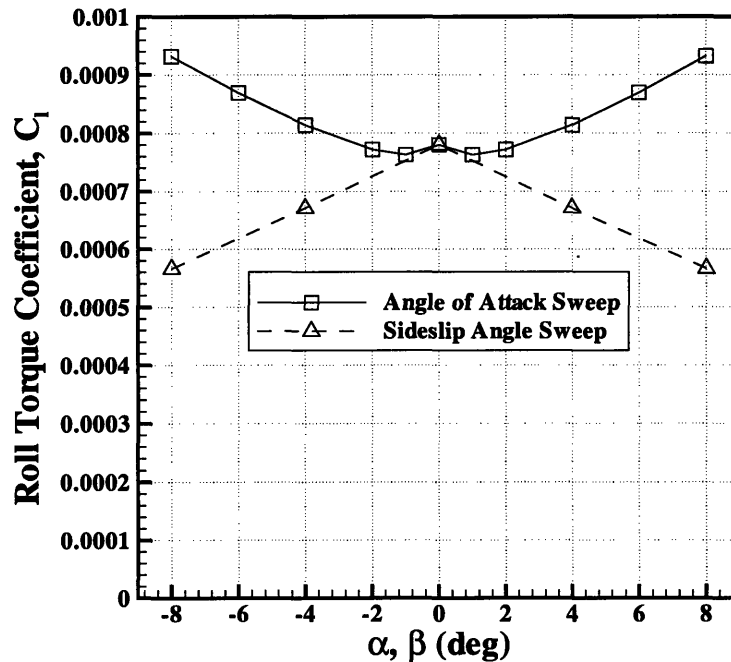


Figure 6-2: Roll Torque Variation with Angle of Attack and Sideslip Angle

The strakes are oriented as depicted in Figure 6-1b, with the pitch plane coinciding with the plane of the page. The strakes exhibit symmetric behavior with angle of attack and sideslip angle. The behavior is linear with sideslip, but has a nonlinearity in angle of attack, for which the roll torque decreases mildly at first before increasing and becoming linear.

	1	2	3	4
Length	2.0	1.5	1.5	2.0
Width	0.25	0.25	0.25	0.25
Height	0.375	0.25	0.125	0.125
Taper Length	0.25	0.25	0.25	0.25
x_{start}	0.75	1.0	1.0	0.75
Multiplicity	2	2	2	4

Table 6.1: Defining Parameters of Strake Geometries (all dimensions in inches)

6.3 Parametric Study

The roll torque of sundry configurations and Mach numbers have been computed. Table 6.1 details the configurations. For all configurations the roll torque coefficient increased linearly with cant angle and did not vary significantly with Mach number. Figure 6-3 summarizes the results.

For preliminary design purposes, the dual strake (multiplicity of 2) data can be approximately reduced with a normalization factor related to the participation of the side area of the strake in torque generation. The factor can be formulated as the product $L'h'\delta$, where L' is the length of the strake corrected for the taper, h' is the height of the strake corrected for the boundary layer thickness, and δ is the differential cant angle. Written with corrections,

$$L' = L - \Delta L_{\text{taper}}$$

$$h' = h - \delta^*$$

where the displacement boundary layer thickness, δ^* , should not be confused with the differential cant angle, δ .

The application of the above reduction is simplified by introducing a dual strake torque scaling parameter and a reference roll torque coefficient value:

$$C_l = K_{\text{DT}} C_{l,\text{ref}}$$

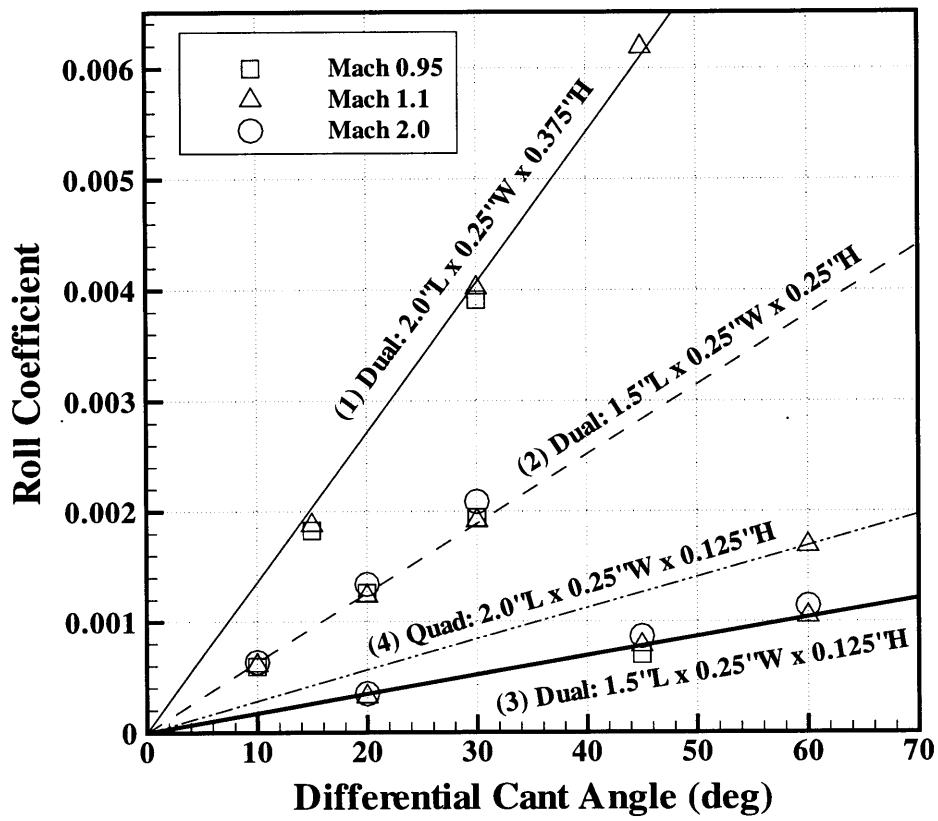


Figure 6-3: Static Roll Torque Generation

Parameter	Value
$(L'h'\delta)_{\text{ref}}$	1.375 in ² /deg
$C_{l_{\text{ref}}}$	3.48×10^{-4}

Table 6.2: Dual Strake Torque Scaling Parameters

$$K_{\text{DT}} = \frac{L'h'\delta}{(L'h'\delta)_{\text{ref}}}$$

Table 6.2 gives the constants evaluated by choosing strake geometry 3 from Table 6.1 at a 20° differential cant angle as the reference point.

6.4 Design Considerations

The dual strake torque scaling introduced provides a preliminary design algebra for sizing of strakes for standard fuze profiles. Alternate fuze profiles will modify the torque arm, implicitly contained in the constants, as well as modifying the boundary layer thickness and thus strake effectiveness.

Strake configurations with multiplicities greater than two have not been computed, except for a single quad strake. The quad strake data point suggests that the strakes do interact with each other, as suggested by the resultant torque not being on the order of twice as large as the dual strake of similar configuration. An empirical relationship relating the solidity ratio, or similar parameter, to the torque scaling could be developed from the collection of additional higher multiplicity data points.

The order of magnitude decrease in dynamic pressure over the trajectory complicates the sizing of strakes for passive aero-torque generation when the internal torquing mechanism has an active power or energy storage constraint. If the strakes are sized so as not to overpower the internal torquing mechanism or drain too much energy, then not enough aero-torque will be generated as the projectile approaches apogee and descends. If the strakes are sized to produce enough torque at low dynamic pressures, then the internal torquing mechanism will be unable to maintain control at higher dynamic pressures. The high dynamic pressure constraint has some flexibility

in that it might not be necessary to maintain control, but merely to maintain a low enough spin rate to sustain sufficient navigational accuracy.

As with the BLAM fuze of the previous chapter, the strake can be implemented as a small scale mechanical device. In general, proportional mechanics are more complex than on/off mechanics, so that control of torque magnitude might best be attained not by varying the height of strake, but by segmenting it and controlling torque magnitude by controlling the number of deployed segments. Such a strategy would allow the strakes to be sized for a very rapid despin of the fuze when fully deployed at launch, then the excess strake could be retracted when no longer necessary.

Such mechanisms will need to overcome the aerodynamic pressures exerted on the strake. Figure 6-4 gives a typical pressure distribution, extracted from a Mach 2.0 solution.

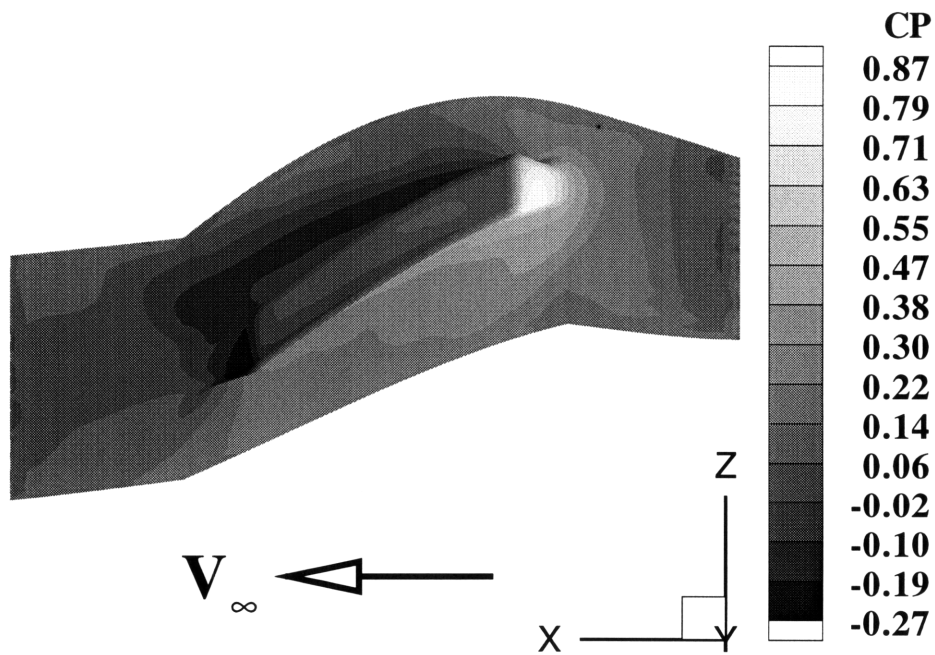


Figure 6-4: Pressure Distribution Over Strake: Geometry 3 at 20°, Mach 2.0, and Zero Angle of Attack

Finally, the effect of the strakes on transonic critical behavior of the projectile has not been investigated. The relatively large forces generated by the small ring in the previous chapter suggest that this could be an important issue, although the strakes

function in the streamwise direction and are much less likely to disturb the boundary layer significantly enough to affect the boattail sensitivity.

Chapter 7

Conclusions and Future Work

Several concepts for generating the necessary forces and moments for trajectory control have been investigated through the development and application of CFD models and through trajectory analysis. Validation of the CFD models of primarily nonspinning projectiles showed good agreement with experimental data throughout all Mach numbers of interest. Introduction of the spinning boundary condition to model Magnus effects tended to destabilize the solution, especially at transonic Mach numbers, limited the investigation of spin effects and is an area for future work.

Transonic computations for baseline profiles provided insight into the transonic critical behavior resulting from the displaced upper and lower portions of the shock disk in the boattail. Baseline computations also revealed that sting mounting of the CMATD wind tunnel model has potentially under-predicted the normal force slope by 20% and over-predicted the pitch moment slope by 10% in the transonic region. Baseline calculations showed that the small angle of attack sign change in Magnus force and moment results from the contribution of the last 2% of a spinning boat-tailed projectile. This contribution dominates the net force and moment at small angles of attack, but the forebody contribution dominates at higher angles of attack.

Computations found that the bent configuration outperformed the sliced configuration for trim lift generation and had a more favorable Mach distribution of trim lift, producing a much more substantial maneuvering envelope. The bent configuration also has advantages in the greater internal volume it provides and the smaller changes

in Magnus effect compared to the slice.

Configurational asymmetries influence the Magnus effect by increasing the Magnus force and moment for the nominal fuze orientation (maximum positive trim lift) and decreasing the Magnus force for the opposite orientation (maximum negative trim lift), introducing a Magnus dependency on fuze roll angle.

Configurational asymmetries, however, were found to perform poorly overall relative to the magnitude of force produced locally. Two factors contribute to the poor performance. First, the local high pressure flow must be accelerated from the asymmetric region to the axisymmetric afterbody. The resulting under pressure region and pressure recovery incur substantial losses. Second, local lift generation creates an induced flow which produces a counteracting force over the afterbody.

The maneuvering envelope of typical artillery trajectories have a strong sensitivity to transonic trim lift performance due to the relative amount of transonic flight time. Actuation schemes which take advantage of the aerodynamic transonic critical behavior of boattail projectiles can also take advantage of the transonic sensitivity of the trajectory and thus engender synergism. Targeting such a narrow band of the Mach number range inherits robustness to quadrant elevation from the approximate invariance of the Mach number distribution to quadrant elevation.

One concept for doing this was investigated. The concept, utilizing the tendency of an adverse pressure gradient to thicken a boundary layer, dissipated energy from the upper surface boundary layer causing it to thicken through the adverse pressure gradient of the boattail which resulted in the differential alignment of the upper and lower surface shocks in transonic flow, thereby generating a net force and moment. The concept was found to perform extremely well in the ideal environment of the computational experiments, but a number of practical issues remain to be addressed. In addition to good performance, the concept benefits from small actuator size which also provides opportunity for very compact active control effectors.

Aerodynamic torque generation was investigated with differentially canted, body fitted strakes. The strakes were found to perform linearly with cant angle and the torque coefficient was relatively constant throughout the Mach range of interest. A

number of dual strake data points were computed, allowing a simple approximate design algebra to be written. The torque generated did not scale simply with the number of strakes and the effects of multiplicity were not able to be determined from the single quad strake data point.

A number of items of future work remain to determine how best to effect trajectory control. Three flow model and computational items: improved Magnus prediction, rigid body dynamics and automated generation of Mach sweeps. Improving Magnus prediction involves a detailed look at turbulence modeling and how best to impose the boundary condition for flow model accuracy and numerical stability. Of particular interest here is the transition from the boattail into the wake, which dominates the Magnus characteristics of interest.

The free flight dynamics of projectiles exhibit complex precessional and nutational motion which could play an important role in the aerodynamic behavior of the types of actuation considered. The flow modeling of the geometry undergoing this type of motion is important both for evaluating the effectiveness of actuation concepts and for determining dynamic characteristics, such as pitch damping, which are necessary for control system design. Although steady-state approximations of Weinacht et. al. [45] could be sufficient for evaluation of steady-coning characteristics, the evaluation of unsteady flow over a projectile in free flight will provide the opportunity to explore more realistic behavior of time-dependent active actuation.

Finally, the development of an automated procedure to perform Mach sweeps would be an efficient algorithmic addition. The procedure would need to adapt to each Mach number, choosing and refining the time step, and CFL number as well as adapting the grid to improve efficiency and properly resolve the flow features at each Mach number.

Future investigation of actuation concepts should add detail. The inclusion of firing rings and other surface details will be important, especially as the fidelity of Magnus prediction increases. Surface details are also important to concepts like the BLAM fuze, which depend on the subtle boundary layer behavior.

Future work should also utilize inverse design techniques to improve the perfor-

mance of the actuators, building on the established understanding of the pressure distribution behavior. The performance of the sliced fuze, for instance, can be improved by increasing the pressure drop around the leading edge, while both configurational asymmetries will benefit from a more appropriate pressure recovery from the high pressure region.

Appendix A

Trim State Linearization

The gyroscopic dynamics can be investigated by considering a moment balance at a fixed point on the trajectory.

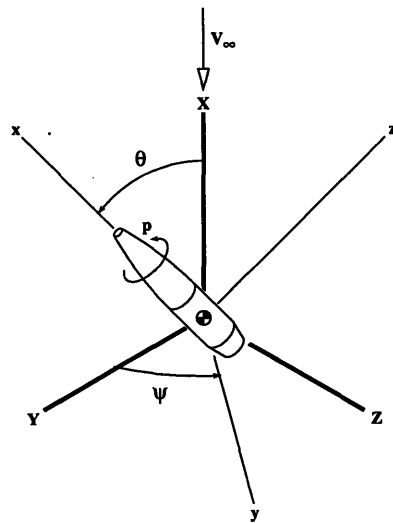


Figure A-1: Coordinate System for Rotational Motion Analysis

Figure A-1 introduces the coordinate system in which the conservation of angular momentum will be satisfied:

$$\sum \vec{M} = \dot{\vec{H}} = \left(\frac{d\vec{H}}{dt} \right)_{xyz} + \vec{\Omega} \times \vec{H} \quad (\text{A.1})$$

The relative wind is parallel but opposite in direction to the X -axis, the coning angle θ represents the total angle of attack and the aerodynamic pitch moment vector

is directed along the y axis. Plane $X-Z$ is the pitch plane and plane $X-Y$ is the yaw plane. As in the aeroballistic coordinate system, the Z axis points down, orienting positive α opposite to the Z axis. Pitch and yaw angles α and β are written

$$\begin{aligned}\alpha &= \theta \cos \psi \\ \beta &= \theta \sin \psi\end{aligned}\tag{A.2}$$

From the figure it can be seen that the angular velocity of the the projectile, $\vec{\omega}$, and of the $x-y-z$, $\vec{\Omega}$ axes are

$$\begin{aligned}\Omega_x &= \dot{\psi} \cos \theta & \omega_x &= \dot{\psi} \cos \theta + p \\ \Omega_y &= \dot{\theta} & \omega_y &= \dot{\theta} \\ \Omega_z &= \dot{\psi} \sin \theta & \omega_z &= \dot{\psi} \sin \theta\end{aligned}\tag{A.3}$$

The angular momentum components become

$$\begin{aligned}H_x &= I_{xx}\omega_x = I (\dot{\psi} \cos \theta + p) \\ H_y &= I_{yy}\omega_y = I_0\dot{\theta} \\ H_z &= I_{zz}\omega_z = I_0\dot{\psi} \sin \theta\end{aligned}\tag{A.4}$$

Substitution into the conservation equation produces

$$\begin{aligned}\Sigma M_x &= I \frac{d}{dt} (\dot{\psi} \cos \theta + p) \\ \Sigma M_y &= I_0 (\ddot{\theta} - \dot{\psi}^2 \sin \theta \cos \theta) + I \dot{\psi} (\dot{\psi} \cos \theta + p) \sin \theta \\ \Sigma M_z &= I_0 (\ddot{\psi} \sin \theta + 2\dot{\psi}\dot{\theta} \cos \theta) - I \dot{\theta} (\dot{\psi} \cos \theta + p)\end{aligned}\tag{A.5}$$

Damping moments are neglected which makes the spin rate constant and reduces the applied moment to a symmetric term, C_{m_α} , and an asymmetric term, C_{m_0} . Roll control of the asymmetry is modeled by holding the asymmetric pitch moment vector constant in inertial space. The asymmetric pitch moment vector is always perpendicular to the x axis, but is maintained in the $X-Y$ plane. The applied moments can be written

$$\begin{aligned}
M_y &= qSD(C_{m_\alpha}\theta + C_{m_0}\cos\psi) \\
M_z &= -qSDC_{m_0}\sin\psi
\end{aligned}
\tag{A.6}$$

The projectile will precess around the zero-moment axis

$$\begin{aligned}
M_z = 0 &\Rightarrow \psi = 0 \\
M_y = 0 &\Rightarrow \theta = -C_{m_0}/C_{m_\alpha}
\end{aligned}
\tag{A.7}$$

Recalling that $\alpha = \theta \cos\psi$, Equation A.7 shows that the zero-moment axis will lie in the same plane as the geometric asymmetry. Motion of spin-stabilized projectiles exhibit rotational time scales much shorter than translational time scales allowing the zero-moment axis to be interpreted as a linearized trim state.

$$\alpha_{\text{trim}} = -\frac{C_{m_0}}{C_{m_\alpha}}
\tag{A.8}$$

The linearized trim state has been confirmed by simulation. Equation A.5 and Equation A.6 can be solved for the angular accelerations $\dot{\theta}$ and $\dot{\psi}$, rewritten as a system of first order equations and integrated numerically.

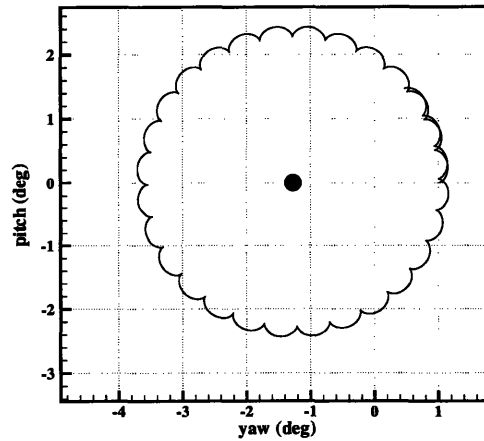


Figure A-2: Rotational Motion with $q = 1500.0$ psf, $C_{m_\alpha} = 4.5$, $C_{m_0} = 0.1$, $p = 255$ Hz and $t_f = 1.5$ seconds.

Figure A-2 shows a typical result for a pitch plane oriented asymmetry and for parameters representative of the post-apogee portion of the trajectory. The conser-

vative motion has a high frequency nutational mode due to the total angular velocity not being parallel to the major inertial axis and the motion is centered at the trim angle of attack. Note that positive α is directed opposite to positive Z , so that the precession does occur counterclockwise around the X axis, as it should.

Thus, an applied moment vector maintained in the X - Y plane, corresponding to a geometric asymmetry in the X - Z plane, produces an average trim angle of attack in the X - Z plane.

Appendix B

OVERFLOW Flow Solver Code Suite

The OVERFLOW suite of CFD tools was selected as the computational engine for the investigation. Work on OVERFLOW and the suite of tools associated with it remains active with a large user base, being led by Pieter Buning¹ of NASA Langley Research Center (previously of NASA Ames). This appendix describes the key relevant features of these tools.

B.1 OVERFLOW Flow Solver

OVERFLOW is a finite-difference Navier-Stokes solver which utilizes structured overlapped grids. The code began as a complete rewrite of the F3D/Chimera code developed by Joseph Steger at NASA Ames Research Center. Version 1.7r, dated October 30, 1996 has been used, as it was originally provided, although version 1.8 was available as of February 23, 1998.

¹OVERFLOW can be requested through license from NASA through Pieter Buning, who can be reached at p.g.buning@larc.nasa.gov

Algorithm

The time implicit algorithms evolved out of the ARC2D/ARC3D research codes and are based on the implicit approximate factorization algorithm of Beam and Warming [3]. Application to three dimensional fluid flow was first presented by Pulliam and Steger [28] and the efficiency was later improved by diagonalizing the block tridiagonal left hand side [27].

The diagonal form of the implicit algorithm retains the explicit side of the block-tridiagonal Beam and Warming approximate factorization so that both algorithms converge to identical conservative steady-state solutions. The diagonal algorithm is only first order accurate in time, however, and the diagonalization gives time accurate shock calculations a nonconservative nature producing errors in shock speed and shock jumps.

The scheme is stabilized with fourth and second order dissipation. The fourth order dissipation damps out the cascading of waves into higher and higher frequencies due to nonlinear interactions in the convection terms of the momentum equations. Undamped, this cascade results in an unstable “sawtooth” mode. Sawtooth waves are the highest frequency waves supported by the grid. Fourth order dissipation does not, however, prevent Gibbs phenomena near shock discontinuities. The wild oscillations leading and trailing shock discontinuities are damped by using second order dissipation which is switched nonlinearly such that it is only included near shocks.

Non Dimensionalization of Flow Quantities

Non dimensionalization of flow quantities follows that of the F3D and ARC3D codes. Denoting non dimensional quantities by an asterisk, we define

$$\begin{aligned}x^* &= \frac{x}{L} \\ \mathbf{V}^* &= \frac{\mathbf{V}}{a_\infty}\end{aligned}$$

$$\begin{aligned}
t^* &= \frac{ta_\infty}{L} \\
\rho^* &= \frac{\rho}{\rho_\infty} \\
p^* &= \frac{p}{\rho_\infty a_\infty^2} = \frac{p}{\gamma_\infty p_\infty} \\
T^* &= \frac{TR_\infty}{a_\infty^2} = \frac{T}{\gamma_\infty T_\infty} \\
R^* &= \frac{R}{R_\infty} \\
c_p^* &= \frac{c_p}{R_\infty} \\
c_v^* &= \frac{c_v}{R_\infty} \\
e_i^* &= \frac{e_i}{a_\infty^2} \\
\mu^* &= \frac{\mu}{\mu_\infty} \\
k^* &= \frac{k}{k_\infty} \\
\nabla^* &= L\nabla
\end{aligned}$$

A number of these non dimensionalizations were chosen such that the non dimensional thermodynamic equations have the same form as the dimensional equations.

$$\begin{aligned}
p^* &= \rho^* R^* T^* = (\gamma - 1) \rho^* e_i^* \\
a^{*2} &= \gamma R^* T^* = \frac{\gamma p^*}{\rho^*} \\
e_i^* &= c_v^* T^*
\end{aligned}$$

The coefficient of pressure can be written in terms of these quantities:

$$C_p = 2 \left(p^* - \frac{1}{\gamma} \right) \frac{1}{M_\infty^2}$$

Boundary Conditions

The boundary conditions constitute the physical definition of the flow problem. A number of boundary conditions are provided by OVERFLOW and the code is structured in a manner which allows additional boundary condition subroutines to be incorporated relatively easily through the modification of two source files and a *make*

file.

A tangential velocity boundary condition has been added to provide for the modeling of spinning projectiles. The boundary condition imposes the velocities:

$$\begin{aligned}u &= 0 \\v &= Bz^* \\w &= By^*\end{aligned}$$

where the spin parameter, B has the definition:

$$B = \frac{pL_{\text{ref}}}{a_{\infty}}$$

but can also be written in terms of the dimensionless spin rate, although the parameter varies with Mach number in this form (holding $pD/2V$ constant).

$$B = \frac{pD}{2V} \frac{M_{\infty}}{\frac{r_{\text{ref}}}{L_{\text{ref}}}}$$

B.2 HYPGEN Volume Grid Generator

HYPGEN [5] generates three-dimensional volume grids by marching away from a user-supplied single-block surface grid. The marching is accomplished by the solution of the three-dimensional hyperbolic grid generation equations composed of two orthogonality relations and one cell volume constraint as well as a specified stretching function which determines the step size normal to the surface. Version 2.0 of HYPGEN has been used.

The inputs to HYPGEN consist of a surface grid, parameters defining the normal spacing, parameters defining the boundary conditions and parameters governing some more subtle numerics such as smoothing and constraints on angles and volume growth away from the surface. The surface grid, acting as the initial conditions to a hyperbolic system, strongly drives the stability and subsequent quality of the resulting grid. Small changes in surface spacing in marginally stable regions, such as the concave

corner and axis defining the boattail wake region, can affect the convergence of the grid generator.

B.3 PEGSUS Connectivity Solver

PEGSUS [41] calculates the interconnections between the aggregate of grids defining an overlapped grid system. Overlapping nodes will lie not only within the flow field defined by other grids, but also within regions which could be defined as external to the flow field. The connectivity solver has the task of determining which nodes should be ignored, called blanking, which nodes will serve as an interface to other grids and how those nodes will interface with other grids. PEGSUS 4.1 Version 46 has been used.

The input consists of the independent but overlapping volume grids, and the specification of planes defining the interfacing boundaries and planes which cut out portions of the volume not contained in the flow field. The user can also specify a minimum interpolant quality to maintain. Nodes for which satisfactory interpolants were not able to be found are flagged as orphaned points. Once the correct interconnection topology has been specified, the task is to generate overlapping grids which share enough volume and have comparable resolution in the overlap region.

B.4 CHIMERA Grid Tools

A collection of very useful utilities has also been developed, called the CHIMERA grid tools. The utilities allow for the generation and manipulation of structured over-set grids. A preliminary version of the package, Version 0.2 has been used. Many of the utilities have been incorporated into a modular visually driven grid manipulation program called OVERGRID, which was found to be useful. Several of the manipulation utilities were used on this project, in addition to the OVERGRID interface. GRIDDED, which extracts subsets, converts grid formats and extrapolates mirror symmetry planes. SRAP spline fits nodes of a grid plane and allows more grid lines

to be added and redistributed over the surface. Finally, the grid projection utility PROGRD was used to ensure that overlapping sections of surface grid were on the same surface.

Appendix C

Physical-Space Weight Function

Compressible flow fields can exhibit very high gradients in the form of shocks and expansion fans, the modeling of which can be efficiently improved by refining the grid in regions where these flow features are expected. A priori knowledge of flow field structure can be obtained from experimental results, preliminary computations or can be postulated from the geometry, as discontinuities and high curvature regions tend to produce discontinuities in the flow field. Longitudinal refinement has been facilitated by use of a physical-space weighted one dimensional grid generation algorithm. While solutions of nonlinear differential equations are certainly not required to discretize one dimensional space, this approach allows smooth integration of boundary constraints specification of grid space weighting.

Position in physical space is represented as $x \in [a, b]$, Computational (logical) space is represented as $\xi \in [0, 1]$ and the specified weighting is given by the nonnegative function $w(x)$ which is defined on $[a, b]$. The goal is to find a grid, represented as the indexed variable x_i , such that the distance between points, $x_{i+1} - x_i$ is determined from the value of the weighting function midway between the two points, $w((x_{i+1} + x_i)/2)$. Written

$$x_{i+1} - x_i = Kw \left(\frac{x_{i+1} + x_i}{2} \right) \quad (\text{C.1})$$

where the constant K is unknown. The above equation implies the continuous equa-

tion

$$\frac{x_\xi(\xi)}{w(x(\xi))} = C \quad (\text{C.2})$$

which can be differentiated to remove the unknown constant

$$\left(\frac{x_\xi(\xi)}{w(x(\xi))} \right)_\xi = 0 \quad (\text{C.3})$$

The above equation can be discretized with centered differences, yielding the nonlinear discrete approximation

$$\frac{1}{w(x_{i+1/2})} x_{i-1} - \left(\frac{1}{w(x_{i+1/2})} + \frac{1}{w(x_{i-1/2})} \right) x_i + \frac{1}{w(x_{i-1/2})} x_{i-1} = 0 \quad (\text{C.4})$$

The above discrete system is tridiagonal and can be solved by lagging the x values used for weight calculation and iterating until converged. Solutions are not guaranteed to exist or to be unique, but experience has shown them to be acceptable. A uniform grid was used for an initial guess.

The weighting function is specified as the summation of an arbitrary but finite number of source elements, which have the form depicted in Figure C-1 and given by Equation C.5.

$$w(x) = \sum_k \lambda_k \phi_k(x) \quad (\text{C.5})$$

where d is the distance between the grid point and the source location and ϕ is unity for $d < r_k$, otherwise

$$\phi_k(x) = \exp[-c_k(d - r_k)] \quad (\text{C.6})$$

Figure C-2 shows a prototypical weighting function used for the axisymmetric baseline profiles.

In order to maintain defining points of the geometry, such as discontinuities, phys-

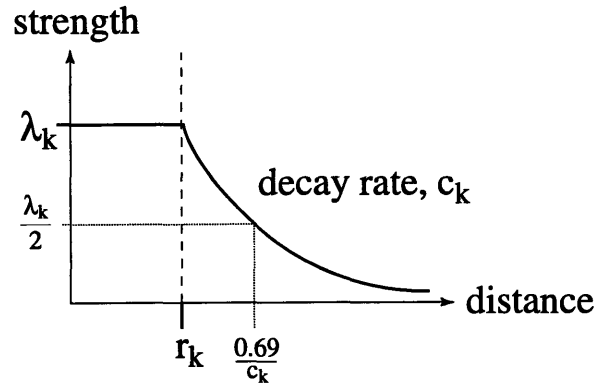


Figure C-1: Grid Spacing Source Element

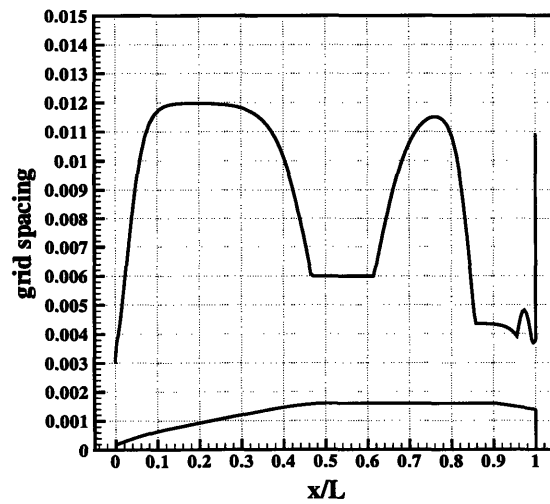


Figure C-2: Typical Grid Spacing Specified by Source Weighting Elements

ical points are marked and grid generation is carried out piecewise on each segment. Additionally, it is desirable to specify a maximum spacing not to be exceeded. The initial guess and thus the initial number of grid points is determined from evenly distributing grid points to achieve the necessary maximum spacing everywhere. Grid points are then added to each segment during each iteration until the system converges and the maximum spacing is not exceeded anywhere.

Bibliography

- [1] Holt Ashley and Marten Landahl. *Aerodynamics of Wings and Bodies*. Dover Publications, Inc., 1965.
- [2] B. Baldwin and T. Barth. A one-equation turbulence transport model for high Reynolds number wall-bounded flows. Technical Memorandum 102847, NASA, 1990.
- [3] R. Beam and R.F. Warming. An implicit finite-difference algorithm for hyperbolic systems in conservation law form. *Journal of Computational Physics*, 22:87–110, 1976.
- [4] W. R. Chadwick and J. F. Sylvester. Dynamic stability of the 5-inch/54 rocket assisted projectile (the influence of a non-linear Magnus moment). NWL Report 2059, U.S. Naval Weapons Laboratory, Dahlgren, Virginia, October 5 1966.
- [5] William M. Chan, Ing-Tsau Chiu, and Pieter G. Buning. User's manual for the HYPGEN hyperbolic grid generator and the HGUI graphical user interface. Technical Memorandum 108791, NASA, Ames Research Center, Moffet Field, CA, October 1993.
- [6] W. B. Compton, J. L. Thomas, W. K. Abeyounis, and M. L. Mason. Transonic navier-stokes solutions of three-dimensional afterbody flows. TM 4111, NASA, July 1989.
- [7] G. S. Deiwert. Numerical simulation of three-dimensional boattail afterbody flowfields. *AIAA Journal*, 19:582–588, May 1981.

- [8] W. F. Donovan and L. C. MacAllister. Transonic range tests of 5-inch/54 rocket-assisted projectile (inert). Memorandum Report 2107, Ballistic Research Laboratories, Aberdeen Proving Ground, Maryland, July 1971.
- [9] H. A. Dwyer and B. R. Sanders. Magnus forces on spinning supersonic cones—part I: The boundary layer. *AIAA Journal*, 14(4):498–504, April 1976.
- [10] J.A. Edwards and J.J. Roper. A computational assessment of static and dynamic coefficients for the H3 hypervelocity projectile. In *35th aerospace Sciences Meeting and Exhibit, January 6-10, 1997 / Reno, NV*, number AIAA 97-0640.
- [11] Jan-Kaung Fu and Shen-Min Liang. Computations of aerodynamic drag for turbulent transonic projectiles with and without spin. *AIAA 93-3416-CP*, 1993.
- [12] C. Gracey, E. M. Cliff, F. H. Lutze, and H. J. Kelley. Fixed-trim re-entry guidance analysis. *Journal of Guidance*, 5(6), November-December 1982. (Also AIAA 81-1754).
- [13] Jerome T. Kegelman, Robert C. Nelson, and Thomas J. Mueller. The boundary layer on an axisymmetric body with and without spin. *AIAA Journal*, 21(11):1485–1491, November 1983.
- [14] R. W. Kline and E. F. Brown. Ballistic similtude analysis of the 155 MM M483A1 and XM795 projectiles. Technical Report ARLCD-TR-77018.
- [15] R. W. Kline and T. D. Hoffman. Aeroballistic performance of several designs of the 155 MM M483 projectile. Technical Report ARLCD-TR-78023, US Army Armament Research and Development Command, Large Caliber Weapons Systems Laboratory, Dover, New Jersey, October 1978.
- [16] Patrick Knupp and Stanly Steinberg. *Fundamentals of Grid Generation*. CRC Press, Boca Raton, Florida, 1993.
- [17] T. Mairson, J. Smith, and K. Smith. CHAMP phase II: Exploratory development; volume II: Theory and simulation of controlled projectile. Technical

- Report AD-A145 160, US Army ARRADCOM, Dover, New Jersey, February 1977.
- [18] John C. Martin. On Magnus effects caused by the boundary layer displacement thickness on bodies of revolution at small angles of attack. BRL Report 870 - Revised, Ballistic Research Laboratories, Aberdeen Proving Ground, Maryland, 1955.
- [19] Jeremiah E. McGinley, Richard J. Schoon, and James O. Sweeny. Guided projectile feasibility study. Technical Report AFATL-TR-81-45, Air Force Armament Laboratory, April 1981.
- [20] M.C. Miller. Pressure measurements on a transonic spinning projectile. *Journal of Spacecraft and Rockets*, 22(5):112–118, March-April 1985.
- [21] J.-M. Moschetta, A. Lafon, and H. Deniau. Numerical investigation of supersonic vortical flow about a missile body. *Journal of Spacecraft and Rockets*, 32(5):765–770, September-October 1995.
- [22] M. P. Netterfield. Computation of the aerodynamics of spinning bodies using a point-implicit method. *AIAA 91-0339*, 1991.
- [23] M. P. Netterfield. Modern CFD methods applied to aerodynamic predictions of spinning projectiles. *AIAA 93-0500*, 1993.
- [24] Jack N. Nielsen. *Missile Aerodynamics*. Nielsen Engineering & Research, Inc., Mountain View, California, 1988.
- [25] C. J. Nietubicz, W. B. Sturek, and K. R. Heavey. Computations of projectile Magnus effect at transonic velocities. *AIAA Journal*, 23(7):998–1004, July 1985.
- [26] C.J. Nietubicz and W.B. Sturek. Navier-Stokes code verification for projectile configurations at supersonic and transonic velocities. *AIAA 88-1995*, May 1988.
- [27] T. H. Pulliam and D.S. Chaussee. A diagonal form of an implicit approximate factorization algorithm. *Journal of Computational Physics*, 39:347, 1981.

- [28] T. H. Pulliam and J. L. Steger. Implicit finite-difference simulations of three-dimensional compressible flows. *AIAA Journal*, 18:159, 1980.
- [29] N. Qin, D.K. Ludlow, S.T. Shaw, J.A. Edwards, and A. Dupuis. Calculation of pitch damping coefficients for projectiles. In *35th aerospace Sciences Meeting and Exhibit, January 6-10, 1997 / Reno, NV*, number AIAA 97-0405.
- [30] Frank J. Regan. Preliminary static aerodynamic measurements on a proposed canard-controlled guided projectile. Wind-Tunnel Report 73, Naval Ordnance Laboratory, April 1974.
- [31] Frank J. Regan. Preliminary static and Magnus measurements on a proposed canard-controlled guided projectile. Wind-Tunnel Report 80, Naval Ordnance Laboratory, April 1974.
- [32] Jubaraj Sahu. Numerical computations of transonic critical aerodynamic behavior. *AIAA Journal*, 28(5):807–815, May 1990.
- [33] B. R. Sanders and H. A. Dwyer. Magnus forces on spinning supersonic cones. part II: Inviscid flow. *AIAA Journal*, 14(5):576–582, May 1976.
- [34] W. B. Sturek, H. A. Dwyer, L. D. Kayser, C. J. Nietubicz, R. P. Reklis, and K. O. Opalka. Computations of Magnus effect for a yawed, spinning body of revolution. *AIAA Journal*, 16(7):687–692, July 1978.
- [35] W. B. Sturek, B. J. Guidos, and C. J. Nietubicz. Computational study of nose bluntness effects for spinning shell at supersonic speeds. *Journal of Spacecraft and Rockets*, 21(1):16–20, January-February 1984.
- [36] W. B. Sturek and D. C. Mylin. Computational study of the Magnus effect on boattailed shell. *AIAA Journal*, 20(10):1462–1464, October 1982.
- [37] W. B. Sturek, D. C. Mylin, and C. C. Bush. Computational parametric study of aerodynamics of spinning slender bodies at supersonic speeds. *AIAA Journal*, 19(8):1023–1024, August 1981.

- [38] W. B. Sturek, C. J. Nietubicz, J. Sahu, and P. Weinacht. Applications of computational fluid dynamics to the aerodynamics of Army projectiles. *AIAA Journal of Spacecraft and Rockets*, 31(2):186–199, March-April 1994.
- [39] W.B. Sturek. Applications of CFD to the aerodynamics of spinning shell. *AIAA 84-0323*, January 1984.
- [40] W.B. Sturek and K.R. Heavey. Computations of projectile Magnus at transonic velocities. *AIAA Journal*, 23(7):998–1004, July 1985.
- [41] N. E. Suhs and R. W. Tramel. PEGSUS 4.0 user’s manual. Technical Report AEDC-TR-91-8, Arnold Engineering Development Center, Arnold AFB, TN, June 1991.
- [42] K. Y. Tang, W. R. Graham, and J. Peraire. Active flow control using a reduced order model and optimum control. In *27th AIAA Fluid Dynamics Conference*, New Orleans, LA, June 17-20 1996. AIAA 96-1946.
- [43] Harold R. Vaughn. A detailed development of the tricyclic theory. Technical Report SC-M-67-2933, Sandia Laboratory, Albuquerque, February 1968. (Also NASA N69-74116).
- [44] P. Weinacht. Prediction of projectile performance, stability and free-flight motion using CFD. In *35th aerospace Sciences Meeting and Exhibit, January 6-10, 1997 / Reno, NV*, number AIAA 97-0421.
- [45] Paul Weinacht, Walter B. Sturek, and Lewis B. Schiff. Navier-Stokes predictions of pitch damping for axisymmetric shell using steady coning motion. *AIAA 91-2855-CP*, 1991.